Low-Reynolds Number Adaptive Flow Control Using Dielectric Barrier Discharge Actuator

by

Young-Chang Cho

A dissertation submitted in partial fulfillment
of the requirements for the degree of
Doctor of Philosophy
(Aerospace Engineering)
in The University of Michigan
2010

Doctoral Committee:

Professor Wei Shyy, Chair
Professor Dennis S. Bernstein
Professor Peretz P. Friedmann
Professor William W. Schultz
Assistant Professor Anouck R. Girard

“The essential is invisible to the eyes.”
− Antoine de Saint-Exupéry, 1943

To my parents

ACKNOWLEDGEMENTS

The high-speed train that I took in Daegu is scheduled to arrive at Seoul in about an hour. I am in Korea to see my friend's wedding.

Every trip I have taken so far has been a process of quest after beauty. The pursuit of a Ph.D. in aerospace engineering was conceived in curiosity about the invisible, which is though powerful enough to make us fly: *airflow*. Something that fascinates us possesses indefinite orderliness. Sometimes it is like fireworks, a shining light that we can sense but can never grasp. The beauty of airflow, such as the familiar breeze around us, resides on the boundary between understanding and obscurity.

In fact, this voyage was shaped over time with the help of companions: teachers, friends and family. Teacher Eun-Jung Kim revealed the beauty of devotion to what we love. Teacher Kwang-Seup Cho evoked the joy of pursuing passion. Professor Dong-Ho Lee allowed me to initiate academic research. Professor Wei Shyy showed how to transform curiosity into understanding. And Minyoung is sharing my view of beauty. Throughout this excursion, I have owed a great debt of gratitude to my friends at the University of Michigan, especially Yongjun, Jiwon, and Jaeheon, as well as other friends in the Department of Aerospace Engineering and the Shyylab members.

There are sincere friends who have encouraged me to be unique. Though they are all in different fields, the light emitted by each of them is a guiding star in my life in an otherwise dark universe. Taekun, Minho, Hyun-chul, Min-hyun, Deok-ryun, Young Mi, Jongseon and Jun-young, to name a few.

Regardless of the time and effort devoted to a process, closure is a singularity across which nothing in one's life is continuous. Even for trivial closures, such as the moment a spoon is put down after lunch, or the appearance of someone ending one's wait, keeping

consistency and momentum in life during the moment is impossible. Though the transition is short, threads of meaning in the notion of existence experience change. In other words, I am no more what I was. However, it is a change one can never grasp or analyze.

In fact, every moment of life is a "quantum" closure, though we hardly recognize it. The fact that one has just passed a closure can be approved only by testimony: "It was a delightful lunch," or "Hello," for example.

While confronting another closure, I feel uneasiness coming from the disquietudes of discontinuity. More precisely, from the wake of infinite awaited-closures along the passage I have undergone. One moment, my perception resides on a singularity-free trajectory, leading to exultation. The next moment, infinite uncertainties, which I have missed, evoke the fear of losing orientation, force and love.

At every moment of such distraction, there is family. I am always grateful for being a member of a supportive and considerate family. My father, mother and two elder sisters are the coordinates to which I always refer, wherever I am. I also have to include my angelic cousin Aesook.

The train is about to arrive.

Now, in a brief pause, I can say that I am lucky to have encountered people who induced me to be where I am. At the risk of blurring individual favors, I am deeply grateful for fellowships from SNUIK (Seoul National University Taekkyon Club) and KAFA (Korea Air Force Academy). I can't forget Jee-hyun's help in starting my study in the University of Michigan.

Dr. Jayaraman helped me to initiate this study with few difficulties. Collaboration with Prof. Haftka and his group in the University of Florida cultivated the initial part of this work. Prof. Bernstein helped me to safely sail through the latter part of this study, which would have been filled with numerous struggles without Dr. Hoagg, Dr. Santillo, Matt Fledderjohn and Matt Holzel. I appreciate Profs. Friedmann, Girard and Schultz whose

warm advice encouraged me to finalize this dissertation. Finally, I want to extend thanks to Mary and George Lindquist who make Ann Arbor more beautiful.

TABLE OF CONTENTS

LIST OF FIGURES

LIST OF TABLES

ABSTRACT

Aerodynamic performance of low-Reynolds number flyers, for a chord based Reynolds number of 10^5 or below, is sensitive to wind gusts, flow separation, and laminar-turbulent transition. Active flow control offers insight into fluid physics as well as possible improvements in vehicle performance. However, the complexity associated with unsteady and transitional flows, as well as the unpredictability of wind gusts, makes the development of active flow control with feedback difficult. Recently, the dielectric barrier discharge (DBD) actuator, characterized by a fast response without moving parts, has emerged as a promising flow control device. Although the DBD physics and flow generation mechanisms have been explored in numerous studies, there is a lack of understanding of the performance of the DBD actuator and surrounding flows under different operating conditions and material parameters. Moreover, the disparity of time- and spatial-scales in plasma-dynamics makes direct numerical simulation of the DBD actuator impractical for real time flow control.

In this study aimed at flow control, surrogate modeling techniques are adopted to extract the features needed to characterize DBD performance. Specifically, the parametric impact of the dielectric constant, the voltage, and the waveform of a DBD actuator on the force generation and power requirement is addressed. Global sensitivity and Pareto front analyses identify parametric dependencies and distinctive regions of interest in the design space. Due to the much faster time scale associated with the DBD actuator, a quasi-steady reduced-order model can be utilized even though the surrounding fluid flow is unsteady. The feedback control is devised by combining surrogate modeling, system estimation and a penalty-based adaptive law. The only information the control algorithm (minimizing a quadratic function of the retrospective performance) requires is the first nonzero Markov

parameter and nonminimum-phase zeros of the linearized flow-actuator model, which are easy to estimate and convenient for online identification. The estimates of these system parameters are analyzed under various flow and actuation conditions using impulse and step response tests. For finite and infinite wings with the SD7003 airfoil geometry with chord based Reynolds numbers between 300 and 1000, and a 15-degree angle-of-attack, lift under modest free-stream fluctuations can be stabilized by the control law. The interaction between control and flow responses indicates that the adjusted pressure and suction regions around the DBD actuator can neutralize the lift variations. Furthermore, by minimizing the lift fluctuation, the controlled induced-flow can either increase or decrease the drag fluctuation depending on flow conditions. The limitations of the linear modeling approach are addressed by considering the system's nonlinear behavior, and the assessed parametric drift suggests a remedy to improve control performance. In addition, guidelines on the controller and actuator setups, such as sampling frequency, impulse magnitude for system identification, and actuation voltage and location, are developed. The present modeling, estimation and control framework offers a new approach for control of low-Reynolds number aerodynamics.

CHAPTER 1
INTRODUCTION

1.1 Background

The interest in low-Reynolds number aerodynamics characterizing the flight of insect- or bird-sized flyers has increased rapidly over the last decade. These small air vehicles have distinctive potential, such as greater accessibility to confined space, lower chance of detection and superb maneuverability[1], unsurpassed by conventional high-Reynolds number vehicles. These characteristics have potential for surveillance and reconnaissance purposes. Due to the small size and low flight speed of low-Reynolds number flyers, their aerodynamics are highly influenced by unsteadiness of the flight environment, such as wind gust. As a result, an effective flow control strategy is required for low-Reynolds number flyers to achieve stable flight performance.

The development of a flow control system requires multiple interwoven methodologies. Among various flow-control schemes, the appropriate type of actuation, control-loop structure and control law can be chosen based on the control objective and fluid dynamics of interest. Since there are numerous design parameters for an air vehicle, achieving a target performance at a certain operation point has only limited applications. In order to extend the applicability and outcome of a flow control scheme to the optimization of the entire flight system, greater understanding of the flow control mechanisms and interaction between the control measure and the flow field is critical.

The principal goal of this study is to develop an effective flow control framework for low-Reynolds number unsteady aerodynamics. To facilitate control system design, the

surrogate modeling approach is used to analyze parametric impacts on actuator performance. Specifically, the impact of the applied voltage frequency, the insulator dielectric constant and the polarity time ratio of the voltage waveform on both the net force generation and required power is examined. Multiple surrogate models consistently identify two branches of the Pareto front – a set of potential optimal points with competing objectives. Each branch corresponds to either the positive net-force generation with relatively low power or the negative net-force generation with higher power. Moreover, global sensitivity analysis indicates that the voltage frequency and polarity time ratio are important only for some portions of the design space, while the dielectric constant is always important.

Instead of intending an application to a specific vehicle, the current flow-control study focuses on understanding the fundamental relations between control and underlying flow physics. As an application, the attenuation of flow unsteadiness for high-angle-of-attack infinite and finite wings at low-Reynolds numbers in the range of 300 ~ 1000 is targeted. The time-varying aerodynamic forces under moderate flow unsteadiness can be suppressed by the retrospective cost adaptive control algorithm along with the system parameters. Key issues, such as the mechanism of lift stabilization, the influence of disturbance conditions on control performance and performance limitations due to system nonlinearity are explored.

In the following sections, background concepts and conventional approaches are introduced.

1.2 Low-Reynolds number aerodynamics

The performance of low-Reynolds number flyers, specifically with Reynolds numbers lower than 10^5, is significantly affected by flow conditions[2]. Moreover, unlike higher-Reynolds-number flows, the flow structure in the low-Reynolds number regime is sensitive to flow separation, laminar-turbulent transition and flow reattachment[3]. In addition, the transition point and the size of the laminar separation bubble are dependent on free stream turbulence and unsteadiness. Thus, the flight performance under unsteady

ambient wind conditions is a major design issue[1, 4] for small air vehicles. Furthermore, at high angle-of-attack, the instability in a separated flow region induces unsteady-vortex evolution, resulting in time-varying performance.

1.3 Active flow control

Active flow control refers to the class of flow control schemes based on flow control devices that operate with energy input. Passive flow control, on the other hand, relies on devices or schemes independent of additional effort, such as surface roughness and shape variations and installation of vortex generators, to enhance the performance of a vehicle or flow element. For example, reducing the drag of a bluff body[5], increasing the stall angle of a wing and enhancing pressure recovery of a shock generator have been widely explored with passive control approaches. In contrast to the performance improvement at a fixed-operating point or the limited response to flow conditions of passive approaches, active flow control can exploit flow instabilities and enhance the region of operation[6] by manipulating control influence over the flow. As understanding of fluid dynamics at various flow regimes grows, and techniques of diagnosing and forcing flow fields are developed, active flow control techniques are used in many areas, particularly aerodynamic applications: for example, high-lift systems in flight vehicles, drag-reduction devices in ground vehicles, and noise reduction in blade-vortex interaction for rotorcrafts, to name a few.

Based on the objective of control, the applications of active flow control can be divided into flow-induced noise reduction, drag reduction and/or lift enhancement for bluff or aerodynamic bodies, and mitigation of flow unsteadiness. On the other hand, considering the impact on the flow field, flow control techniques can be classified into momentum addition to the flow such as wall motion, vortex generation and wall jet, suction of the retarded flow, body-shape deformation, wall heating and cooling, and acoustic excitation. More detailed categorization and examples of flow control techniques can be found in Gad-el-Hak[7], Chang[8], and Joslin and Miller[9]. Each application achieves its control goal by managing either coherent structures in the flow field, flow transition, flow separation, or by considering combined effects. Although there are numerous flow control devices

known to be effective for these purposes, their fundamental contributions to the flow – depending on the operational conditions and target performance – are the manipulation of velocity profiles and/or pressure distributions.

The choice of the control strategy most effective for a flow system depends on the specific flow dynamics. For example, at high-Reynolds numbers, high-lift devices with blowing can enhance the aerodynamic lift near the stall angle by adding momentum directly to the retarded flow and preventing flow separation. At low-Reynolds numbers, on the other hand, disturbing the upstream boundary layer conditionally at a high angle-of-attack can promote the transition to turbulence, resulting in flow reattachment due to the enhanced mixing of turbulent flow. The proper time- and spatial-resolutions of a control scheme should be determined based on the size and evolution of dominant flow structures, which differ significantly according to Reynolds number. Some flow unsteadiness caused by periodic flow shedding can be eliminated by open-loop actuations, provided their control authority is sufficient to suppress the flow instability; whereas, unpredictable flow evolutions due to turbulence or unknown disturbances may require a closed-loop control system. Furthermore, the number and locations of actuators and sensors can be critical to achieving control performance. For instance, global oscillations of the flow structure with a wide frequency range, which occurs for a bluff body at high-Reynolds numbers, can incapacitate a feedback control law based on a single-sensor measurement[5].

Active flow control approaches require actuators that convert energy into the control input to the flow field. There are numerous types of flow actuators with different energy consumption, control authority, bandwidth and operation conditions. According to the energy conversion mechanism, most actuators can be divided into two groups: devices based on mechanical motions to influence the fluid, and those affecting the flow field without moving parts. The former includes synthetic-jet (zero-net mass-flux) actuators and various flaps. In addition, there are traditional flow control devices that were actively studied in the 1940's and 1950's, such as porous suction using an ejector pump and the blowing jet using the main engine exhaust[10]. Recently, piezoelectric materials have been

widely used to generate mechanical motions due to their high bandwidth and efficient energy conversion capability with simple structures. Other motion-based actuators include the pulsed microjets, which generate pulse mass injections, and vortex generator jets, which mimic conventional vortex generators with an angled jet injection[9]. Actuators without moving parts are based on either electric-, electromagnetic- or thermal-actuation methods. Gas discharge processes (thermal and non-thermal plasma-based actuators) and combustion processes belong to this category. Since no mechanical part is necessary for these actuators, they usually have benefits in operation bandwidth, responsiveness and installation over the mechanical actuators.

1.4 Plasma-based flow control

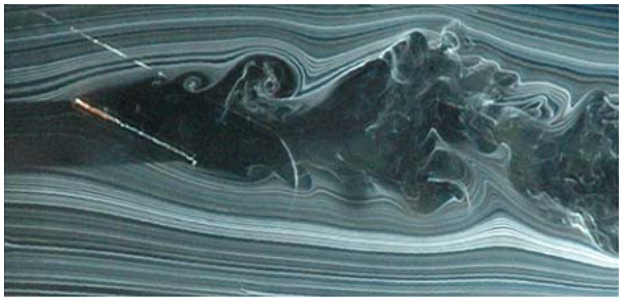

(a) baseline

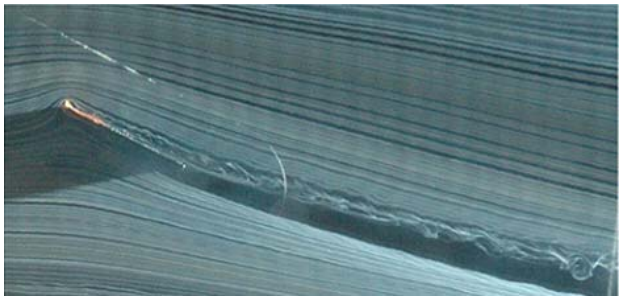

(b) DBD actuation with 8 kV, 4 kHz AC voltage

Figure 1.1 DBD actuation for a high angle-of-attack (26°) flat plate at Reynolds number of 3000 (reproduced from Greenblatt *et al*., 2008[11]).

Among active flow control devices, plasma-based flow control devices utilize ionized gases as the medium between power input and flow generation. The ionized gas (or plasma) produced either by the high-voltage gas discharge and/or high-temperature flow

conditions is activated by electromagnetic fields, resulting in induced neutral flow via momentum and/or heat transport phenomena. Plasma-based devices have advantages over the mechanical flow control devices of fast response (order of 10 kHz) and simple device structure (no moving parts). The plasma-based flow control devices can be classified based on the ionization mechanism or discharge regime. For example, the corona-based discharge and dielectric barrier discharge (DBD)[12] are popular categories of ionization for the actuators based on non-thermal plasma, which means only electrons, not heavy particles such as ions and gas molecules, are heated by discharge. In order to sustain a stable gas discharge region, the former can adopt high-voltage pulses, and the latter introduces a dielectric insulator along with AC or pulsed voltage. On the other hand, Braun *et al*.[13] categorize plasma-based flow control devices into electromagnetic flow control and electrohydrodynamic flow control and compare them in terms of operational conditions, force magnitude and applications. For the flow applications where sufficient natural ionization exists, such as hypersonic vehicles, incorporating a magnetic field can enhance the force generation more efficiently in the form of the Lorentz force than utilizing the Coulomb force only. For applications with lower flow speed, however, actuators based on electric field only, such as the DBD actuator, can be more energy efficient.

Despite their advantages, the plasma-based flow control devices have a variety of limitations that should be addressed for practical performance needs. Usually, the generation of plasma needs a high voltage source, and although the current requirement is relatively low, the power consumption per the momentum generation by the induced flow is relatively high. For example, the fluid power induced by a DBD actuator is reported to be 10^{-4} of the power input to the plasma system[14, 15]. On the other hand, though only a limited number of studies are available, for piezoelectric devices widely adopted for generating synthetic jets, an efficiency index such as the energy transmission coefficient[16] – the ratio of output mechanical energy and input electric power – is known to be 10^{-2}. This lower power efficiency, along with the limitation in operation for stable discharges, results in the limited control authority of the plasma-based devices. Although there are some attempts to apply the plasma-based devices to high-Reynolds number flows, most

studies focus on the applications with low flow speed where the momentum induced by the actuator is comparable to the inertial forces in the boundary layer. The efficiency of plasma-based actuators depends on geometric and material parameters (such as size and geometry of electrodes, and material and thickness of the insulator), operational parameters (such as magnitude and waveform of the applied voltage) and velocity, temperature and pressure of neutral flow. Since the number of design parameters is large, an extensive parametric study is required for a streamlined design of the plasma-based actuator, which may be unacceptable for experimental approaches. Considering the discharge dynamics and neutral flow physics of interest, which have very different time and spatial scales, the numerical simulation of the plasma-based actuator is expensive. For practical purposes, there are other issues such as durability and environmental impact of the plasma-based actuators. For example, the DBD actuator has been used for industrial purposes such as pollution control, surface treatment and light sources. It produces radicals and ozone[17] as byproducts, which can cause harmful impacts on the actuator durability and human health.

Recently, the number of research groups studying plasma-based actuators has increased substantially, and plasma-based flow control devices have been studied widely for various applications. For example, plasma arc actuators are applied to the jet shear layer to increase its mixing and reduce noise in the high-speed, high-Reynolds number flow[18]. The dominant aeroacoustic mode of an open cavity flow is attenuated by vortical flow structures generated by a spanwise array of plasma actuators that is located at the upstream edge of the cavity[19]. At lower Reynolds numbers between 3,000 and 20,000, the DBD actuator can enhance aerodynamic performance at high angle-of-attack and control the airfoil wake[11] as shown in Figure 1.1 for example. Some examples of the plasma-based flow control are shown in Table 1.1 and Table 1.2.

Table 1.1 Experimental studies of flow control with plasma-based actuators.

Study	Actuator type and flow regime		Objective
Greenblatt *et al*. (2008)[11]	DBD (10 kV_{p-p} AC, 4 kHz)	Re_c = 3000-50,000	High angle-of-attack airfoil performance, wake control
Huang *et al.* (2008)[20]	OAUGDP (3.2 kHz square wave)	$Re = O(10^4)$	Closed-loop attenuation of cavity noise
Asghar and Jumber (2009)[21]	DBD (5-10 kV AC, 3-10 kHz)	$Re_D = O(10^4)$	Synchronization of vortex shedding from two circular cylinders
Benard *et al*. (2008)[22]	DBD (36 kV_{p-p} AC, 1.5 kHz)	$Re_c = 2.6\times10^5$	Enhancement of post-stall performance of NACA 0015 with unsteady actuation
Benard *et al.* (2008)[23]	DBD (40 kV_{p-p} AC, 1.5 kHz, 9.6 W @ quasi-steady operation)	$Re = O(10^4\text{-}10^5)$	Jet mixing enhancement
Patel *et al.* (2006)[24]	DBD (3-12 kV_{p-p} AC, 5 kHz, 6.6-13 W/m)	$Re_c = 1.8\times10^5$	Wing stall detection (NACA 0015) using pressure fluctuation and on/off flow control
Lopera *et al*. (2007)[25]	No data	$Re_c = 4.33\times10^5$	Lift control of a scaled-UAV wing using DBD actuation along with separation ramp
Grundmann and Tropea (2009)[26]	DBD (10 kV_{p-p} AC, 6 kHz, 8.1-68.3 W/m depending on the duty-cycle)	$Re_x = O(10^3)$	Tollmien-Schlichting wave cancellation for a flat-plate boundary layer
Kim *et al.* (2009)[27]	Arc filament plasma actuators (3.2-5.4 kV AC, 12-25 W per actuator at 10-20 % duty cycle)	Ma = 0.9, $Re_D = 6.23\times10^5$	Jet noise reduction and mixing enhancement

Table 1.2 Numerical studies of flow control with plasma-based actuators.

Study	Actuator type and flow regime		Objective
Visbal *et al*. (2006)[28]	DBD ($F_{electrical}/F_{inertial}$ = 75 ~ 150)	Re_c = 45,000	Stall prevention of a high angle-of-attack NACA 0015 airfoil
Jarayaman *et al*. (2007)[29]	DBD (3 kV, 5 kHz sine wave)	$Re = 6\times10^4$	Mitigation of flow separation over a SD7003 airfoil
Poggie (2006)[30]	Glow discharge model (input power: 100 W)	Ma = 14	Local heat control of shock-induced separated flow
Rizzetta and Visbal (2008)[31]	DBD ($F_{electrical}/F_{inertial}$ = 50 ~ 100)	Re = 10,000	Mitigation of flow separation and vortex shedding from a circular cylinder
He *et al*. (2007)[32]	DBD (not specified, but corresponding experiments are based on 1.3 kHz 36 kV_{p-p} sine wave)	U_{ref} = 34.6 m/s, Ma = 0.1	Control turbulent separation over a wall-mounted hump

1.5 Design and modeling issues of DBD actuator

The Dielectric Barrier Discharge (DBD) actuator is a flow control device that is comprised of two asymmetrically placed electrodes separated by a dielectric insulator. The gas discharge, driven by kilohertz radio frequency AC or pulses with kilo-volt amplitude, generates a stable weakly ionized gas in a plasma state. The charged particles activated by the asymmetric electric field can generate the flow of neutral particles via the momentum collision process[33-35]. For the AC voltage operation, although the electric field reverses polarity between the two half cycles, the resultant neutral flow is a unidirectional wall jet-type flow due to the asymmetric electrode geometry and charged particle dynamics[36-38]. In addition, the disparity between the positive-going uniform discharge and the negative-going non-uniform one is regarded as a key role in the actuation efficiency[39]. In the operation of the dielectric barrier discharge, several operating modes such as streamer, filamentary, glow and coupled modes[40] are observed, and a homogeneous low-temperature discharge under atmospheric pressure is of great interest among researchers because of its energy efficient non-thermal ionization[41] and versatility of application[42].

Although some features of plasma-based phenomena can be captured, the experimental analysis is bounded by the difficulty of measurement, making the numerical approach crucial to understanding the mechanism and physics of the DBD actuator. Recently, numerical approaches have been improved to simulate the complex actuator discharge mechanism with qualitative comparison to the experiments. Boeuf *et al*.[35] use the fluid modeling approach to study the effect of the negative ions, which is important for air chemistry. Font *et al*.[43] compared the particle (PIC-DSMC) and fluid plasma simulations, and analyzed the asymmetry in the forward and backward cycles as well as the spatial non-neutrality in oxygen. Likhanskii *et al*.[44] demonstrate the use of positive pulses with a positive bias and report an improved performance in force generation. Roy *et al*.[45] use eight charged and neutral species for the N_2/O_2 air chemistry simulation, observing the existence of a decelerating force downstream of the powered electrode.

Although the DBD actuator has been widely studied for various flow control applications, little insight is available regarding efficient operating conditions to accommodate various performance needs. The force generated by a single actuator is less than 10 mN/m in air[46], and the induced flow velocity is usually less than 5 m/s for the pulse-input[15] and AC voltage[47] operations. Moreover, as mentioned, the performance characteristics of the DBD actuator such as force generation and power consumption are dependent on various parameters such as the type of discharge, applied voltage and material of the insulator. In order to understand the operating mechanism and, if possible, to identify optimal conditions, various researchers have done parametric studies. The effects of electrode gap and width[47], wave form of applied voltage and gas species[48], frequency and amplitude of applied voltage, dielectric material[47-49], pressure of neutral gas[50] on the induced flow velocity and/or power efficiency have been reported. However, it is difficult to assess the integrated parametric impact and the interplay between various material and operating parameters by parameter-by-parameter searching or simulations with limited parametric combinations. Before one can optimize the DBD performance, it is desirable to gain better insight into the impact of individual and collective influences of these parameters on the actuation performance.

Despite the recent efforts to accurately capture the actuator physics, significant strides are necessary to study complex flow control applications. The first-principle-based DBD model is very expensive to compute, often requiring an order of magnitude longer CPU time than that of the associated flow field simulations. Specifically, at low-Reynolds number, the disparity in time and spatial scales for plasma evolution and neutral flow physics makes the numerical simulations inefficient and infeasible for most practical problems. As a result, reduced-order or simplified DBD models have been suggested by several research groups. Since the DBD actuator operates at the frequency of kilohertz, which is several orders of magnitude faster than the flow evolution time scale, the quasi-steady force models can approximate the induced flow field satisfactorily. For example, Shyy *et al*.[37] suggest the bilinear body-force model based on the simplified linear electric field and constant charge density. Hall *et al*.[51] approximate the DBD actuator with a doublet in the potential flow field. Suzen *et al*.[52] use the pre-solved body force model

from Poisson's equations for electric field and charge distributions assuming the time-independent Gaussian charge distribution. On the other hand, Orlov *et al.*[53] use the lumped element circuit model to represent the time- and space-dependent force variations. Although the reduced-order models capture little or no plasma dynamics of the high-pressure discharge, each model incorporates the flow solver, showing a reasonable induced flow result in comparison with experiments.

1.6 Surrogate modeling techniques

Surrogate-based techniques[54] have been widely used to support engineering design problems[55, 56]. Surrogate models are functional descriptions (or mappings) representing the design variable-to-objective relations that otherwise necessitate costly numerical or experimental simulations. Surrogates trained with limited simulations enable us to generate a reliable approximation of the solution over a design space and to assess the sensitivity and correlation among the various parameters. The standard procedure starts with the design of experiments, which is the identification of design points in the design space. Once simulation results are obtained for those points, surrogate models can be generated to fit the data. There are widely used models, namely polynomial response surface approximation[57, 58], Kriging[59, 60], radial basis neural network[61] and weighted average of multiple surrogate models (also known as parameter-based surrogate model)[62, 63]. There are various factors – such as the sampling strategy of design points and the nature of the physical system itself – that affect the accuracy of surrogates. Moreover, it is well known that the performance of a surrogate model is problem-dependent. As a result, considering that the cost of fitting surrogates is usually negligible compared to that of the numerical simulations, it is beneficial to use multiple surrogate models at the same time[64]. If the accuracy of the constructed surrogates is not satisfactory and/or there exists a region of interest, the design space can be refined by repeating the whole procedure for the refined space. In addition, a design problem usually involves the optimization of multiple objectives comprised of competing factors that can be simplified by ignoring insignificant parameters using global sensitivity analysis[54, 65]. With the aid of surrogates, a trade-off curve can be created based on the so-called Pareto front analysis[66], which suggests the potential optimal points.

1.7 Closed-loop flow control

The application of closed-loop control to active flow control enables not only enhanced aerodynamic performance, but also versatile target-performance. Moreover, closed-loop flow control is required either when open-loop control under unsteady flow conditions cannot efficiently achieve a commanded target such as desired lift, or when a target is time-varying. Moreover, control effort, such as energy input to actuators, can be significantly reduced via closed-loop control while retaining or even enhancing control performances. In order to generate an appropriate control signal in response to the flow, closed-loop approaches require a controller, the measurement of flow quantities and the information of the flow-actuator system to be controlled. In feedforward control, the measured quantities can be variables free from the impact of control, such as upstream velocity or pressure. In feedback control, on the other hand, measurements include the interaction with control, such as local pressure and aerodynamic forces of interest.

Feedback flow control can be categorized in various ways. For example, Moin and Bewley (1994) divide it into adaptive schemes, schemes based on physical arguments, schemes based on dynamical systems and optimal control schemes[67]. The criteria for this categorization are how to formulate the control problem and how to obtain the system information or control-to-flow relation. The adaptive schemes are defined as approaches tuning relevant parameters based on identification of the input-to-output relation of the flow-actuator system. In the category of schemes based on physical arguments, disturbance cancellation via counter-acting actuators in response to the upstream fluctuations is included. The schemes based on dynamical systems include dimension-reduction methods that truncate the dynamics of coherent flow structures. The control goal of these approaches is to keep system states within the stable manifold to stabilize the system. The optimal control schemes are defined as the approaches based on the minimization of a cost functional by solving adjoint differential equations or their simplified versions. According to the controller formulation, flow control with Navier-Stokes equations involves control laws such as proportional-integral, linear optimal, H_∞ and Lyapunov-based[68] laws.

In order for the control signal to achieve a target performance, a controller needs information about the plant or flow-actuator system, as well as measurements. Depending on the perspective of the applications and the class of the system to be controlled, various categorizations of feedback flow control are available. Since a flow control problem is characterized by the high dimensionality and nonlinearity of the system, which augment modeling uncertainties, a comprehensive classification can be based on whether the control system requires the information of a flow field or not, or more specifically, whether the approach requires a structured model for the flow physics of interest. According to this criterion, feedback flow control approaches can be divided into two groups: approaches based on specific flow-field models and ones based on general input-output models. Each category can be further classified according to the degree of modeling and the amount of information required by models.

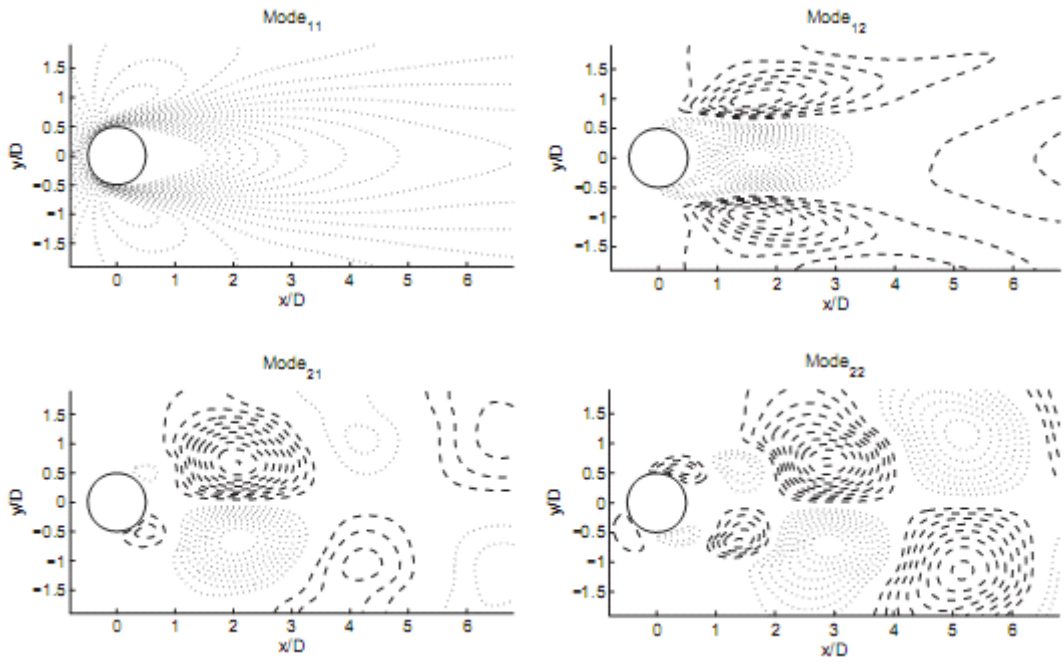

Figure 1.2 First 4 double POD modes for the circular cylinder wake (reproduced from Fagley *et al.*, 2009[69]).

The first category is composed of control schemes based on specific fluid dynamics models, such as reduced-order system equations. Since the reduced-order equations approximate the flow field, this approach usually approximates all flow quantities or

states of the entire flow field. In practice, the controller needs a process that reconstructs the entire solution field or states from limited measurements. The first step of this approach is decomposing the flow solutions into distinct modes and reducing the infinite dimensional solutions into finite dimensional subsets. The most popular techniques are the proper orthogonal decomposition (POD) and Galerkin projection methods. POD provides a set of basis functions in a low-dimensional subspace on which the governing equations are projected[70]. The Galerkin projection converts an infinite-dimensional partial differential equation into a finite set of ordinary differential equations. The optimal basis given by "empirical eigenfunctions," which guarantees to capture the greatest possible kinetic energy with a set of spatial modes as shown in Figure 1.2, can aid the projection process. However, since POD is a linear procedure, optimality is only within linear representations. Since the efficiency of the model reduction is determined by the number of the spatial modes that can represent the entire flow field, this approach is especially attractive when the flow is dominated by coherent structures, such as shedding vortices and vortex structures in turbulent boundary or shear layers, or when the flow system has an unstable steady-state. Once a reduced-order model that can reasonably approximate the time-varying solution field is obtained, a state-space representation of the flow system is available, and a canonical control law, such as the linear quadratic Gaussian (LQG) or H_∞ control, can be used. The state estimations based on limited measurements can be achieved by introducing state observers, such as the Kalman filter. Unstable vortex shedding from a high-angle-of-attack airfoil at $Re = 100$ is suppressed with LQR and a Kalman filter based on the reduced-order model with unstable modes[71]. The reduced-order models can also be used to reduce the computational cost in the adjoint-based optimization method in flow control problems[72]. Although this approach shows effective performance in, for example, suppressing unsteady force caused by low-Reynolds number vortex shedding, some difficulties should be addressed. Incorporating non-simple control input into the solution field in the process of model reduction is not straightforward and needs special treatment. For example, control input separation[18] can be used in transforming boundary control into an explicit form in the dynamic model. Furthermore, since the solution reconstruction with

measurement and linearization of fluid dynamics is always accompanied by uncertainties, it is difficult to achieve an equivalent performance goal at off-design conditions.

The approaches of the second category – the input-to-output models – do not require a particular flow model structure but a generic dynamic model with a set of parameters. In this approach, only the relation between control input and measurement is modeled, and the relevant system dynamics need to be estimated. Since the system reference model only approximates the input-to-output relation and does not reconstruct the flow field, the control system setup is less complicated. Also, the flow structures that have minor impacts on system dynamics are not considered, resulting in a reduced susceptibility to modeling uncertainty. However, some features characterizing fluid dynamics, such as high dimensionality and nonlinearity, as well as unstable steady-state, are the major challenges to non-tailored dynamics models. The choice of system models and methods of parametric estimation, which determine control performance, can be restricted by flow conditions such as flow instability. Moreover, without all the flow field information, it is difficult to select effective control and/or measurement variables and locations, which is crucial information affecting control performance as well as observability and controllability. Kutay *et al.* (2007)[73] apply a baseline PID controller compensated with an adaptive neural network to the closed-loop pitch control of a 2D wing. In recent work[74], a reduced-order model for aerodynamic force evolution based on wake vortex dynamics is introduced to extend the control bandwidth, and a LQR control law is augmented with the output feedback adaptive control based on a reference model to compensate for nonlinear system dynamics. In order to minimize flow separation on an airfoil, Pindera (2002)[75] uses an artificial neural network methodology with the nonlinear autoregressive with exogenous inputs (NARX) for both the system identifier and the controller. The online training using a gradient method with stochastic perturbation takes 20,000 and 40,000 time steps for steady and unsteady inlet conditions, respectively. Becker *et al.* (2007)[6] detect and suppress flow separation on a high-lift airfoil with the use of a single-slotted flap using extremum-seeking and slope-seeking methods as an adaptive closed-loop controller[6]. The techniques introduce harmonic excitation to search the slope of performance and achieve the maximum lift with relatively lower control effort. Although

these approaches require no reference model, which can be beneficial for avoiding modeling uncertainties, the applications are limited due to their low bandwidth and continuous harmonic actuation. Deb *et al.* (2007)[76] use adaptive inverses to compensate for actuator parameter uncertainties while using synthetic jet actuators as aircraft flight control devices. The uncertainties incorporate the actuator parameters in the nonlinear model of virtual airfoil surface deflection due to synthetic jet actuation. An ARMARKOV/Toeplitz model-based adaptive control algorithm[77] is applied to reducing the separation-induced pressure fluctuation on an airfoil[78] and to minimizing the influence of free-stream unsteadiness in a 2D channel flow[79]. Table 1.3 summarizes the closed-loop flow control applications.

Regardless of its control methodology, each approach shares several key challenges that are highlighted especially in flow control applications. First, nonlinearities should be properly quantified and addressed to avoid control failure. Although some nonlinear-modeling approaches have been adopted in flow control problems, most control laws are based on linear plant models, which are valid only within some bounds around the set point. The major nonlinearities in flow control applications lie in the nonlinear flow dynamics, which are subject to flow conditions such as Reynolds number and flow topology and the actuator's nonlinear behavior. Second, the high dimensionality intrinsic to flow dynamics hinders the model identification or reduction as well as the choice of sensors and actuators. The sensor efficiency and control authority can be highly dependent on the flow structure and should be assessed accordingly to achieve a control objective. Finally, a control scheme should be robust for uncertainties in both dynamics and measurement. In practice, all these challenges can coexist and interact.

Table 1.3 Closed-loop active flow control examples.

Study	Controller and actuator		Objective
Ahuja and Rowley (2008)[71]	Balanced truncation model, LQR, observer with force measurement	Not specified	Stabilization of vortex shedding of low-Re 2D wing
Deb *et al.* (2007)[76]	Nonlinear synthetic-jet model and its adaptive inverse, LQR	distributed synthetic jets	High-angle-of-attack separation control
Cortelezzi *et al.* (1997)[80]	Closed-form nonlinear controller, reduced-order model with vortex model	Suction point	Confine the 2D flat-plate wake in a recirculating bubble
Fagley *et al.* (2009)[69]	POD + artificial neural network – autoregressive exogenous (ANN-ARX) identification	Vertical oscillation of the cylinder	Wake control of a 2D circular cylinder
Pindera (2002)[75]	Plant-inverse controller with nonlinear autoregressive with exogenous inputs -artificial neural network (NARX - ANN)	Multiple actuators capable of suction and blowing	Elimination of the recirculating zone on the NACA 0012 airfoil
Ito and Ravindran (1996)[81]	Reduced basis method, optimal control	Partial boundary movement	Vorticity minimization in a channel flow, match a driven cavity velocity-field with the desired one
Tadmor *et al.* (2004)[82]	Empirical Galerkin method (Karhunen-Loève decomposition)	Cylinder displacement, fluid body-force	Suppression of vortex shedding behind a circular cylinder
Muse *et al.* (2009)[74]	Low-order vortex model, LQR + output feedback adaptive control	Synthetic jet pairs near the trailing edge	Vertical position control of a 2D wing
Tian *et al*. (2006)[78]	ARMARKOV disturbance rejection algorithm	Synthetic jet actuator	Suppression of pressure fluctuation on the airfoil surface
Santillo *et al*. (2007)[79]	ARMARKOV disturbance rejection algorithm	Suction/blowing jets	Suppression of flow-speed fluctuation in a 2D channel

1.8 Scope of the dissertation

The rest of the dissertation consists of 3 Chapters.

In Chapter 2, the design and modeling issues of the DBD actuators are investigated using the surrogate modeling technique. First, the sensitivity of the actuator performance to the selected material and operational parameters is studied for the 2-species helium chemistry. Specifically, the positive-to-negative polarity ratio and frequency of the applied voltage and the dielectric constant of the insulator are chosen as design variables. The objective functions are force generation and power consumption. Some key features of charge, electric field and force evolutions are explored by Pareto front analysis to achieve possible optimal conditions. Furthermore, global sensitivity analysis formulates parametric dependencies. Second, the surrogate modeling techniques are also applied to improve the fidelity of the bilinear body force model, while maintaining the computational efficiency.

In Chapter 3, the feedback control of low-Reynolds number unsteady aerodynamics is explored for a rectangular wing with the SD7003 geometry at $Re = 300 \sim 1000$. In order to understand the underlying physics, open-loop flow control with different wing aspect ratios, actuation positions and Reynolds numbers is investigated first. Then, some identification techniques – impulse response test, recursive least squares[83] and real zero identification[84] – are applied to estimate system parameters of the flow-actuator system at different flow conditions. The retrospective cost adaptive control algorithm is used to achieve disturbance rejection control. The disturbance stabilization mechanisms and non-linearity issues such as variation of system parameters are also studied.

Finally, Chapter 4 is devoted to the summary and conclusions of this study. In this chapter, the outcome and findings of this study are clarified and linked, and contributions are addressed. The surrogate-based parametric study of the DBD actuator not only extends to the investigation of optimal conditions but also bridges the gap between first-principle based simulations and the cost effective reduced-order model. The adaptive control of the flow-actuator system achieves the stabilization of unsteady aerodynamics,

illuminates the interplay between DBD actuation and flow dynamics, and suggests the design guidelines to enhance control performance. Furthermore, the issues relevant to the closed-loop control of unsteady low-Reynolds number aerodynamics of the high-angle-of-attack wing are discussed in detail. In addition, conceivable future works led by the current study are suggested.

CHAPTER 2
SURROGATE-BASED PARAMETRIC STUDY OF DBD ACTUATOR

2.1 Design and modeling issues with DBD actuator

As an active flow control device, the performance efficiency of the DBD actuator, such as force generation per power consumption, should be adequate for practical purposes. Moreover, considering the limited control authority of the DBD actuator, designing an optimized actuator is critical. The design process requires an understanding of design variables, a valid design space defined by constraints and parametric relations between design variables and objectives.

The design variables for the DBD actuator belong to three categories: geometric, operational, and material parameters. For the conventional DBD actuator setup, the geometric parameters include the dimensions and geometry of the electrodes, the distance between the electrodes, and the thickness of the insulator. The operational parameters are characteristics of the applied voltage, such as voltage amplitude, waveform – most commonly, sinusoids and pulses – and frequency. Finally, the material parameters are the dielectric constant of the insulator and electrode materials.

Some features of the relation between the DBD parameters and actuation performance can be found in other studies. For example, force generation or induced velocity is directly proportional to voltage, frequency, and rate of voltage change[47-49, 85]. Materials with a larger dielectric constant ($\varepsilon_d = 30$ compared to $\varepsilon_d = 2$) are observed to produce larger forces due to the increase in electric field strength and plasma volume at the cost of

increased power[49]. In a similar manner, a thinner dielectric material induces higher flow velocity until the electric field is high enough to produce filamentary discharge, which causes smaller momentum transfer to the neutral flow[47]. Abdoli *et al*. (2008)[86] investigate the effect of the direction and effective region of the plasma actuator on the efficiency of airfoil separation control by using constant electric field and dimensional analysis. As reviewed by Moreau (2007)[12], various factors such as type of discharge, number of actuators, geometry and voltage input have been investigated by many research groups with the idea of enhancing the performance of actuators in flow control applications.

In this study, surrogate modeling techniques[54, 87] are used to explore the parametric characteristics of the DBD actuator. The study focuses on understanding the effect of three chosen parameters – the waveform and frequency of the applied voltage and the dielectric constant of the insulator – on the DBD actuator performance characterized by power input and force generation in the flow direction using surrogate models. The main objective is to understand the impact of those variables which have significant interaction. The accuracy of each surrogate model for this application is also addressed and the surrogate models with reasonable accuracy are shown to contribute to successfully refining the design space, resolving the region of interest with higher accuracy.

For the DBD simulations, the fluid plasma model[38] is used to generate the performance data – force generation and power consumption. To simplify the problem, the 2-species helium gas chemistry is adopted. Furthermore, only the effects of the selected parameters are investigated, while other variables known to have significant impact (such as geometry) are treated as fixed. Error and performance of the various surrogate models for this application are also discussed in detail. Once a satisfactory modeling approach is established, the scope of the model can be extended to cover air chemistry as well as other geometric and operating parameters.

On the other hand, the design process should incorporate the application to the flow of interest. Not only the operational efficiency of the actuator but also the performance gains of the flow-actuator system need to be assessed appropriately. As described earlier, the numerical flow simulation with DBD actuation requires a cost-effective actuator model.

For example, the bilinear body-force model[37] simplifies the quasi-steady DBD body force with the constant charge density confined in the bilinear electric field. Even with the aggressive simplification, the bilinear model captures the key features of the induced flow field with reasonable accuracy. However, since the model only involves the applied voltage, actuator size and electrode gap as DBD parameters, its application is limited.

In order to overcome these limitations and address the issues with reduced-order modeling, the surrogate modeling techniques are applied to develop an approximate body-force model that can bridge the first principle-based model and the flow control applications. The sampled data, parametric exploration and design guidelines provided by the surrogate modeling methodology in the first part of the chapter are employed in the later part to develop the approximate body-force model.

2.2 Surrogate modeling methodology

A common modeling procedure based on surrogate models is shown in Figure 2.1.

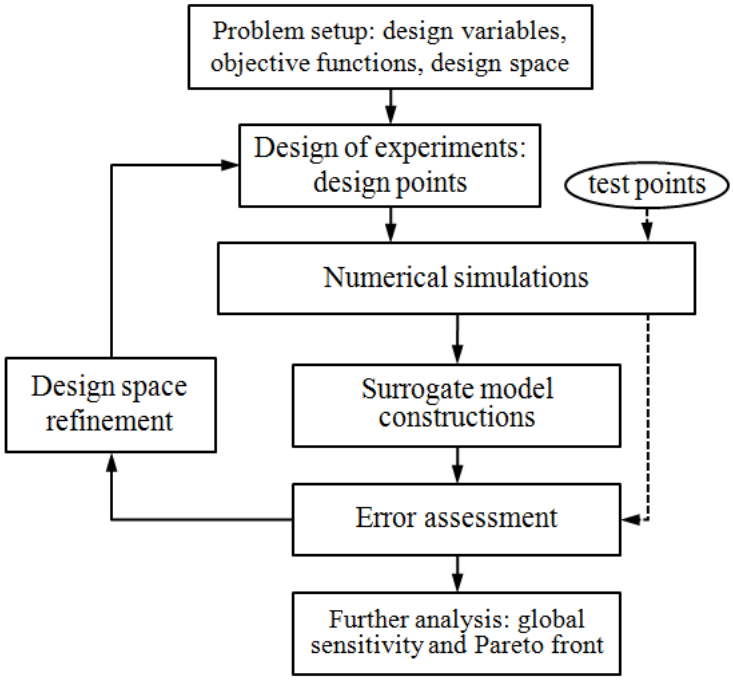

Figure 2.1 Surrogate-based modeling procedure.

An engineering design can be defined by specifying design variables, the design space – i.e., design variable constraints – and objective functions. Once a design problem is established, design points (or sampling points) are obtained through the design of experiments. Then, the objectives are obtained through numerical or experimental simulations for the design points. For most engineering problems, this process is the most time-consuming part of the procedure. The data sets of design points and objectives are then used to train multiple surrogate models. After examining the fitting quality of surrogates using pertinent error measures, sometimes including additional test points, further analysis can be performed, or the design space can be refined by repeating the whole process. In the following sections, each process is presented in detail.

2.2.1 Design of experiments

The surrogate-based modeling constructs surrogate models based on a set of design points and simulation results for these points. Due to the significant cost of most high-fidelity simulations, the number of design points is limited by computation resources. As a result, an efficient sampling strategy is required to cover the entire design space as well as to avoid missing the region of interest. The design of experiments is the sampling scheme for a given design space.

Since the characteristics of the design space – the dimension, shape of the boundary, and the gradients of the objective functions – are highly problem-dependent, no single design of experiments can be universally best. There are several popular approaches among which are the three methods used in this study: face-centered composite design (FCCD), Latin hypercube sampling (LHS), and distance-based design.

For a hypercube that represents a normalized design space, FCCD samples a design point at each vertex, and the center of each face and the cell, resulting in $(2N+2^N+1)$ points for N-dimensional space (or N-design variables). Compared to other designs, this approach populates more points on the boundaries of the design space. As a result, it provides a better resolution on the bounds, which is beneficial for problems that have a region of interest, such as the maximum, minimum and high gradient of objective functions, near the bounds. However, since the number of vertices increases exponentially as the

dimensionality of the problem grows, this approach is not efficient and becomes prohibitive for higher-dimensional design space.

LHS[88], on the other hand, divides the axes of design variables into the same number of strata, and a stratum of each axis is assigned one design point, so that each design variable has a uniform probability of sampling within the bounds. Since this approach ensures the even distribution of design points along each dimension of the design space, high dimensional design space can be filled efficiently with a given number of samplings.

Distance-based design[58] distributes sampling points to minimize the volume of the void space. Starting from a reference point, one can sequentially add the next point by maximizing the minimum Euclidean distance between the sampling points. This approach provides design points evenly filling the design space, which can be especially beneficial when the geometry of the design space is complex with irregular boundaries.

The schematics of the aforementioned design of experiments are shown in Figure 2.2.

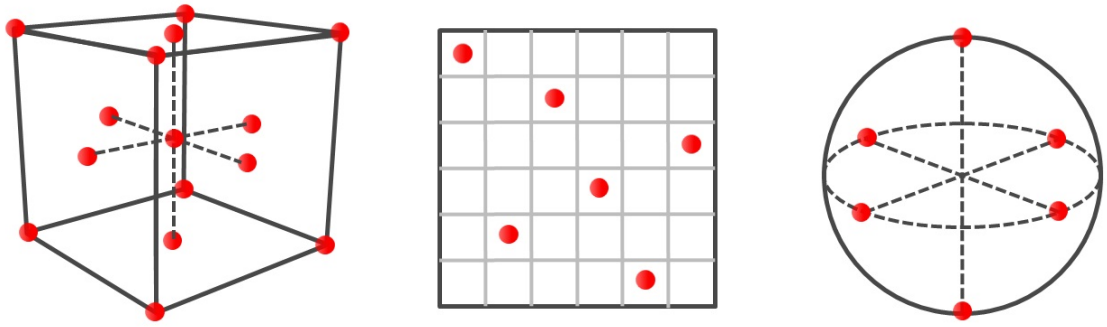

(a) FCCD (b) LHS (c) distance-based design

Figure 2.2 Design of experiments.

2.2.2 Surrogate models

a. Polynomial response surface (PRS): The polynomial response surface approximation of a function $y(\mathbf{x})$ is

$$\hat{y}(\mathbf{x}) = \sum_i b_i f_i(\mathbf{x}) \tag{2.1}$$

where b_i is the estimated value of the coefficient associated with the i^{th} basis function. The coefficient vector $\mathbf{b}$ is obtained by minimizing the error in the approximation (given by $e(\mathbf{x}) = y(\mathbf{x}) - \hat{y}(\mathbf{x})$) at k sampled design points in a least square sense as

$$\mathbf{b} = \left(X^T X\right)^{-1} X^T \mathbf{y} \tag{2.2}$$

where X is the matrix of basis functions and $\mathbf{y}$ is the vector of responses of the design points.

b. Kriging (KRG): Kriging estimates the value of an objective function $y(\mathbf{x})$ at design point $\mathbf{x}$ as the sum of a linear polynomial trend model $\sum_i \beta_i f_i(\mathbf{x})$ and a systematic departure $Z(\mathbf{x})$ representing low frequency (large scale) and high frequency (small scale) variations around the trend model.

$$\hat{y}(\mathbf{x}) = \sum_i \beta_i f_i(\mathbf{x}) + Z(\mathbf{x}) \tag{2.3}$$

The systematic departure components are assumed to be correlated as a function of distance between the locations under consideration. There are various correlation functions such as Gaussian, linear exponential, cubic and spherical. Gaussian is the most commonly used correlation function[59, 60].

$$C\left(Z(\mathbf{x}), Z(s), \boldsymbol{\theta}\right) = \prod_i \exp\left(-\theta_i (x_i - s_i)^2\right) \tag{2.4}$$

The parameters β_j and θ_j are obtained using maximum likelihood estimates. In addition, the linear correlation function is also used. The Kriging software developed by Lophaven *et al*. (2002)[60] is used to construct a Kriging model.

c. Radial basis neural network (RBNN): For radial basis neural networks, the objective function is approximated as a weighted combination of responses from radial basis functions (also known as neurons).

$$\hat{y}(\mathbf{x}) = \sum_{i=1}^{N_n} w_i a_i(\mathbf{x}) \tag{2.5}$$

where N_n is the number of neurons, $a_i(\mathbf{x})$ is the response of the i^{th} radial basis function at design point $\mathbf{x}$ and w_i is the weight associated with $a_i(\mathbf{x})$. Usually, a Gaussian function is used for radial basis function $a(\mathbf{x})$ as

$$a(\mathbf{x}) = \exp\left(-b\left\|\mathbf{s}-\mathbf{x}\right\|\right)^2 \tag{2.6}$$

where b is inversely related to a user defined parameter "spread constant" that controls the response of the radial basis function[61, 89]. A higher spread constant would cause the response of neurons to be very smooth and very high spread constant would result in a highly non-linear response function. Typically, the spread constant is selected between zero and one. The number of radial basis functions (neurons) and associated weights are determined by satisfying the user defined error "goal" on the mean square error in approximation, which is done by using the native neural networks Matlab toolbox[90].

d. PRESS weighted-average surrogate (PWS): Although one surrogate can outperform the others in terms of error measures, a better representation of the whole design space with the surrogate is not guaranteed. It is always possible that one surrogate with poorer global error measures can approximate some regions better than others. PWS is used to minimize the uncertainty associated with choosing the best surrogate by blending multiple surrogates together. The surrogate model is defined as

$$\hat{y}_{PWS}(\mathbf{x}) = \sum_{i}^{N_{sm}} w_i(\mathbf{x})\hat{y}_i(\mathbf{x}) \tag{2.7}$$

where N_{sm} is the number of surrogate models, $\hat{y}_{PWS}(\mathbf{x})$ is the predicted response of the weighted average of the surrogate models, $\hat{y}_i(\mathbf{x})$ is the predicted response by the i^{th}

surrogate model, and $w_i(\mathbf{x})$ is the weight associated with the i^{th} surrogate model at design point **x**. Furthermore, the sum of the weights must be such that, if all the surrogates coincide, $\hat{y}_{PWS}(\mathbf{x})$ should be equal to one of them. Weights are determined as follows:

$$E_{avg} = \frac{1}{N_{sm}} \sum_{i=1}^{N_{sm}} E_i; \quad \beta < 0, \ \alpha < 1 \tag{2.8}$$

$$w_i = \frac{\left(E_i + \alpha E_{avg}\right)^{\beta}}{\sum_i \left(E_i + \alpha E_{avg}\right)^{\beta}} \tag{2.9}$$

where α = 0.05 and β = -1 are used, and E_i is the global data-based error measure for i^{th} surrogate model. The error measure is substituted with the square root of the predicted residual sum of squares (PRESS), which is defined in the next section. This weighting scheme is used with polynomial response surface (PRS), Kriging (KRG) and radial basis neural networks (RBNN) approximations such that,

$$\hat{y}_{PWS} = w_{PRS}\hat{y}_{PRS} + w_{KRG}\hat{y}_{KRG} + w_{RBNN}\hat{y}_{RBNN} \tag{2.10}$$

The SURROGATES toolbox[91] is used for the implementation.

Figure 2.3 shows an example of fittings with different surrogate models.

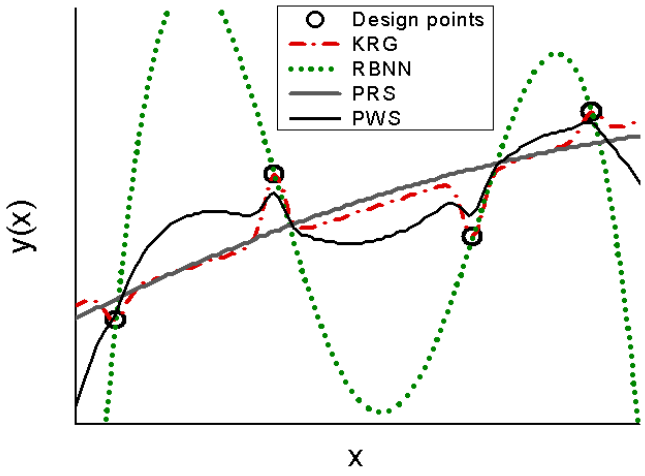

Figure 2.3 Surrogate models.

2.2.3 Error estimations and design space refinement

Since the surrogate representation is a significant model reduction from high-fidelity simulations, error estimation is a critical process for assessing the reliability of a surrogate model. Furthermore, since not the true model but only a set of sampled relations is known, the global error – the sum of the differences between the actual function and the surrogate prediction – can only be estimated. Among several popular error measures, the root mean square error for test points and the square root of predicted residual sum of squares (PRESS) are used. When simulation results for test points other than the design points are available, the prediction quality of a surrogate model can be assessed by calculating the root mean square of the differences between the test results and predictions.

When test points are not available or limited, PRESS can estimate the prediction error based on the set of design points. Instead of using all design points to train a surrogate, we can leave one point out for a test point and construct a surrogate model using a set with the other design points. By doing this for all the design points and summing the prediction error with respect to the left-out point, the global prediction error can be evaluated. In other words, PRESS can be calculated as follows.

$$PRESS = \frac{1}{N_s}\sum_{i=1}^{N_s}\left(y_i - \hat{y}_i^{(-i)}\right)^2 \tag{2.11}$$

where $\hat{y}_i^{(-i)}$ represents the prediction at $\mathbf{x}^{(i)}$ using the surrogate constructed using all sample points except $\left(\mathbf{x}^{(i)}, y_i\right)$. Compared to other error measures, such as the standard deviation of the prediction error and the adjusted coefficient of multiple determination for PRS, which are based on the fitting quality, PRESS provides a more reliable prediction measure of a surrogate model.

The poor error measures for all the surrogates indicate the performance deficiency of the given surrogate models. This deficiency could be caused either by the lack of design points or by the excessive design space size. The fidelity of a surrogate can be highly dependent on the sampling density in the design space. Although the appropriate number

of design points for a design space should be determined by the complexity of objective functions, it is rarely known a priori. Hence, considering the simulation cost, it can be more efficient to start from a design with coarser samplings and increase the prediction accuracy by refining the design space, especially the region of interest.

Design space refinement leads to a new modeling procedure. However, the bounds for the new design space can be more efficiently chosen based on the original surrogate outcomes. In order to investigate the regions of interest with the desired accuracy, the surrogate-based design can consist of multiple levels of iterative refinements.

2.2.4 Pareto front

One of the critical issues in engineering design problems is to uncover the optimal set of design variables that results in the best performance of the objectives, such as maximum force generation, minimum aerodynamic drag and minimum impact of disturbances. Furthermore, the design goal, in most cases, incorporates multiple objectives. An example of such a goal can be to design a flow control device that maximizes aerodynamic lift over drag of a wing with minimum power consumption. Since it is highly probable that one design cannot achieve the best performance for all objectives at the same time, most practical design processes involve a compromise of multiple objectives – improvement of one objective at the cost of the other. As a result, it is important to locate not just a single parameter set that enhances one performance or the other, but parameter combinations that are candidates for being the optimal set, depending on the operation need.

The Pareto front (also known as Pareto-optimal solutions) is a hyperplane (n-1 dimensional geometry in n-dimensional space) that is composed of a set of design points that are not dominated by any other design. A design is dominated by another if it is no better in any of the objectives and worse in at least one objective.

2.2.5 Global sensitivity analysis

A surrogate model $f(\mathbf{x})$ of a square integrable objective as a function of a vector of independent input variables $\mathbf{x}$ in domain [0, 1] is assumed and modeled as uniformly

distributed random variables. The surrogate model can be decomposed as the sum of functions of increasing dimensionality as

$$f(\mathbf{x}) = f_0 + \sum_i f_i(x_i) + \sum_{i<j} f_{ij}(x_i, x_j) + \cdots + f_{12\cdots N}(x_1, x_2, \cdots, x_N) \tag{2.12}$$

where $f_0 = \int_0^1 f \; d\mathbf{x}$. If the following condition

$$\int_0^1 f_{i_1 \cdots i_k} dx_k = 0 \tag{2.13}$$

is imposed for $k = i_1, \ldots, i_s$, then the previous decomposition is unique. In the context of global sensitivity analysis, the total variance denoted as $V(f)$ can be shown to be equal to

$$V(f) = \sum_{i=1}^{N_v} V_i + \sum_{1 \le i, j \le N_v} V_{ij} + \cdots + V_{1\cdots N_v} \tag{2.14}$$

where $V(f) = E\left(\left(f - f_0\right)^2\right)$ and each of the terms represents the partial contribution or partial variance of the independent variables (V_i) or set of variables to the total variance and provides an indication of their relative importance. The partial variances can be calculated using the following expressions:

$$\begin{aligned} V_i &= V\left(E\left[f \mid x_i\right]\right) \\ V_{ij} &= V\left(E\left[f \mid x_i, x_j\right]\right) - V_i - V_j \\ V_{ijk} &= V\left(E\left[f \mid x_i, x_j, x_k\right]\right) - V_{ij} - V_{ik} - V_{jk} - V_i - V_j - V_k \end{aligned} \tag{2.15}$$

and so on, where V and E denote variance and expected value respectively. Note that $E\left[f \middle| x_i\right] = \int_0^1 f_i dx_i$ and $V\left(E\left[f \middle| x_i\right]\right) = \int_0^1 f_i^2 dx_i$. Now, the sensitivity indices can be computed corresponding to the independent variables and set of variables. For example, the first and second order sensitivity indices can be computed as

$$S_i = \frac{V_i}{V(f)}, \quad S_{ij} = \frac{V_{ij}}{V(f)} \tag{2.16}$$

Under the independent model inputs assumption, the sum of all the sensitivity indices is equal to one. The first order sensitivity index for a given variable represents the main effect of the variable, but it does not take into account the effect of the interaction of the variables. The total contribution of a variable to the total variance is given as the sum of all the interactions and the main effect of the variable. The total sensitivity index of a variable is then defined as

$$S_i^{total} = \frac{V_i^{total}}{V(f)} \tag{2.17}$$

where

$$V_i^{total} = V_i + V_{i,Z} \tag{2.18}$$

where V_i is the partial variance of the objective with respect to x_i and $V_{i,z}$ is the measure of the objective variance that is dependent on interactions between x_i and Z. Similarly, the partial variance for Z can be defined as V_z. Therefore the total objective variability can be written as

$$V = V_i + V_Z + V_{i,Z} \tag{2.19}$$

The above expressions can be easily computed using Gaussian-quadrature points for numerical integration of different partial variance terms. The SURROGATES toolbox[91] is used for the implementation.

2.3 2-species fluid plasma model for DBD actuator

2.3.1 Governing equations

The set of governing equations used in modeling the DBD actuator are the continuity and momentum equations derived from the Boltzmann equation and the electric field

equation derived from the Maxwell's equations. Since the atmospheric pressure is high enough to assume local thermodynamic equilibrium, the fluid model is reasonably accurate and the local electric field density can be used to approximate the phenomena related to the collision processes – ionization/recombination, diffusion and drift - instead of solving the energy equation[92]. Governing equations are given as Eqs. (2.20)-(2.23) for two species - He^+ (subscript $p = i$) and electron (subscript $p = e$).

$$\frac{\partial n_p}{\partial t} + \nabla \cdot \left(n_p \mathbf{u}_p \right) = n_e S_{ie} - r n_i n_e \tag{2.20}$$

$$n_p \mu_p \mathbf{E} - \nabla \left(n_p D_p \right) = n_p \mathbf{u}_p \tag{2.21}$$

$$\nabla \cdot \left(\varepsilon_d \mathbf{E} \right) = \frac{q_i n_i - q_e n_e}{\varepsilon_0} \tag{2.22}$$

where n_p is the particle number density, $\mathbf{u}_p$ is the species drift velocity, S_{ie} and r are the ionization and recombination rate coefficients, and μ_p and D_p are the mobility and diffusivity of charged particles, respectively. $\mathbf{E}$ is the electric field, q is the electric charge of one species particle, and ε_0 and ε_d are the permittivity of the vacuum and the insulator, respectively.

Eq. (2.21) is the well-known drift-diffusion equation, which is valid also for ions in high pressure (atmospheric regime) discharge. To solve this set of equations, the source terms are handled with the 4th order Backward Differentiation Formula (BDF) and the Poisson equation with the algebraic multigrid method, and the second-order central difference and upwind methods are employed for the diffusion and convection terms respectively[38, 93, 94]. The charged particle densities and electric field are coupled by solving the Poisson equation between the predictor and corrector steps where the first order source splitting is used[38]. The coefficients of gaseous properties of helium regarding particle collisions and ionization/production are obtained from McDaniel (1964)[33], Mitchner and Kruger (1973)[34] and Ward (1962)[95].

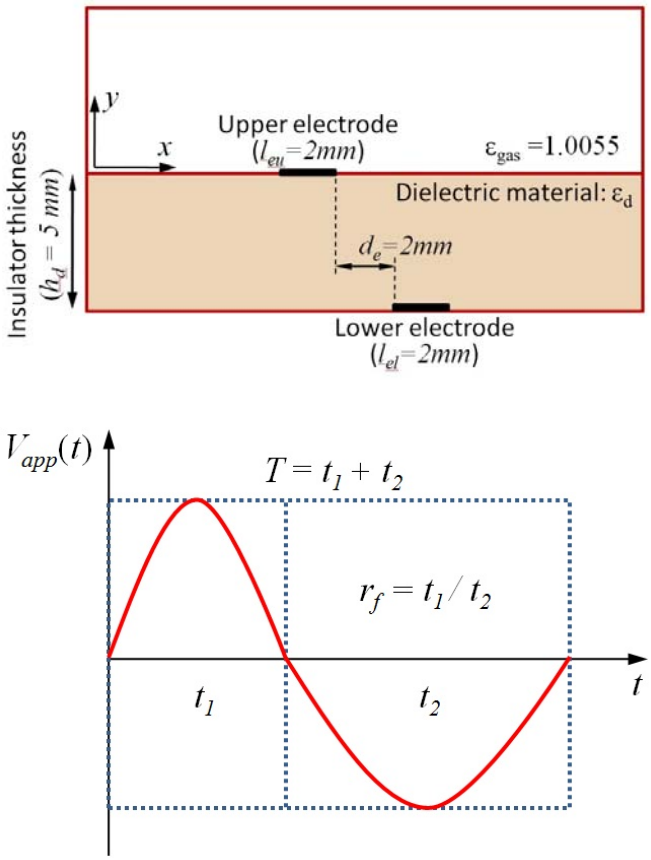

Figure 2.4 Geometry and applied voltage for the DBD actuator simulation.

The computational domain with the actuator geometry is presented in Figure 2.4. The insulator thickness h_d is set as 5 mm, and the upper electrode length l_{eu} and lower electrode length l_{el} are 2 mm, which is the same as the gap distance d_e. The applied voltage to the upper electrode is a modified sinusoidal wave with the fixed amplitude of 1 kV and variable positive-to-negative half cycle ratio r_f. Boundary conditions for the charge species on the dielectric surface are set to satisfy the current continuity that allows for the accumulation of particles, and only electrons can be absorbed into the upper electrode without secondary emission. Gas pressure of helium is set as 300 mmHg, and the ion temperature is 300 K. The electron temperature is calculated as a function of the local electric field strength using a local field approximation approach[38].

2.3.2 Model assessment

The performance of a DBD actuator is subject to various factors such as the insulator material, actuator geometry and waveform of the applied voltage. Furthermore, the fact that most of the experiments are based on air hinders the validation of the current numerical model, which adopts the simplified helium chemistry. Although the purpose of this study is not a quantitative comparison but a preliminary parametric survey, it is necessary to assess the fidelity of the result. The 1-dimensional simulation of DBD using the current model is consistent with other numerical and experimental work that uses helium as the operating gas[38]. In addition, some characteristic features of DBD such as surface charge evolution, dependency of force on the applied voltage, and electric current time evolution, can be compared for the purpose of a qualitative validation of the current model.

In Table 2.1, three different models from other studies are presented for comparison with the current model. Although every model adopts a conventional DBD actuator setup, such as asymmetrically positioned electrodes and the sinusoidal waveform of applied voltage, there exist diversities in geometric dimensions, operating gas and other parameters. Compared to other models, the current model features a thicker insulator relative to the electrodes, as well as lower voltage, which results in a comparatively weaker electric field as well as lower particle densities. Also the effects of negative ions are absent in the current model due to the choice of a simplified helium chemistry.

Table 2.1 Parameter comparisons between different models.

Models	Geometry	Operating parameters			Chemistry
		ε_d	f_v [kHz]	V_{app} [kV]	
The current model (numerical)	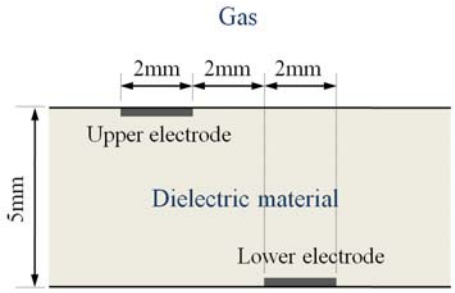	< case for Figure 2.5> 4.5	5	0.25~2.7	2 species helium
		< case for Figure 2.6> 4.5	20	1	
		< case for Figure 2.7> 14.7	7.35	1	
Van Dyken *et al.* (2004) (experimental)	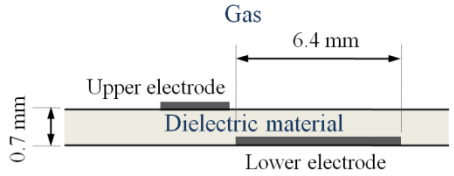	< case for Figure 2.5> 2.9~3.9 (Kapton)	5	1~6	Air
Enloe *et al.* (2008) (experimental)	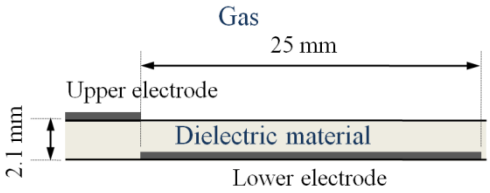	< case for Figure 2.6> 6	5	7	Air
Unfer *et al.* (2008) (numerical)	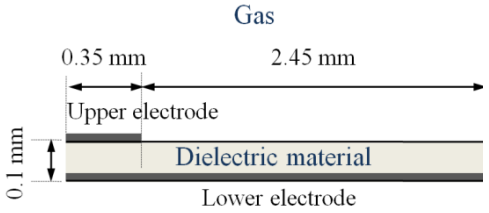	< case for Figure 2.7> 4	8	8	3 species air : positive ion, negative ion and e^-

As shown in Figure 2.5, the current model predicts power-law dependency of force generation on the amplitude of the applied voltage. The resultant force normal to the surface F_y of the current model[96] is compared to the experimental work of Van Dyken *et al*. (2004)[97]. Despite the difference in species dynamics between helium and air, as well as the range of applied voltage, the power of 2.7 is comparable with the experimental result with the power of 3.1.

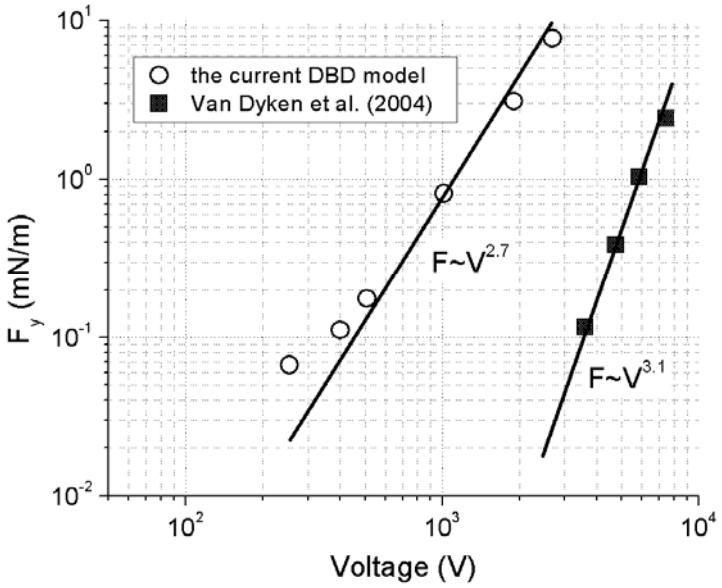

Figure 2.5 Force dependency on the applied-voltage amplitude.

Since the electric potential and the actuator dynamics are characterized by the charge accumulation on the dielectric surface as well as the applied voltage, the surface charge evolution represents a key aspect of the overall mechanism. In Figure 2.6, the surface potential distribution is compared with the experimental result[98] for four different time instants that are evenly spaced over one period of a cycle. The upper or exposed electrode exists at the left of zero and the *x*-coordinate indicates the distance from its edge, which is limited to 6mm for the current model. There are noticeable differences in geometry, frequency, amplitude of applied voltage, and operating gas between cases as summarized in Table 2.1. Nevertheless, qualitative observations for various investigations can be made. For example, when the applied voltage is near zero, the accumulated charges,

especially electron at $t/T = 0$ and ion $t/T = 0.5$, show similar residual potential distributions. This demonstrates that the charge transfer mechanism predicted by the current model is reasonable. Furthermore, despite the restricted computational domain, the potential evolution – especially near the upper electrode edge – coincides qualitatively with experiments throughout the cycle.

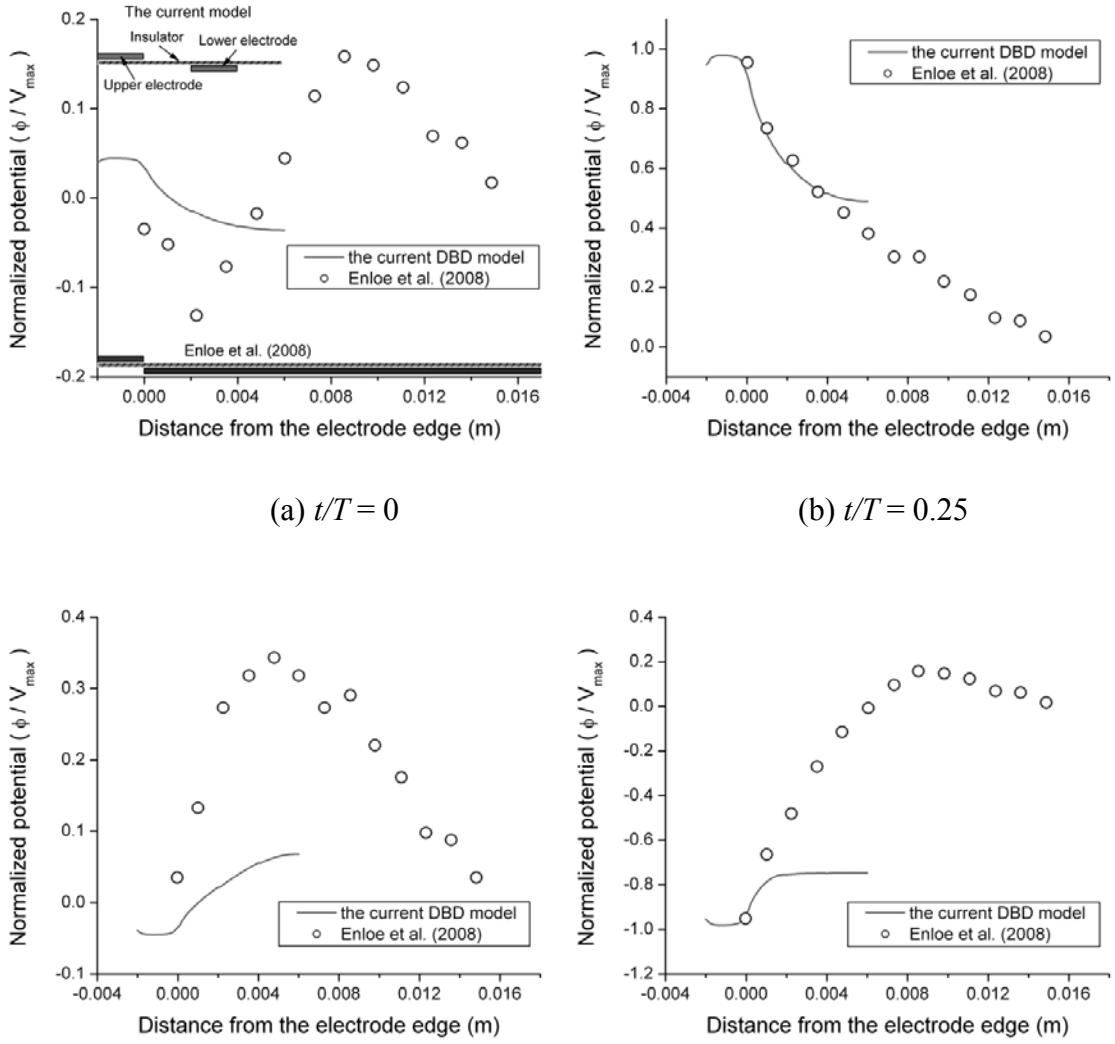

(a) $t/T = 0$ (b) $t/T = 0.25$

(c) $t/T = 0.5$ (d) $t/T = 0.75$

Figure 2.6 Electric potential distribution along the dielectric surface.

In Figure 2.7, the time history of electric current is compared to Unfer *et al*. (2008)[35]. The smaller current and absence of the peaks can be mostly explained by the electric current calculation which only reflects charge flux through the upper electrode as defined in Table 2.1 and the lower magnitude of the applied voltage in the current study. However, there are similarities between the current time histories, especially the instants where the maximum current occurs and the discharge of the positive half cycle ends. Although the current model with reduced helium chemistry does not capture all the features shown in

air applications, the characteristics of the overall discharge process and the evolution of the charged species are in qualitative agreement with other studies.

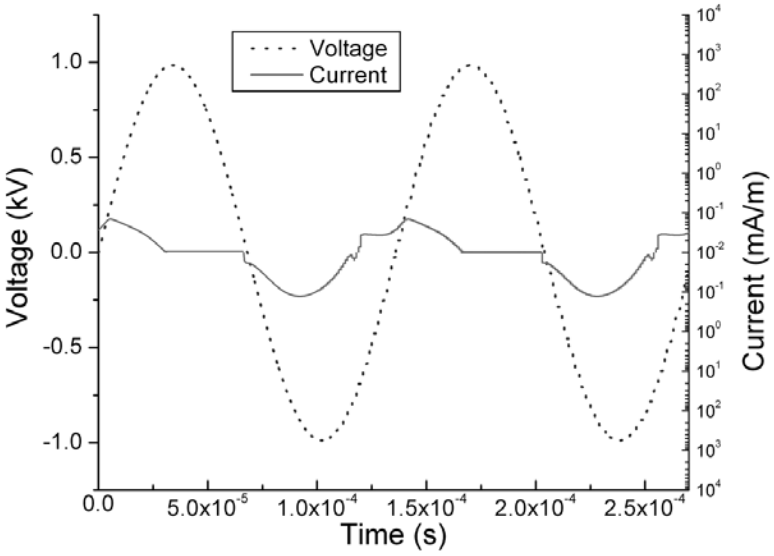

(a) current DBD model

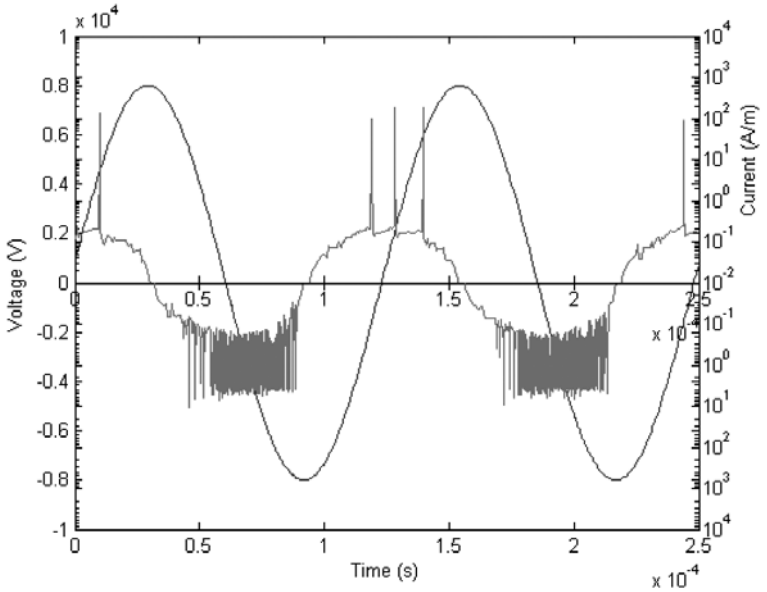

(b) reproduced from Unfer et al. (2008)

Figure 2.7 Time history of the electric current.

It should be noted here, that only a qualitative comparison is presented and hence no attempt was made to match the experimental parameters consistently in this study. The current work, however, is meaningful as a framework for developing an efficient flow control strategy and it can be directly applied to the extended air chemistry and different geometric/operating conditions. Also, the qualitative consistency of the results sheds light on further design refinement as well as characterizing parametric correlations in different chemistries.

2.4 Background study about DBD actuator

2.4.1 Evolution of plasma structure in DBD actuation

In order to understand the plasma dynamics and resultant force generation, a case with the 1 kV amplitude 5 kHz frequency sinusoidal voltage is analyzed. The time- and space-evolution of the discharge structure delivers insights into the force generation mechanism and parameters that may influence the actuation performance.

The discharge mechanism of the DBD actuator is characterized by the time-varying applied electric potential insulated by the dielectric material as well as the reaction mechanism and transport dynamics of the charged particles. The local strength of the electric field determines the rate of the ionized particle generation. Depending on the polarity of the exposed electrode, the electrons and negative or positive ions are attracted to or repelled from the electrode. Moreover, it is known that the charged particles deposited on the insulator at some time instant limit the discharge by counterbalancing the applied electric potential. Since the force generation is determined by the net charge density and electric field, the evolution of the features described above is critical to assess the performance of the DBD actuator.

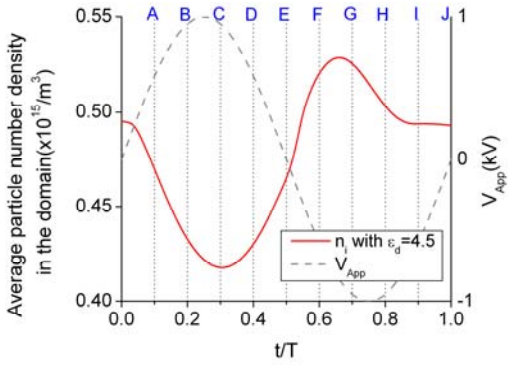

(a) domain-averaged ion number density over time

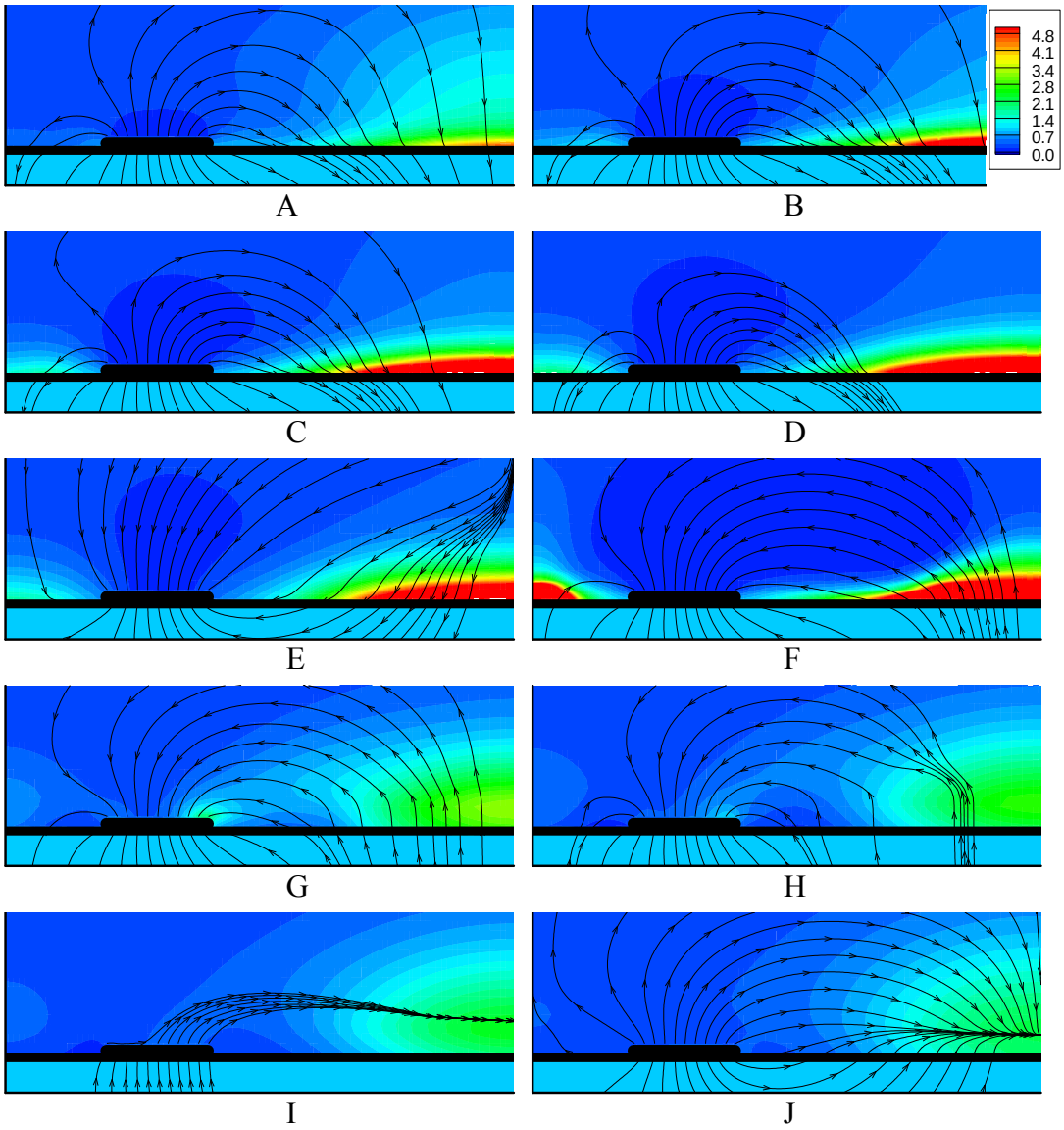

(b) instantaneous snapshots of the ion density [$\times 10^{15}/m^3$] at different instants over a cycle

Figure 2.8 Ion density evolution for one voltage cycle (5 kHz, 1 kV actuation).

Figure 2.8 shows the evolution of the domain-averaged ion density and contour snapshots corresponding to 10 different time instants. As the applied voltage increases, the ion density decreases and reaches its minimum at C, when the voltage starts to decrease. During this part of the cycle, ions move away from the exposed electrode that is charged positively, and they are deposited on the dielectric surface. As the voltage decreases at instants D, E and F, the surface charge build-up is decelerated and the electric potential generated by the built-up ions releases ions, resulting in a density increase. After reaching the maximum ion density between F and G when the negative exposed-electrode facilitates the charge release process from the dielectric surface, the ion density decreases to the equilibrium value where the ion release is balanced with the ion absorption through the exposed electrode.

The time history of the domain-averaged *x*-directional force and contour snapshots for the same case are shown in Figure 2.9. The average force consists of positive and negative parts, which correspond to the positive and negative half-cycles, respectively. In Figure 2.9(b), the positive force region in B, C and D (the region on the right dielectric surface), and the negative force regions in F, G and H (the regions near the exposed-electrode edge and on the left dielectric surface) are the regions where the ion density is high, which indicates that ions contribute mostly to the *x*-directional force generation. In the negative half-cycle of F, G and H, there is a region on the right dielectric surface with a positive *x*-directional force. This region is where the electron is deposited. Similar to ions in the first half-cycle, electrons accumulate in the second half-cycle, resulting in a polarity reversal at the end of the cycle. As a result, the negative average *x*-directional force at the end of the second half-cycle is choked. Since electrons deposit much faster than ions due to their higher mobility, this limiting process is more noticeable at the plateau region around I in the force time history.

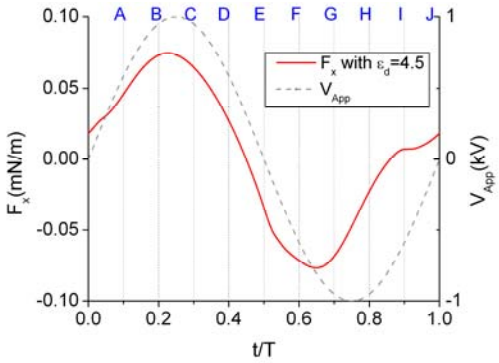

(a) domain-integrated x-directional force (F_x) variation in time

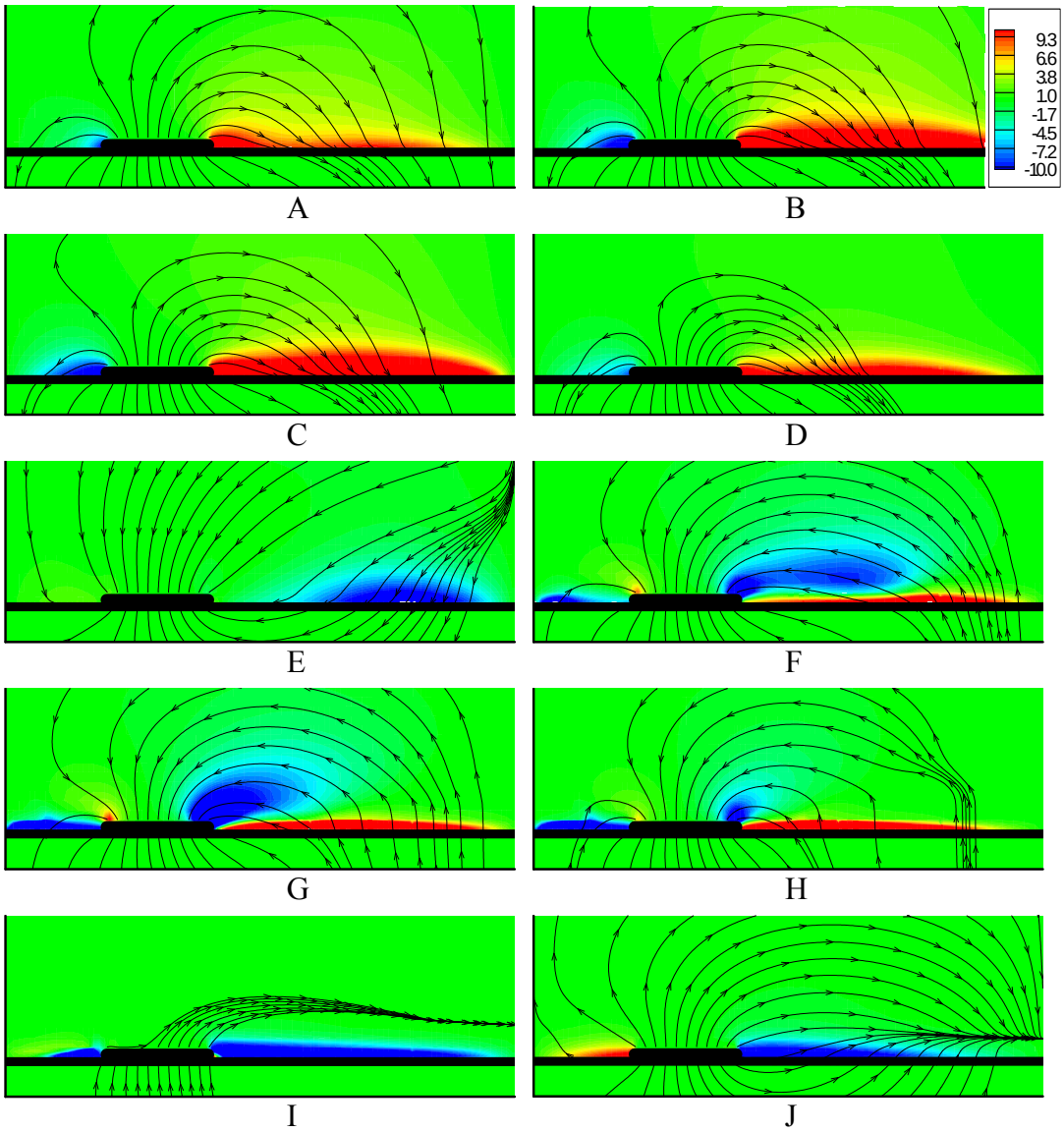

(b) instantaneous snapshots of the F_x field [N/m^3] at different instants over a cycle

Figure 2.9 Force evolution for one voltage cycle (5 kHz, 1 kV actuation).

In summary, the discharge limiting process due to charged particle accumulation is important in force generation. Specifically, the mobility disparity between ions and electrons results in different accumulation rates and force variations for two half-cycles. Considering the time-averaged impact of the force variation on the neutral fluid, this asymmetry in the force history is critical to the actuator performance. In the following sections, the impacts of the voltage frequency and dielectric constant on the force evolution are presented as examples of operational and material parametric effects.

2.4.2 Effects of voltage frequency

The voltage frequency is one of the operational parameters that influence the discharge process. In Figure 2.10, the time histories of the domain-integrated x-directional force, and electron and ion number densities are compared for two different frequencies of 5 and 20 kHz. As shown in Figure 2.10(a) and (b), the increased frequency provides a shorter time for ionization at each half-cycle, which means less ionization. In addition, the charge accumulation rate is lower in the normalized time scale with the higher frequency, resulting in the slower electron saturation at the end of the second half-cycle. Since the electron saturation is related to the discharge limiting, the case with higher frequency allows for the longer second-half or negative discharge in normalized time. As a result, the higher voltage frequency results in delayed and intensified negative force generation, as shown in Figure 2.10(c), which decreases the time-averaged force generation.

The time and domain averaged x-directional force for different voltage frequencies is shown in Table 2.2. For the test conditions, the average force decreases as the frequency increases.

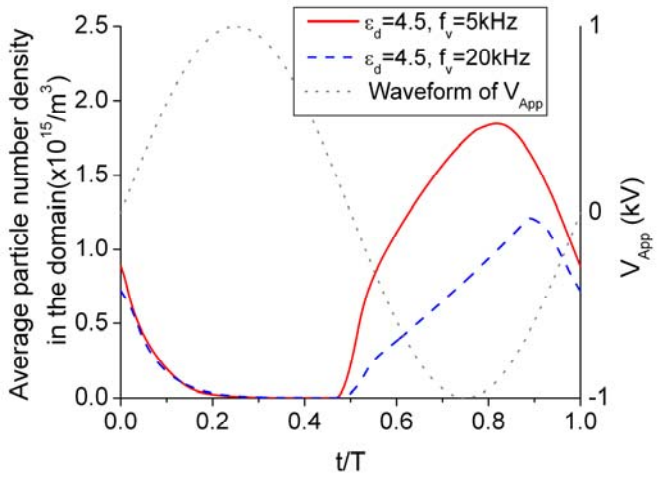

(a) domain-averaged electron number density

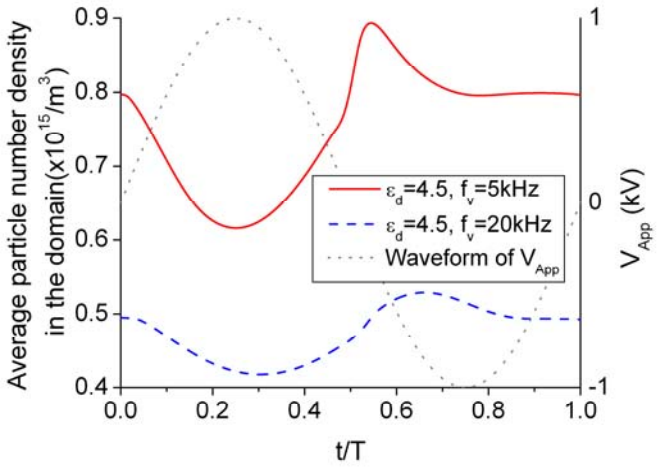

(b) domain-averaged ion number density

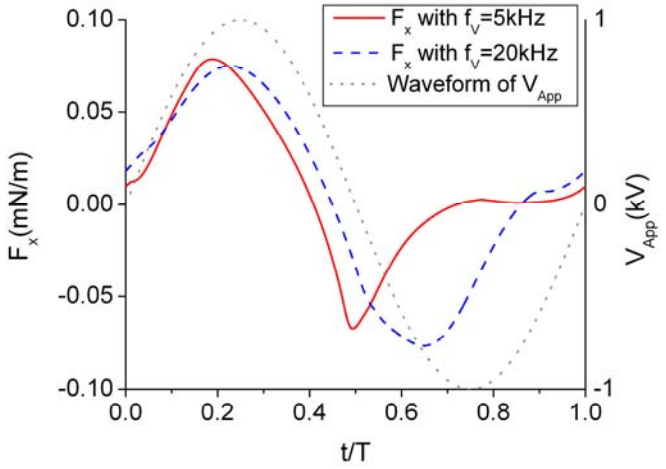

(c) domain-integrated *x*-directional force

Figure 2.10 Impact of the applied voltage frequency.

Table 2.2 Time-averaged domain-integrated *x*-directional force with the voltage frequency.

Frequency (kHz)	$F_{x,ST}$ (mN/m)
5	0.0125
10	0.0095
20	0.0059

2.4.3 Effects of dielectric constant

The dielectric constant is the permittivity ratio between a material and a vacuum, meaning the degree of polarization of the material for a given electric field. Under the same applied electric field, a material with a higher dielectric constant results in the decrease of the electric field and higher charge storage in the material. Since the ability of transmitting an electric field is determined by this constant, it also affects the electric field near the dielectric surface of the DBD actuator. Some materials with different dielectric constants are shown in Table 2.3. In this study, two different dielectric constants of ε_d = 1.0 and 30 are used for the DBD simulation while keeping the voltage and its frequency to 1 kV and 20 kHz, respectively. Although it may not be feasible to adopt insulators with those values of dielectric constant, the simulations shed light on the impact of the constant.

Table 2.3 Dielectric constant of materials (at 25 °C, 10 kHz).

Material	Air	Plasticell[99] (polyvinyl chloride)	Glass-epoxy[48]	Alumina	Thallium bromide[99]	Barium titanite
Dielectric constant	1.00054	1.04	5.2	10	30.3	1200

In Figure 2.11, the time histories of domain-integrated *x*-directional force and snapshots of the force density contours are shown. Compared to ε_d = 1, the force history of ε_d = 30 has much larger force variation. Particularly, the negative peaks at t/T = 0.7 and 1.0 are absent for ε_d = 1. The force contours at these two time instants in Figure 2.11(b) show the definite negative force regions – one near the exposed-electrode edge and the other on the

right dielectric surface – for $\varepsilon_d = 30$, which do not exist for $\varepsilon_d = 1$. This difference can be attributed to the deformation of the electric field line, and the different near-wall electric field strength and resulting charged particle movement when we change the dielectric constant.

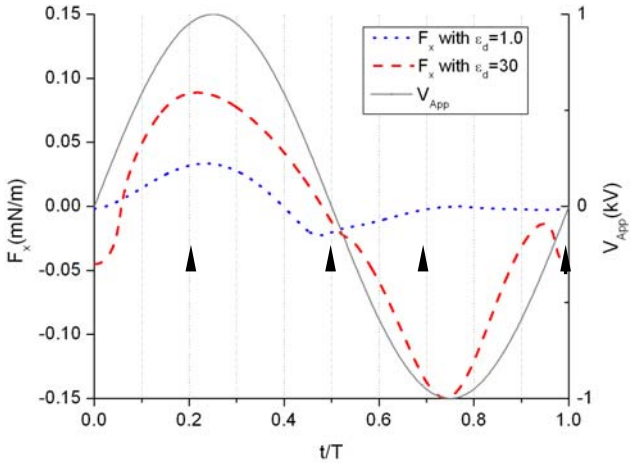

(a) domain-integrated force history

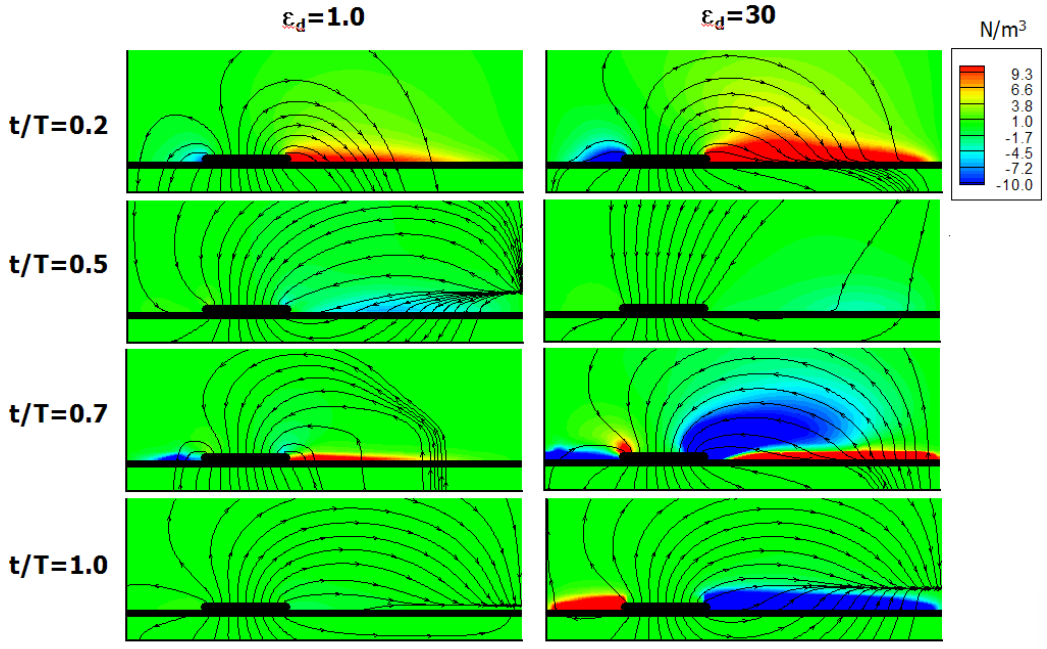

(b) F_x contour and electric field lines

Figure 2.11 Effect of the dielectric constant on force generation (20 kHz, 1 kV).

The electron and ion number density contours in Figure 2.12 show that the concentration of ions at t/T = 0.7 is distinctively high for ε_d = 30 near the upper electrode, which is consistent with the high-force region. On the other hand, the electron density contours show that the moments when the electron accumulation is saturated and the discharge limiting occurs are different for ε_d = 1 and ε_d = 30: t/T = 0.7 for the former and t/T = 1.0 for the later. In Figure 2.11, these moments correspond to the instant when the force plateau starts for ε_d = 1, and the instant when the second force dip occurs for ε_d = 30.

The x-directional electric field magnitudes (E_x) at different time instants are compared in Figure 2.13 as functions of the distance along the right dielectric surface from the right edge of the exposed electrode. The comparison of the two cases indicate that the higher dielectric constant results in a higher value and steeper slope of E_x. As mentioned, the higher dielectric constant means a higher polarization tendency and thus decreased electric potential near the wall, resulting in its higher gradient, i.e., electric field. This effect is prominent when the applied voltage reaches the positive and negative peaks at which the effect of the particle accumulation is weak. The magnitude and distribution of E_x is closely related to the generation of charged particles as well as instantaneous force generation. In Figure 2.13(b), the higher peak value near the electrode (x = 0) at t/T = 0.7 for ε_d = 30 explains the distinctive ion generation around this region mentioned above. Moreover, the flat part of the curve starting from x = 0.004 m corresponds to the region where the electron accumulation is saturated.

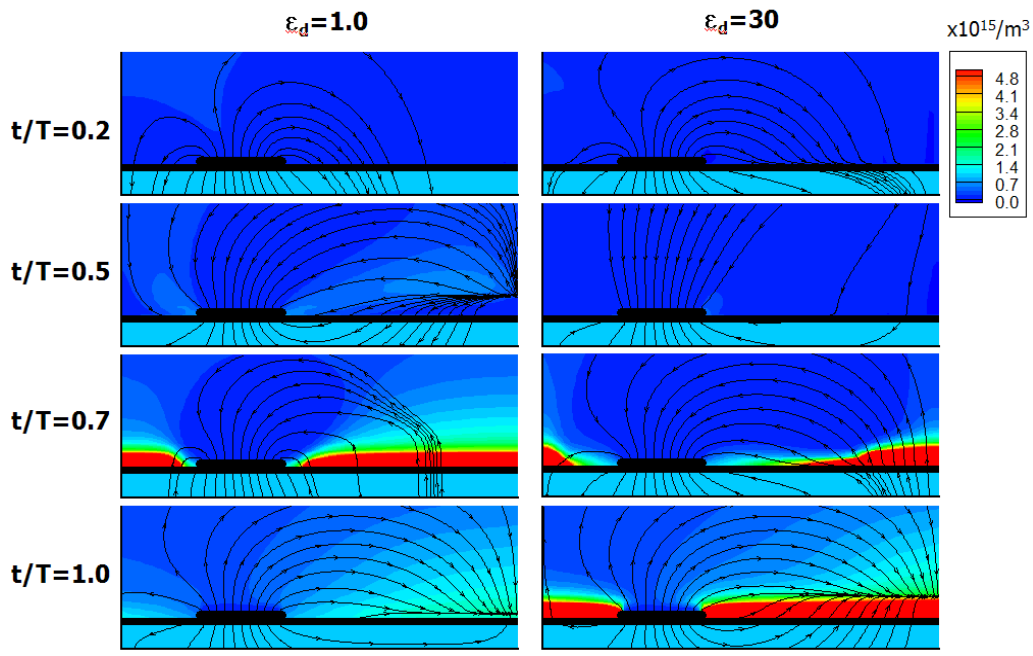

(a) electron number density contours and electric field lines

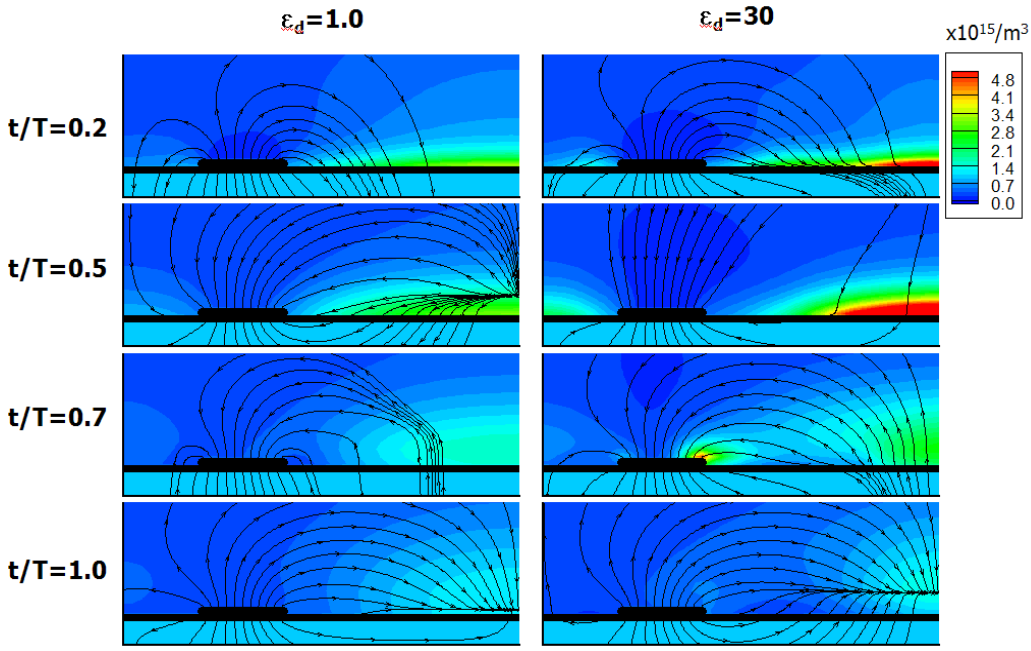

(b) ion number density contours and electric field lines

Figure 2.12 Effect of the dielectric constant on charge densities (20 kHz, 1 kV).

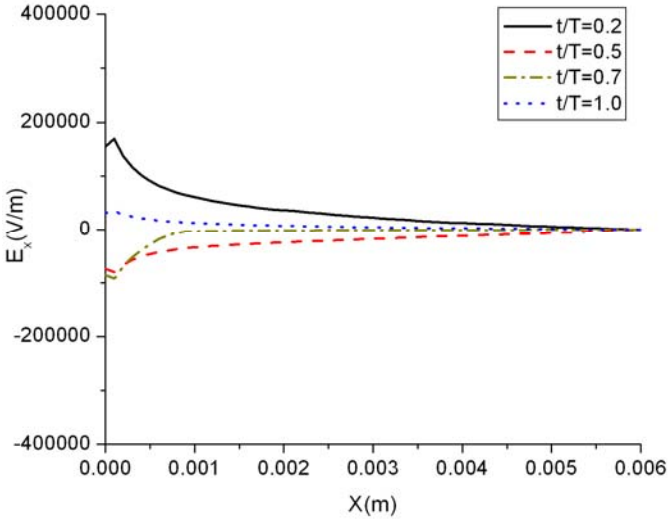

(a) $\varepsilon_d = 1.0$

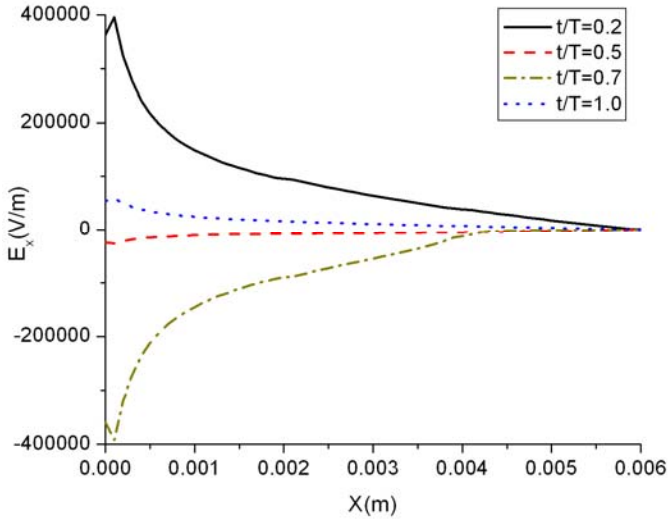

(b) $\varepsilon_d = 30$

Figure 2.13 *x*-directional electric field distribution along the dielectric surface.

2.4.4 Other effects

There are various geometric, operational and material parameters that affect the force generation of the DBD actuator. Among them, the impacts of the lower electrode size, waveform and voltage are also discussed in Jayaraman et al. (2008)[96]. In brief, a larger

lower-electrode results in increased force peaks and average force; the variation in the waveform, specifically in the positive and negative slopes, results in the charge generation rate; the induced force increases as the voltage amplitude increases according to the power law with the exponent close to 3.

2.5 Parametric study of DBD actuator

2.5.1 Surrogate modeling for design exploration

The observations in the previous sections imply that there are some design parameters which have non-trivial effects on the time- and domain-averaged force by affecting both the positive and the negative peak values of force evolution and asymmetry in its waveform. Among the operational and material parameters, three design variables − the dielectric constant of the insulator material ε_d, the frequency of the applied voltage f_v, and the positive-to-negative half cycle ratio r_f − are chosen in this study. The bounds for each design variable are based on the choice of materials and the range of widely adopted operation conditions. The objective functions are chosen so as to represent the actuator performance, namely the average x-directional force ($F_{x,ST}$) in the domain and average power input to the electrodes (P_T). The time-averaged domain-integrated Lorentzian force acting on the charged particles is assumed to be equivalent to the body force acting on the neutral gas, especially at atmospheric pressure conditions. The actual power input to the discharge device can be calculated by considering the charge and displacement currents in the volume of the medium[100]. For the purpose of simplicity in this study, only the charge current through the upper electrode is considered. The definitions and parameter ranges are presented in Table 2.4. Although the current investigation focuses on identifying the combination of the design variable to maximize $F_{x,ST}$ and minimize P_T, as will be discussed later, there are cases which produce negative $F_{x,ST}$. Therefore, the absolute value is used and one objective is chosen as minimizing $-|F_{x,ST}|$, where the minus sign is chosen for the convenience of minimizing both objective functions.

Table 2.4 Design variables, bounds and objective functions.

Design variables		Bounds
ε_d	Dielectric constant of the insulator	$2 \le \varepsilon_d \le 15$
f_v	Frequency of the applied voltage [kHz]	$5 \le f_v \le 20$
r_f	Positive-to-negative half cycle ratio	$0.5 \le r_f \le 1.5$
Objective functions		**Definitions**
$-\lvert F_{x,ST} \rvert$	Time-averaged domain-integrated x-directional force [mN/m]	$F_{x,ST} \triangleq \frac{1}{T}\int_T F_{x,S}(t)\,dt$ where $F_{x,S} \triangleq \int_S F_x(x,y,t)\,dA$ $F_x(x,y,t)$: x-directional force density [N/m^3]
P_T	Power input for one cycle by the charge current through the upper electrode [W]	$P_T \triangleq \frac{1}{T}\int_T I(t)V_{app}(t)\,dt$ where net charge flux, $I(t) = \int_{l_{eu}} \left\{ q_i n_i(t) u_{y,i}(t) - q_e n_e(t) u_{y,e}(t) \right\} dx$ S: gas domain area T: period of the applied voltage

Since the number of sampling points is restricted by the computational cost, the design of experiments needs to be chosen carefully. In this study, a two-stage surrogate modeling process is used. In the first stage, in order to assess the entire design space, FCCD combined with LHS is used to support the design of experiments. The choice of the design of experiments relies on the observation that FCCD is efficient for second-order design in a cuboid design space by spreading the design points towards bounds, and LHS provides more space-filling points with an even chance for each design variable. Based on the outcome of the global investigation, we develop refined surrogate models focusing

on the regions of favorable DBD performance. Since the main interests in the refined regions are in the interior portion of the sub-domains, the distance-based design combined with LHS is used. Since the distance-based sampling minimizes the void of sampling in the design space, it efficiently distributes points in the refined space, whose constraints are curved surfaces in the objective space. In summary, the sampling points are chosen to characterize the entire design space, followed by a refinement study focusing on the regions of interests. The number of sampling points at each design of experiments is set to 20, which is double the number of coefficients of a 2^{nd} order polynomial response surface representation. The refinement study will be presented in detail later.

Four different surrogate models, namely 2^{nd} order PRS, KRG, RBNN, and PWS, are adopted in this study, and the relevant functions and parameters are presented in Table 2.5. As mentioned earlier, the weight of each model in the PWS is set to allow higher contribution to the surrogate with the smaller PRESS.

Table 2.5 Functions and parameters for the surrogate models.

Surrogate model	Functions and parameters	
Kriging	Correlation function:	Gaussian
	Regression model:	Polynomial
	Initial guess of θ_i:	15
Radial basis neural network	Spread, b:	0.75
	Goal:	$\{0.025 \times (sample\ mean)\}^2$

Main and total effects of variables in the global sensitivity analysis are computed using the Gaussian-quadrature. In order to identify the appropriate design variables capable of promoting the two objectives – force maximization and power minimization – the Pareto optimal set is constructed by seeking a set of points that are not dominated by any other points in the objective function space. A survey of the trade-off points on the Pareto front

is accompanied by a few design space refinements based on the error statistics of the surrogate models in the original design space.

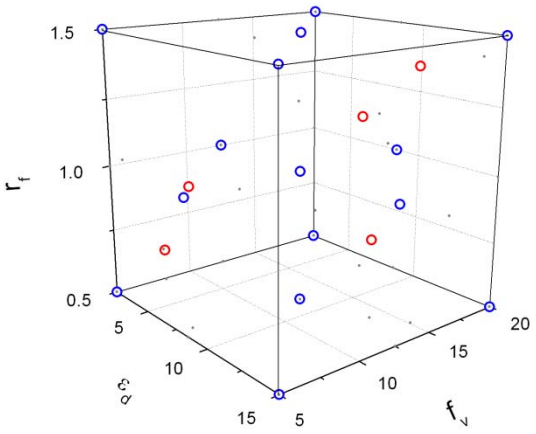

(a) design of experiments (FCCD + LHS)

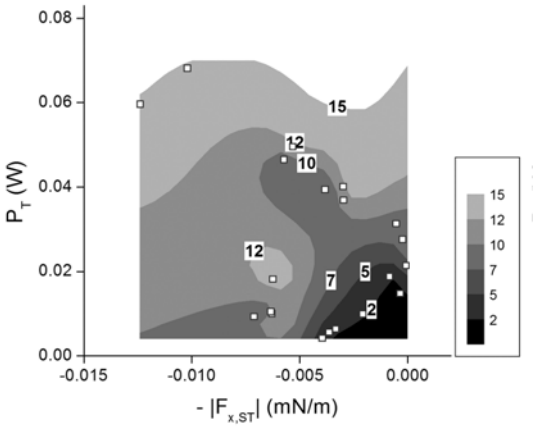

(b) simulation results and ε_d contours

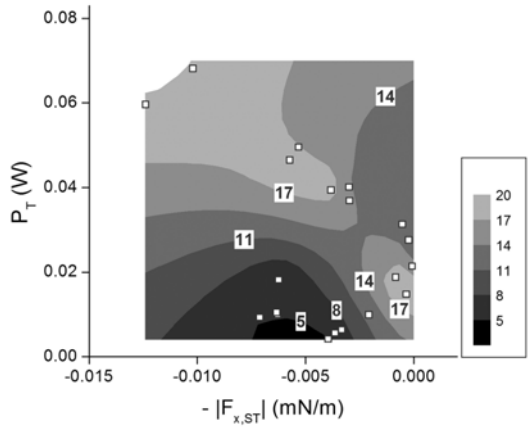

(c) simulation results and f_v [kHz] contours

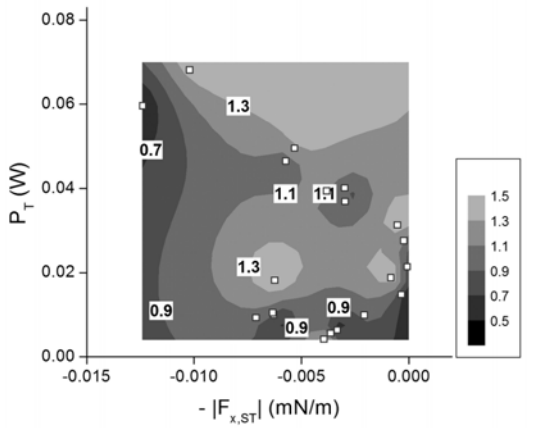

(d) simulation results and r_f contours

Figure 2.14 Design points in design space and objective function space – level 0.

2.5.2 Design exploration

The first level design of experiments, level 0 using the combination of 15 FCCD points and 5 LHS points and the simulation result of those 20 points are presented in Figure 2.14. Although the sampled points are well distributed in the design space, the response points cluster in some parts of the response space, as shown in Figure 2.14(a), (b) and (c). As a

result it is hard to get an idea of the objective function dependency of the design variables with sufficient accuracy, but some noteworthy features can be observed from the contours. With the higher dielectric constant of the insulator both power and magnitude of force, $|F_{x,ST}|$ tend to increase. In the context of the current conditions, the lower frequency generally leads to lower power. The ratio of the first and second half cycle shows more complex effects and makes it hard to deduce any tendency.

The surrogate models are obtained using these sampled points and their PRESS errors are presented in Table 2.6. Due to the insufficient number of sampled points and their complex response, significant PRESS errors exist at this level especially in force prediction. For this case, KRG shows the best performance in predicting the force while PWS does the same for power.

Table 2.6 PRESS of the surrogate models – level 0.

Objective functions	KRG	PRS	RBNN	PWS
$-\left\|F_{x,ST}\right\|$	0.0020 (16)*	0.0027 (22)	0.0095 (77)	0.0028 (23)
P_T	0.0032 (5.0)	0.0033 (5.2)	0.0063 (9.9)	0.0023 (3.6)

*: ( ) % = 100 × PRESS / ($X_{max} - X_{min}$), $X = -|F_{x,ST}|$ or P_T in level 0.

In order to explore the objective function distribution corresponding to the design space, a grid with 31^3 points evenly distributed in the whole design space is employed. Among the surrogates, the prediction points of PWS along with the design points are shown in Figure 2.15. It can be observed that the Pareto front is not continuous and there are two distinct regions that are marked with two windows and correspond to the higher magnitude of force generation. Though they both lie on the same side of the force axis due to our adopting the absolute values of the force, the one with higher power corresponds to the negative – negative *x*-direction in Figure 2.4 – force generation, and the lower to the positive. In terms of magnitude, the negative force generation is larger than the positive. Simply changing the direction of the actuator can be beneficial for maximizing the force generation. On the other hand, the region corresponding to the

positive force generation accompanies a better power efficiency. The power ratio between those two regions is about 5~6 compared to the force ratio of 2.

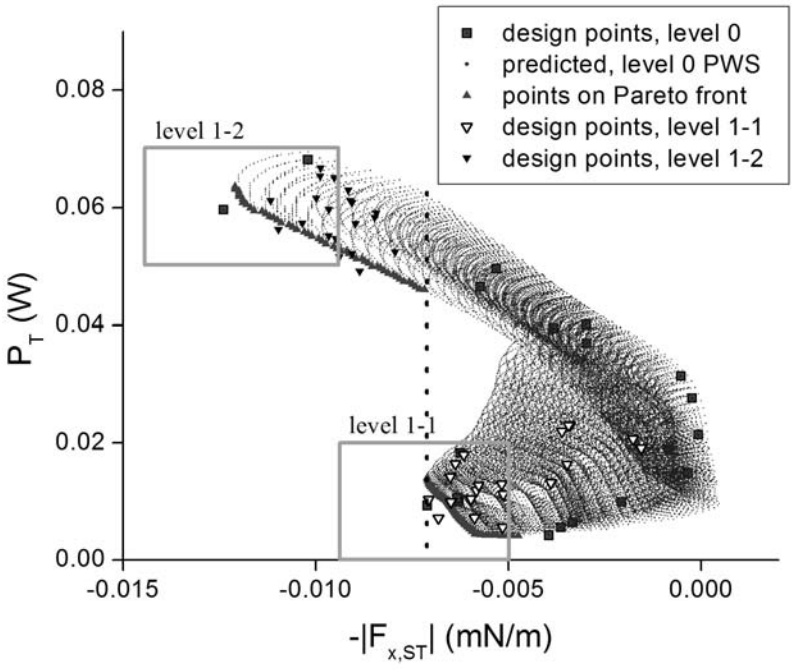

Figure 2.15 Design and predicted points, and Pareto front by PWS in level 0.

The mechanism of the force generation over the two half-cycles has been a subject of interest with different suggestions by researchers, such as whether it consists of two consecutive positive or positive-negative alternating patterns[37]. It has been reported by some researchers that the dominant positive and small negative force generations for the first and second half cycles respectively exist for sinusoidal voltage excitation[96, 101] or pulse-mode operation[102]. Because of the charged species with different polarities and other factors, such as geometry, it is difficult to compare the solution directly. Also, in the numerical models there are other factors such as boundary treatment, domain size and surface reaction modeling that affect the overall force generation. In the current study, there are positive and negative alternating contributions of force generation during the two half cycles, and in a certain part of design space, the negative portion exceeds the positive, resulting in a negative time-averaged force generation.

As Figure 2.15 shows, since the distribution of sampled points near the Pareto fronts are too sparse to resolve the regions of interest properly, two windowed regions are used as the constraints for design space refinement.

Level 1-1, low power region: $-0.009 \le -\left|F_{x,ST}\right| \le -0.005$ [mN/m]

$0 \le P_T \le 0.02$ [W]

Level 1-2, high power region: $-0.014 \le -\left|F_{x,ST}\right| \le -0.009$ [mN/m]

$0.05 \le P_T \le 0.07$ [W]

The design variable constraints corresponding to these objective function constraints, namely design-space-constraints, are generated based on the surrogate models at level 0. In order to generate the constraint surfaces, responses of a set of grid points uniformly distributed in the design space are obtained by using the surrogate models, and the surfaces confining the points whose responses satisfy the objective function constraints are specified. Although PWS has a smaller PRESS error in P_T as presented in Table 2.6, the design space confined by its design-space-constraints is included in that of KRG, and the refined regions are chosen conservatively to cover as much space as possible. Figure 2.16 shows the iso-force and iso-power surfaces and the design-space-constraint[56] surfaces based on KRG (blue is for the lower bounds and red the upper bounds). Considering the lower and upper bounds of the objectives, each level has one refined space along with constraint surfaces. Since these surfaces are contours of constant force or power, it can be said based on their slopes that the force generation is relatively less sensitive to the dielectric constant than power.

Since the design space corresponding to level 1-1 and 1-2 constraint windows is an irregular shape, it is impossible to use the design of experiments for a rectangular hexahedron or sphere. For the design of experiments at the refined level, in order to sufficiently characterize the design space, the LHS is utilized to generate 5000 points. Then, 20 points are selected by maximizing the minimum distance between those points.

The design points generated by this approach are also shown in Figure 2.16 along with the constraint surfaces.

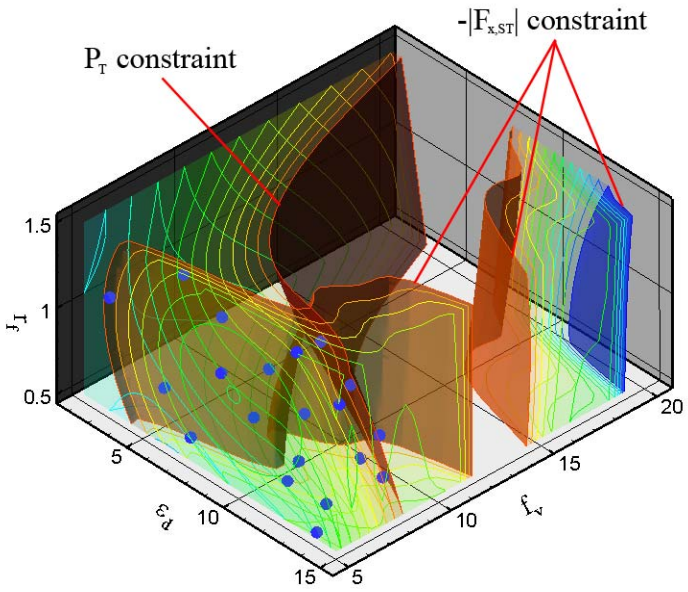

(a) level 1-1: low power region

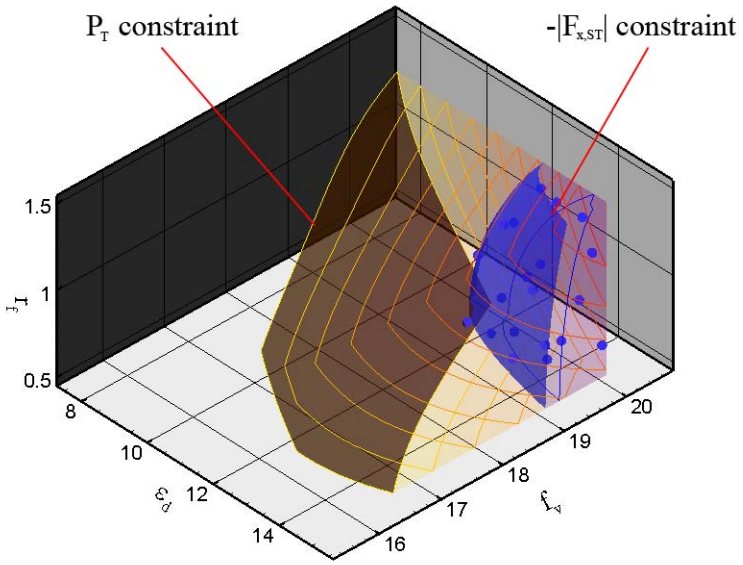

(b) level 1-2: high power region

Figure 2.16 Constraints and design points for the design space refinement.

The simulated result of design points in each region is used to generate the surrogate models. With the refinement, model prediction accuracy is improved both in relative and absolute measures as shown in Table 2.7 and Table 2.8. It can be seen that the PRESS error for the polynomial response surface in the refined levels is much improved, which means that the physical complexity is adequately captured in these refined regions.

Table 2.7 PRESS of the surrogate models – level 1-1.

Objective functions	KRG	PRS	RBNN	PWS
$-\lvert F_{x,ST} \rvert$	5.2×10^{-4} (9.5)*	3.7×10^{-4} (6.7)	2.7×10^{-4} (4.9)	3.3×10^{-4} (6.0)
P_T	1.9×10^{-4} (1.1)	1.4×10^{-4} (0.80)	6.9×10^{-4} (3.9)	1.2×10^{-4} (0.69)

*: ( ) % = 100 × PRESS / ($X_{max} - X_{min}$), $X = -|F_{x,ST}|$ or P_T in level 1-1.

Table 2.8 PRESS of the surrogate models – level 1-2.

Objective functions	KRG	PRS	RBNN	PWS
$-\lvert F_{x,ST} \rvert$	1.2×10^{-4} (3.8)*	1.1×10^{-4} (3.4)	3.4×10^{-4} (10.6)	1.1×10^{-4} (3.4)
P_T	2.0×10^{-4} (1.1)	0.55×10^{-4} (0.31)	9.4×10^{-4} (5.3)	0.90×10^{-4} (0.51)

*: ( ) % = 100 × PRESS / ($X_{max} - X_{min}$), $X = -|F_{x,ST}|$ or P_T in level 1-2.

Using the PWS in level 1-1 and PRS level 1-2, which have best PRESS values, the Pareto front is constructed again for each data set, as shown in Figure 2.17(a) and (b), along with the predicted points by the surrogate models. It can be verified that the majority of design points – 13 in the low power region and 15 in the high power region – reside in the constraint regions, which suggests the prediction accuracy of surrogate models based on level 0 is satisfactory, although the projected position of each design point may differ by at least as much as the PRESS values. Although there are differences between the Pareto fronts using level 0 and those using level 1-1 and 1-2, there is consistency in the shape and orientation of the fronts.

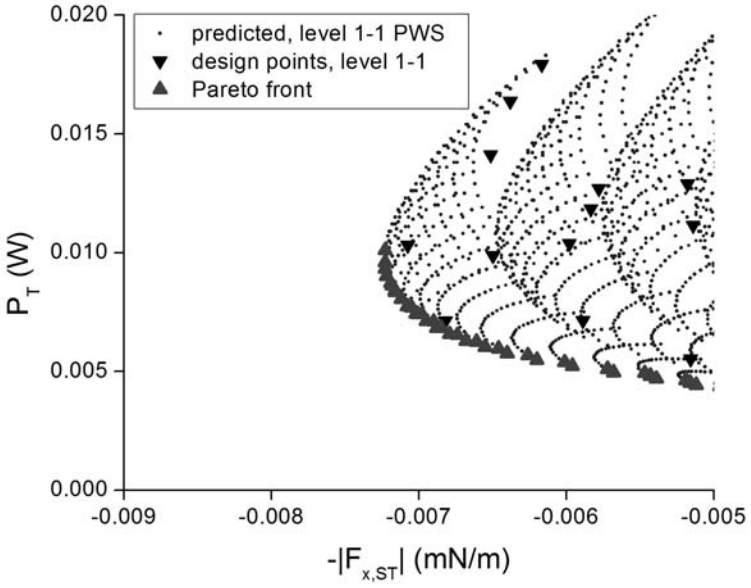

(a) level 1-1: PWS

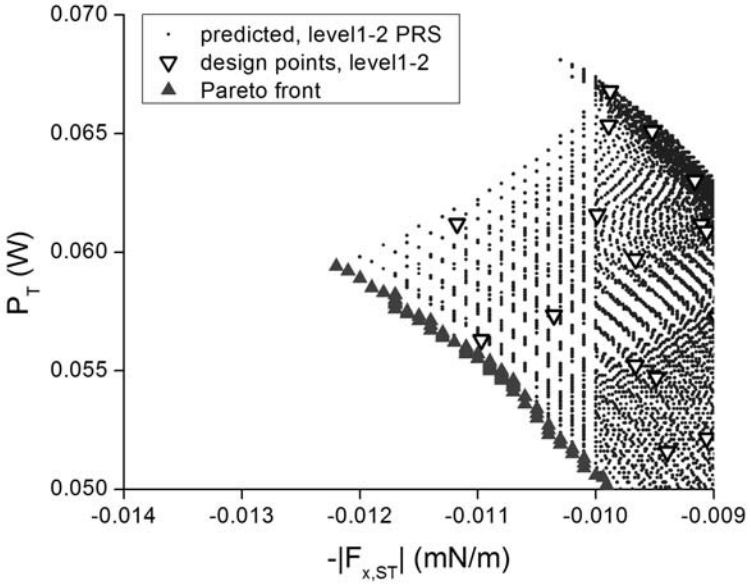

(b) level 1-2: PRS

Figure 2.17 Design and predicted points, and Pareto front in refined levels.

2.5.3 Two distinctive regions and Pareto fronts

To investigate the design variable variation around the Pareto front branches, surrogate models are used as functions to represent the design space regions that correspond to the fronts. The region calculated based on level 0 is presented in Figure 2.18(a) and based on level 1 in Figure 2.18(b). Compared to the prediction by the level 0 surrogate model, the level 1 shows more coherent regions that correspond to the two Pareto front branches respectively. The two branches with the high and low power consumptions are separated by the whole design space in terms of the applied voltage frequency.

For the two regions, the most efficient points in force generation, i.e., minimum in $-|F_{x,ST}|$, are separated from each other by the whole design space, although they occur at the same frequency of applied voltage f_v. It can be observed that, when following the Pareto front line of the high power region, the dielectric constant ε_d is the most influential variable, while for the Pareto front line of the low power region, both ε_d and r_f need to be varied. Though it may be inconvenient to vary the material constant – such as ε_d – to accommodate a desired objective function state, if proper design variables are chosen, this type of information can be used to establish a basis for the performance of these actuators as effective flow control devices.

One can identify multiple optimal points on the design variable bounds – one for f_v and the other for f_v and r_f in Figure 2.18(b). To identify desirable performance of the actuator, the design space can be expanded. However, care needs to be taken to consider the discharge operating mode, which is known to significantly change the charge densities as well as the power consumption.

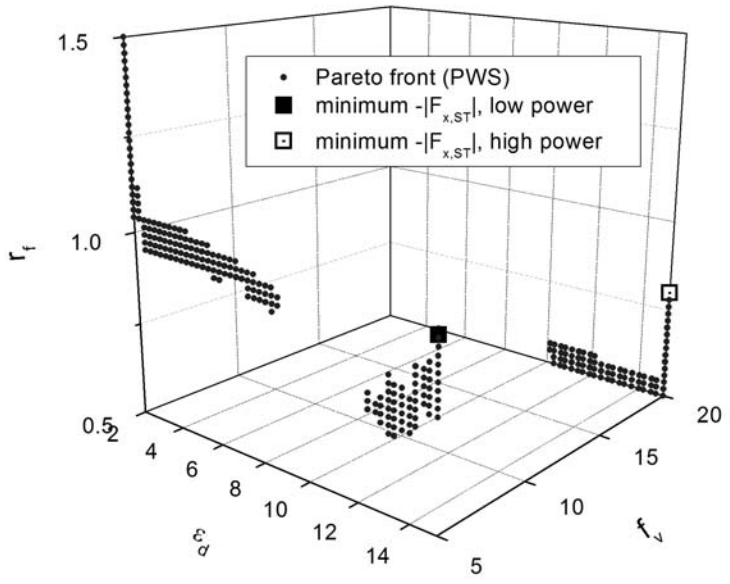

(a) level 0

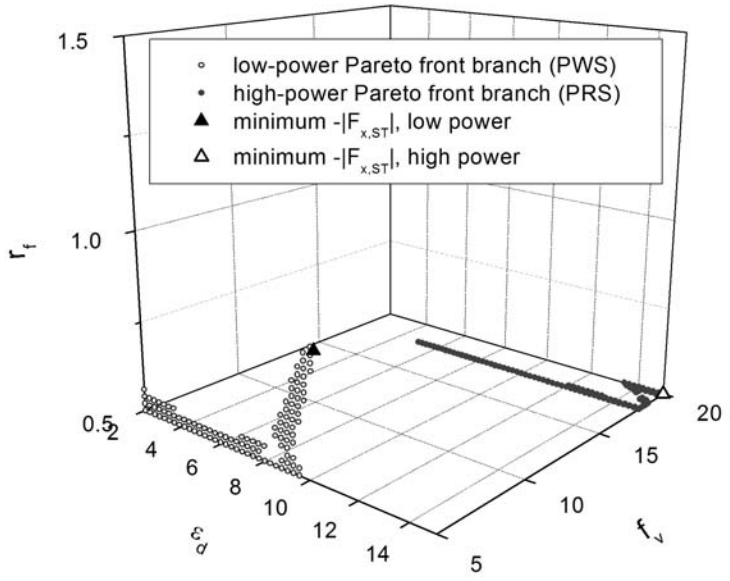

(b) level 1-1 and level 1-2

Figure 2.18 Prediction points on the Pareto front in the objective space along with two design points with minimum -|$F_{x,ST}$| in low and high power regions.

In order to investigate distinctive phenomena in these regions, two points corresponding to the minimum $-|F_{x,ST}|$ conditions are selected and the time history solutions are compared in Figure 2.19 and Figure 2.20. In Figure 2.19(a) and (b) it can be observed that for the case with lower frequency that belongs to the low power region, domain-averaged ion number density is higher. This can be explained by considering the fact that lower frequency allows more time to generate charged particles, as explained in 2.4.2. The electron saturation instances in these cases – about $t/T = 0.8$ in the low power and 0.9 in the high power – coincide with the start of the plateau or second dip in Figure 2.20, which is also mentioned previously as one of the key features affecting the force generation.

Based on the force history results, from which it can be deduced the ratio of first and second half cycles r_f is an effective parameter for changing the force history profile, the ratio is chosen as one of the design variables in this study. Although positive force belongs to the first half cycle and negative to the second, elongating the period of each part in the applied voltage source does not necessarily induce increased force either in the positive or the negative direction. While decreasing r_f, i.e., increasing the second half cycle corresponds to the decreased $-|F_{x,ST}|$ point in the high power region, increasing r_f does not mean increasing the duration of the positive force cycle. The value of r_f corresponding to the maximum force generation in the positive x-direction is about 0.8 in the low power region according to the multiple surrogate model. The reason is that generating the positive force is mainly related to the plateau region of the second half cycle in the $F_{x,S}$ time history, as shown in Figure 2.20.

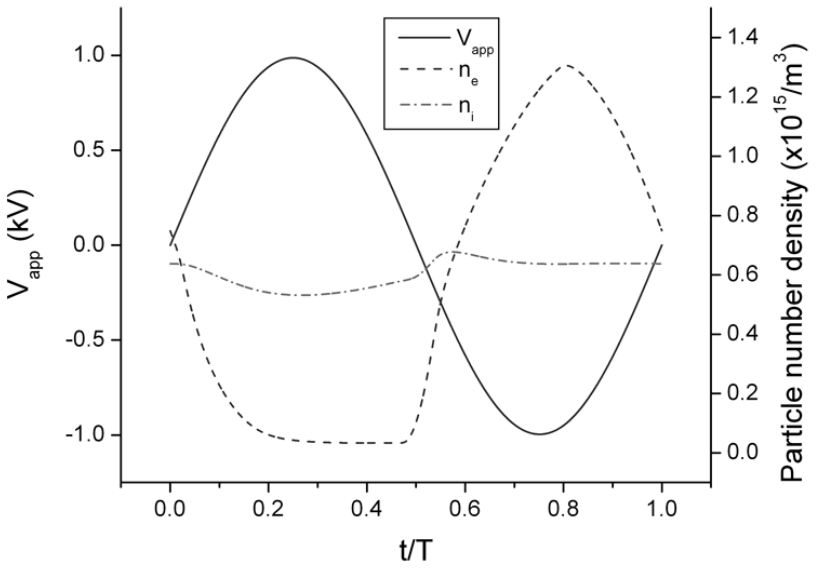

(a) low power region: $\varepsilon_d = 8.5, f_v = 5.0$ and $r_f = 1.0$

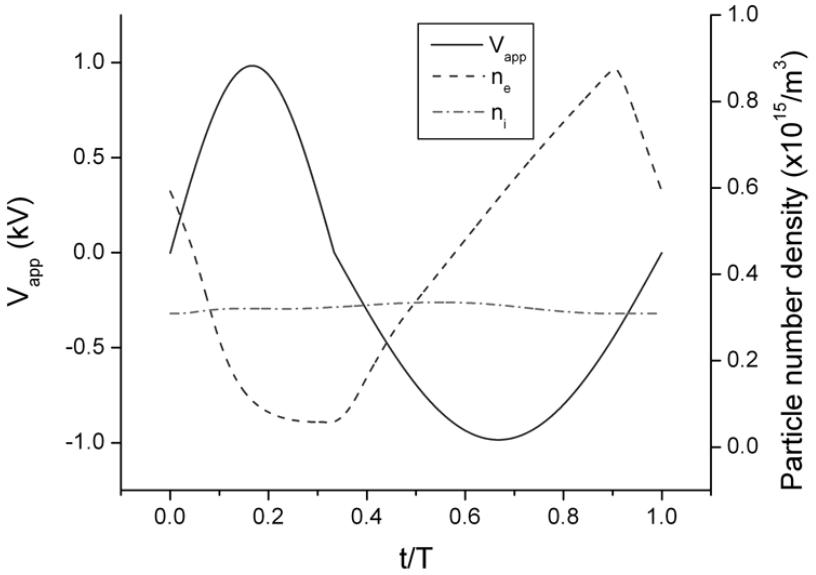

(b) high power region: $\varepsilon_d = 15, f_v = 20$ and $r_f = 0.5$

Figure 2.19 Domain-averaged particle number density evolutions for two design points.

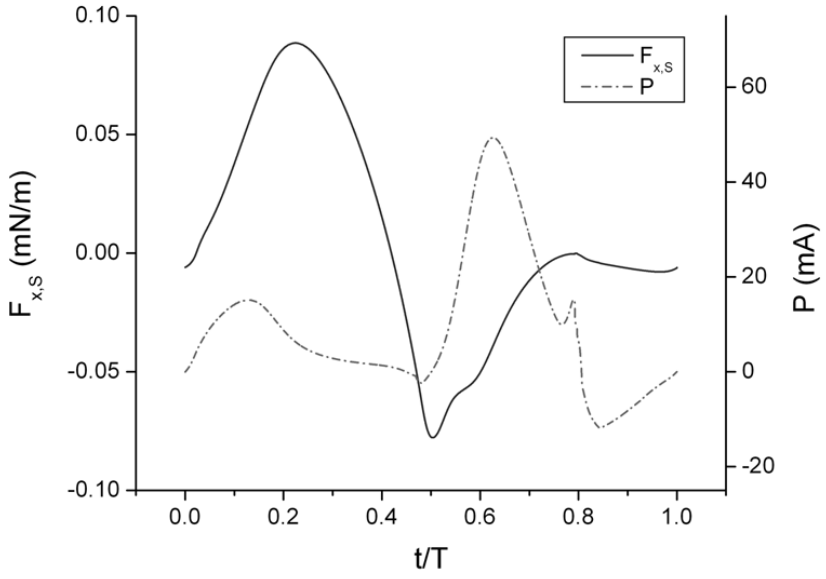

(a) low power region: $\varepsilon_d = 8.5$, $f_v = 5.0$ and $r_f = 1.0$

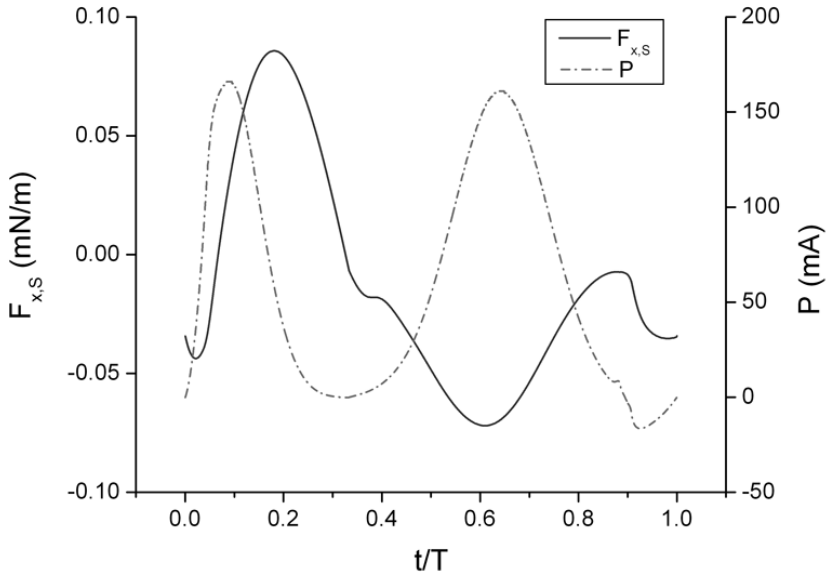

(b) high power region: $\varepsilon_d = 15$, $f_v = 20$ and $r_f = 0.5$

Figure 2.20 Domain-integrated *x*-directional force and power evolutions for two design points.

This phenomenon is mainly caused by the difference in the amount and evolution of the electron and ion clouds that reside on the dielectric surface. In Figure 2.21, instantaneous contours of main physical quantities, especially around the upper electrode, are presented at the moment of $t/T = 0.95$, when the phase change in applied voltage is about to occur. At this instant, as pointed out in 2.4.1, the force generation mainly occurs near the dielectric wall and exposed electrode region caused by the electrons accumulated on the dielectric surface and strong electric field near the edge of electrode. For the low power region, ion clouds having been repelled from the surface through the second half cycle compensate the applied electric field, as in Figure 2.21(d), resulting in the small magnitude of negative force generation in the later part of the second half cycle, i.e., the plateau region. On the other hand, for the high power region, this ion cloud is much weaker, and there is a strong electric field near the upper electrode. As a result, the electron density near the wall is higher, causing the second negative peak at the end of the second half cycle.

On the other hand, the dielectric constant affects the asymmetry between the first and the second half cycles, as well as the amplitude of the generated force. These two effects of the dielectric constant contribute to the average force through competing mechanisms. For example, by increasing the dielectric constant one can increase the amplitude of the force history and consequently increase the time-averaged force generation, but the asymmetry between the two half cycles also decreases, thus decreasing the time-averaged force generation. As a result, for the low power region, the efficient force generation in Figure 2.18 occurs at $\varepsilon_d = 10.2$, which is not on the edge of the design variable range, $2.0 \leq \varepsilon_d \leq 15.0$. However, for the high power region, it occurs at the maximum value, 15.0.

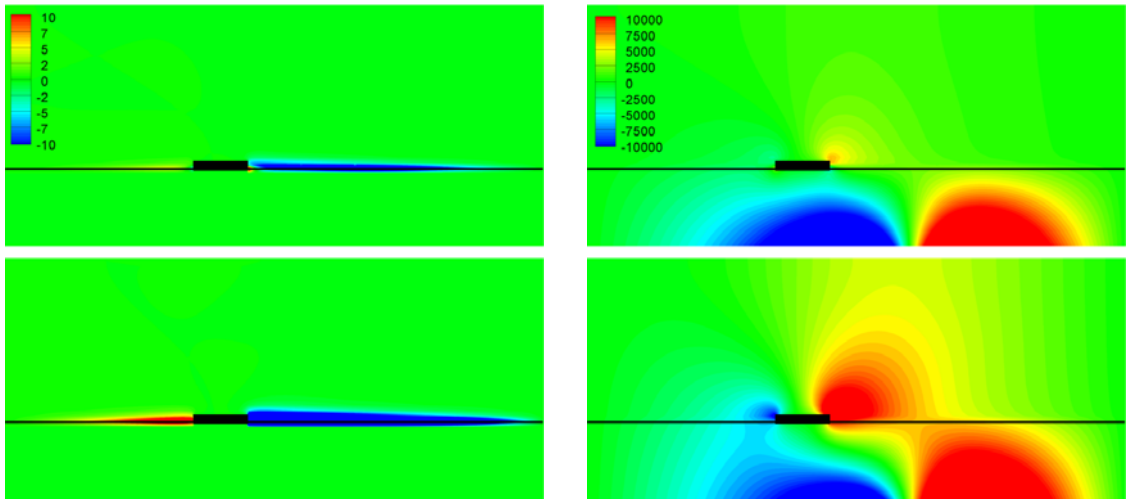

(a) F_x [N/m^3] (b) E_x [V/m]

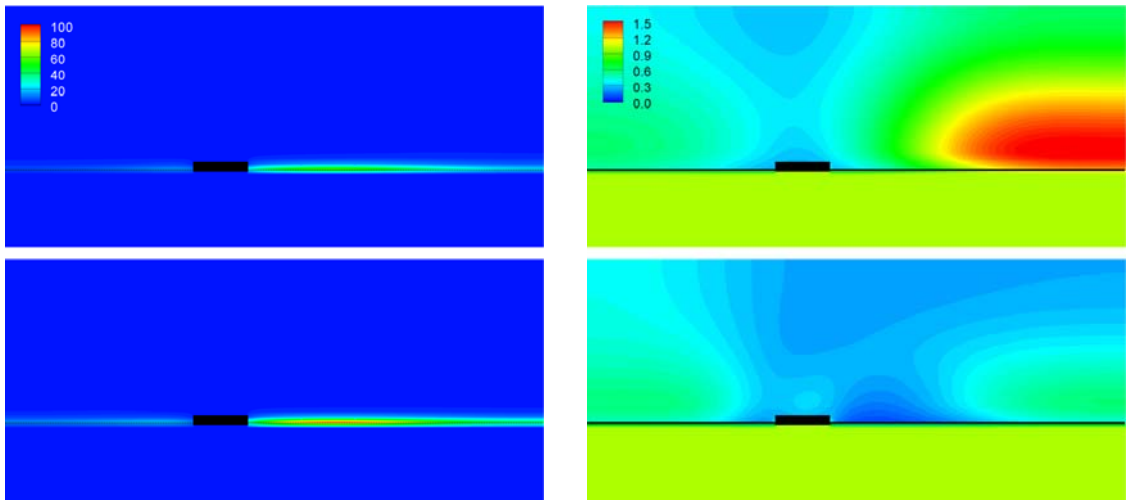

(c) n_e [$\times 10^{15}$ m^{-3}] (d) n_i [$\times 10^{15}$ m^{-3}]

Figure 2.21 Solution contour plots at t/T = 0.95 (upper: low power region, lower: high power region).

According to the present result, the average force generation has more monotonic dependency on the frequency of the applied voltage, at least around the Pareto fronts. For the high power region the higher frequency induces the larger average force, and for the lower power region the opposite occurs. But this is because we are dealing with the magnitude of the average force generation while ignoring its orientation. As mentioned earlier, the lower power region corresponds to the positive force generation, while the high power region corresponds to the negative force generation.

2.5.4 Global sensitivity analysis and dependency on parameters

Figure 2.22 shows the result of the variance-based, non-parametric global sensitivity analysis for each refined level. Compared to the level 1-2, level 1-1 shows stronger parametric correlations, which can be identified from the difference between total and main sensitivities. Also, the voltage frequency f_v in level 1-1 has a significant effect on both the average force and power. On the other hand, in the high power region (level 1-2) the effect of the positive-to-negative time ratio r_f is prominent compared to that of f_v, while the insulator dielectric constant is always important.

The local dependencies of the objective functions on each design variable are investigated by employing the surrogates with the best PRESS values shown in Table 2.7 and Table 2.8 for $|F_{x,ST}|$ and P_T. The performance variations as functions of each design variable are compared while fixing the rest of the variables. While r_f is kept as 1.0, the sensitivity on the applied frequency and dielectric constant is shown in Figure 2.23. For the refined level 1-1 in Figure 2.23(a), the magnitude of force increases with the dielectric constant for f_v = 5 kHz, but decreases for f_v = 10 kHz. However, this trend reverses in level 1-2, as in Figure 2.23(b) – the magnitude of force increases faster for larger f_v. A similar trend is observed in the effect of f_v with constant ε_d. The average force generation decreases with larger f_v in level 1-1. In level 1-2, on the other hand, although the frequency variation range is small, the magnitude of force increases with increasing frequency as shown in Figure 2.23(b). The force sensitivity to the voltage frequency in level 1-1 is different from the frequency impacts reported by other studies. For example, it has been reported that for the frequency range of $O(1)$ kilohertz, body force linearly increases with frequency[85, 102] or saturates at around 2 kHz[47], which is a relatively low frequency. Along with previously mentioned negative average force generation, this aspect needs further examination while the current discharge model is improved.

The power increases monotonically with the dielectric constant and applied frequency, which is consistent with experimental results[49], although the average power used in this study does not accurately reflect the overall power input to the actuator.

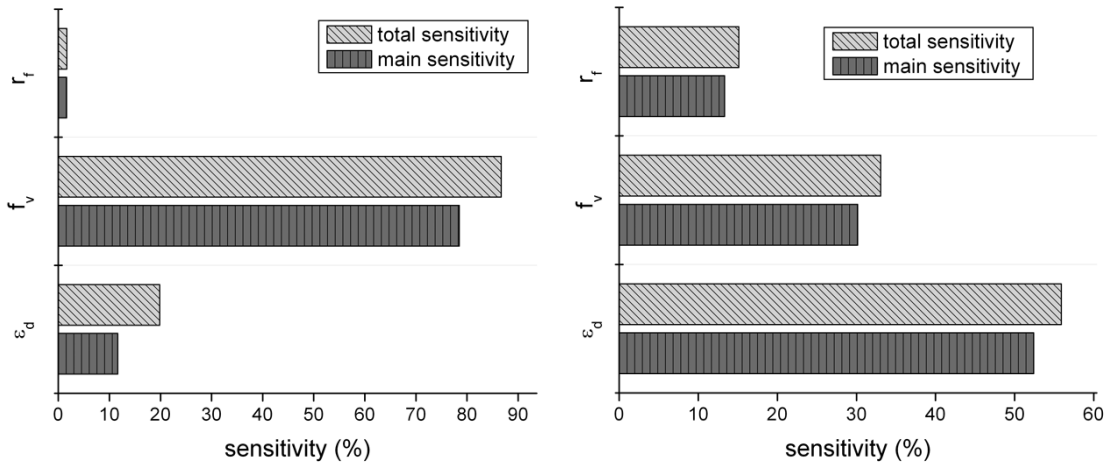

(a) $F_{x,ST}$ at level 1-1

(b) P_T at level 1-1

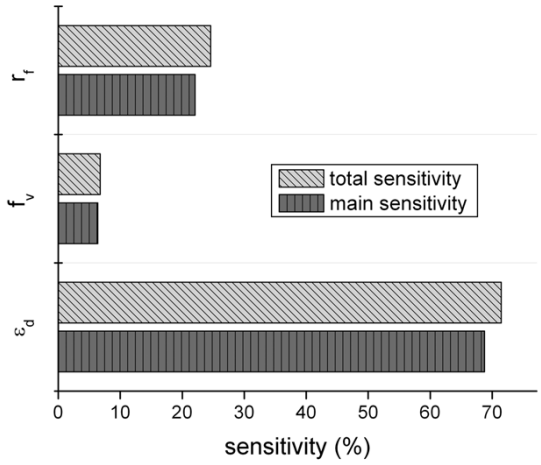

(c) $F_{x,ST}$ at level 1-2

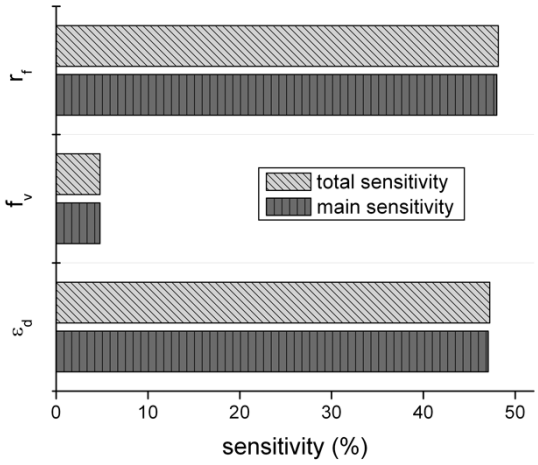

(d) P_T at level 1-2

Figure 2.22 Global sensitivity analysis result.

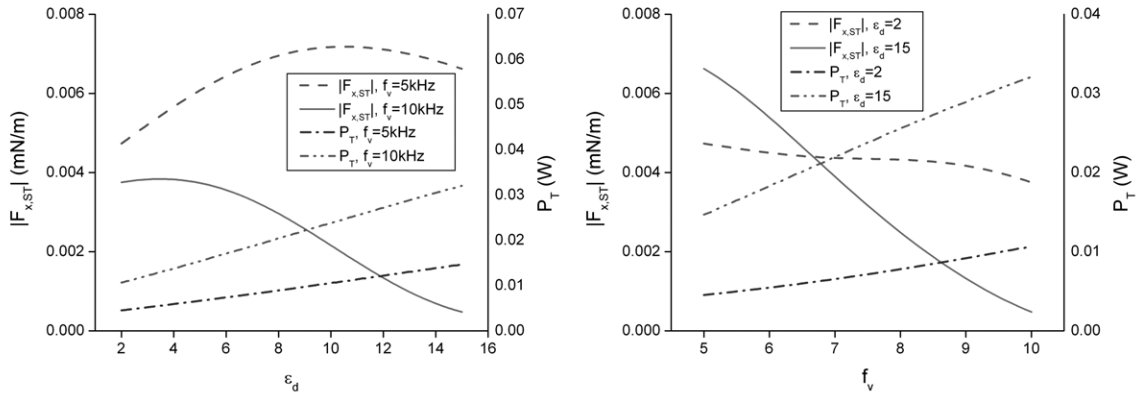

(a) r_f = 1.0 at level 1-1

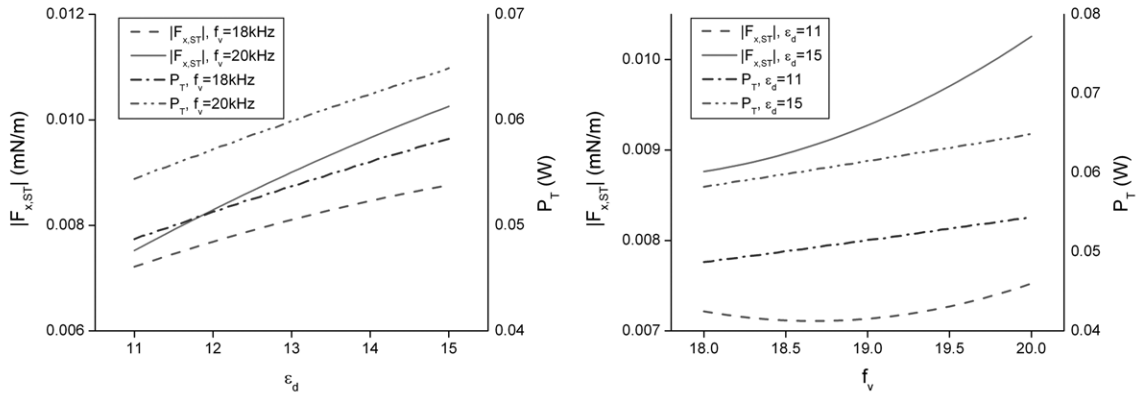

(b) r_f = 1.0 at level 1-2

Figure 2.23 Local dependency of performance on parameters.

2.6 Surrogate-based body-force model

Although the unsteady discharge simulations can provide detailed actuator physics, the significant difference in plasma and neutral flow time scales at low-Reynolds number applications makes first-principle-based numerical approaches inefficient and infeasible. For example, the typical time scale of DBD operation is $O(10)$ kHz or $O(10^{-4})$ sec, which is 1000 times faster than the convection time scale of $O(10^{-1})$ sec for the flow over a wing with the chord length of 0.5 m and flow speed of 5 m/s, i.e., $Re = 1.7\times10^5$ under standard atmospheric conditions. This time-scale disparity justifies the application of quasi-steady

body-force models, which assume that the induced airflow only sees the impact of the DBD actuation averaged over the discharge time scale.

Based on this justification, various simplified DBD models are suggested to decrease the computational cost of DBD simulations. Shyy *et al.* (2002)[37] approximate the discharge area with a triangular region of bilinear electric field and constant charge density. Hall *et al.* (2005)[52] use a doublet in potential flow to mimic the DBD actuator. Suzen *et al.* (2005)[52] solve electric potential and net charge distribution equations with the half-Gaussian charge distribution. Orlov *et al*. (2006)[53] propose a lumped-element model which provides boundary conditions for the electric field equation and calculate the body force vector using the time variant force field. Opaits *et al.* (2010)[103] adopt a self-similar wall-jet model[104].

These approximate models enable the simulation of DBD actuation with complex flow field, but at the cost of omitting detailed plasma physics. Specifically, the consideration of parametric influences on actuator performance is unavailable or significantly simplified. As a result, it is difficult to incorporate the characterization of actuation performance with the control system design.

Since surrogate modeling provides an approximation of the objectives as a function of design variables, it can be used to represent the quasi-steady body-force of DBD actuator and to associate DBD parameters with induced flow dynamics.

2.6.1 Quasi-steady body-force field

The time-averaged body-force fields calculated with 2-species fluid plasma model are shown in Figure 2.24, where *x*- and *y*-axes denote 2-dimensional coordinates as in Figure 2.4, and *z*-axis is force magnitude. The contour surfaces of *x*- and *y*-directional forces show nonlinear variations concentrated near the exposed electrode ($0.009 \leq x \leq 0.011$) and the dielectric surface. In addition, the *y*-directional force is dominantly negative, as opposed to $F_{x,T}$.

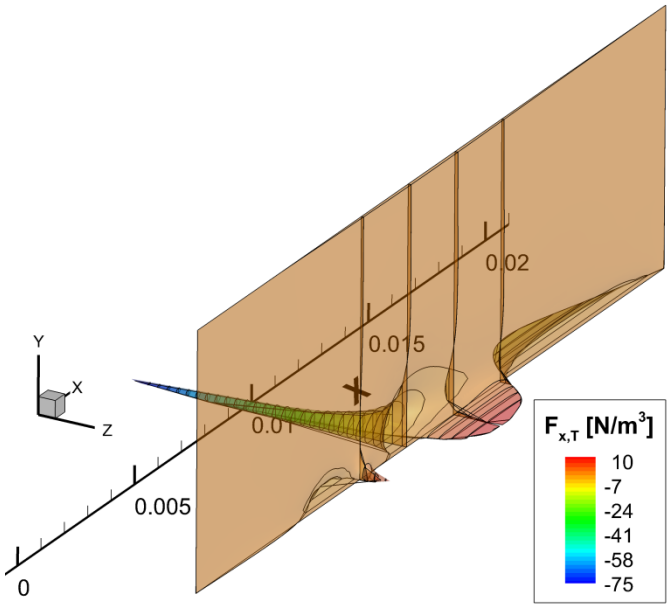

(a) $F_{x,T}$

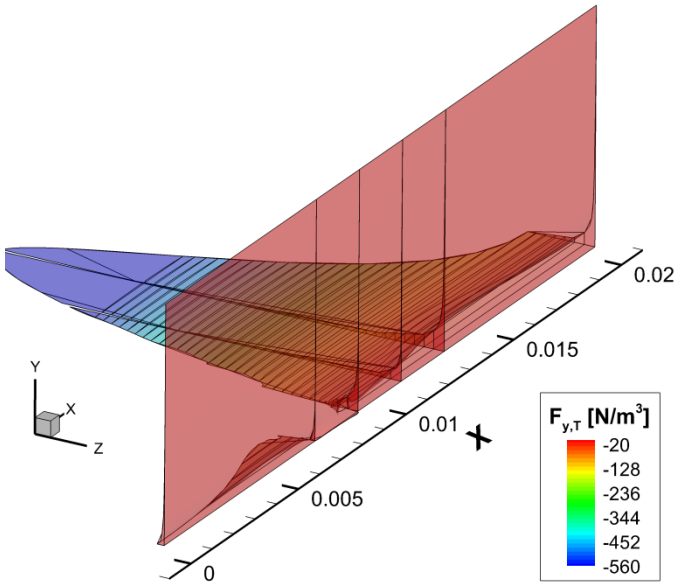

(b) $F_{y,T}$

Figure 2.24 3D surface contours of time-averaged body-force field using 2-species fluid plasma model; $\varepsilon_d = 2$, $f_v = 12.5$ kHz, $r_f = 1$, $V_{app} = 3$ kV.

2.6.2 Surrogate-based approximate body-force model

In order to train surrogate models, the spatial coordinates of the body-fore fields and each force component are assigned as design variables and the objective, respectively. Figure 2.25 compares the original $F_{x,T}$ distribution based on 595 design points and its approximations using three different surrogate models. Due to the highly localized force peaks, PRS fails to capture the force distribution. On the other hand, RBNN and KRG approximate the distribution successfully.

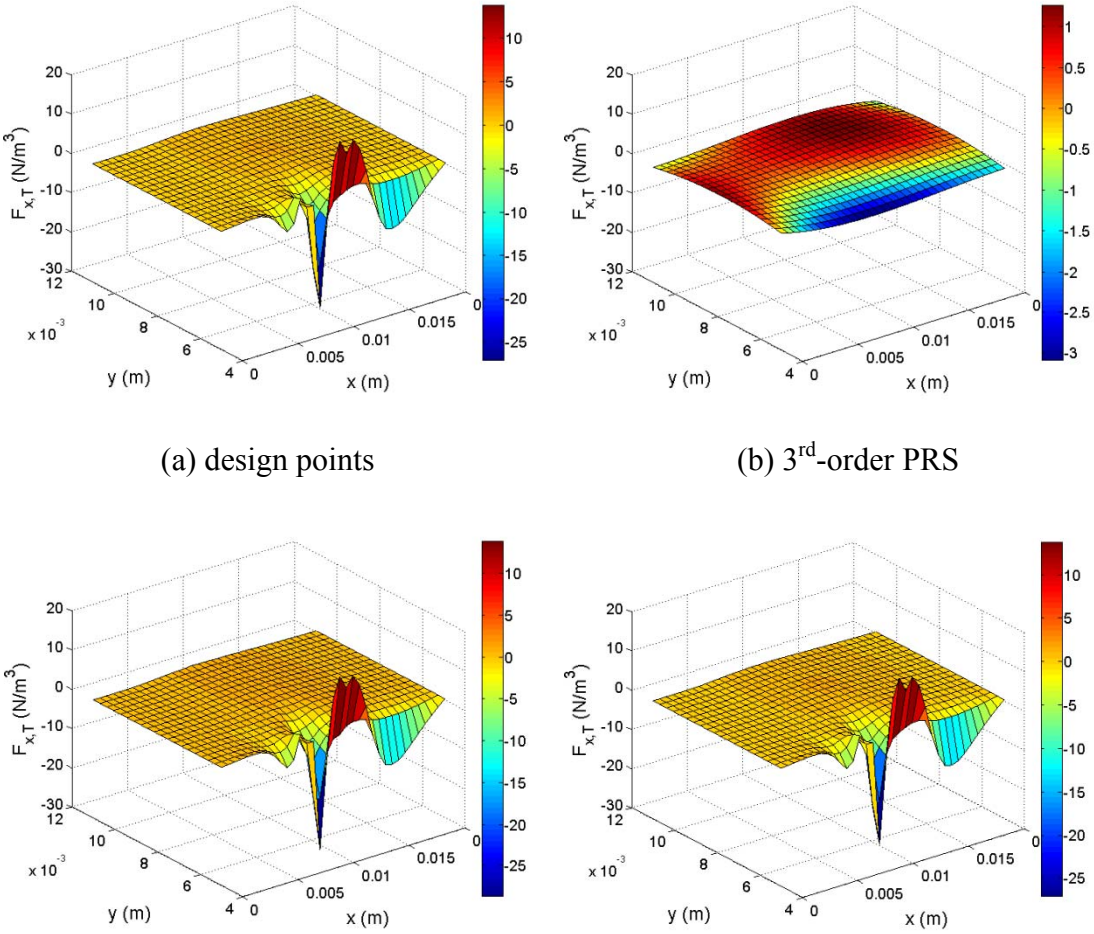

(a) design points (b) 3rd-order PRS

(c) RBNN (d) KRG

Figure 2.25 Spatial distributions of time-averaged *x*-directional body-force and surrogate-based approximations; 595 design points, RBNN (neurons: 595, spread: 0.001), KRG (regression model: 0th-order, correlation model: linear).

2.6.3 Body-force model and induced airflow

Considering the fitting accuracy and convenience in data structure, the force distribution approximated by KRG is chosen for the quasi-steady body-force among the trained surrogate models. For a comparison with experimental results, some actuator parameters are matched, as shown in Table 2.9. However, the geometry and voltage magnitude are not matched due to the computational cost with the fluid plasma model. As previously mentioned, the bilinear body-force model is based on linear spatial-force distribution in both *x*- and *y*-axis directions, and it is chosen as a reference approximate model for comparison. More details of the flow dynamics model and the bilinear model are available in 3.1.1 and 3.1.2, respectively.

Table 2.9 Actuator parameters for velocity profile comparisons.

Study	Exposed electrode	Insulated electrode	Insulator thickness	Dielectric constant	Applied voltage	Voltage waveform
Jacob *et al*. (2005)[105]	10 mm	10 mm	0.05 mm	Kapton	5 kV	4.5 kHz square wave
Hale *et al*. (2010)[106]	5 mm	50 mm	0.054 mm	Kapton	12 kV_{p-p}	10 kHz sinusoid
KRG model*	2 mm	2 mm	5 mm	4.5	6 kV_{p-p}	10 kHz sinusoid
Bilinear model*	The bilinear electric field covers electrodes of the KRG model		5 mm	-	6 kV_{p-p}	-

*: The body-force field is scaled by 50 times to generate the induced velocity comparable to experiments.

The velocity profiles of induced flow are compared in Figure 2.26 at different sections along the streamwise direction, i.e., 0, 5, 10 and 30 mm from the downstream edge of the exposed electrode. The velocity profiles in the vicinity of the exposed electrode are complex and not consistent between two experiments. Likewise, the bilinear and KRG body-force models have difficulties in predicting the velocity near the electrode, and show reasonable comparisons as *x* increases. Although the actuator parameters of the

surrogate-based body-force model match better with Hale *et al*. (2010), the comparison is more consistent with Jacob *et al*. (2005).

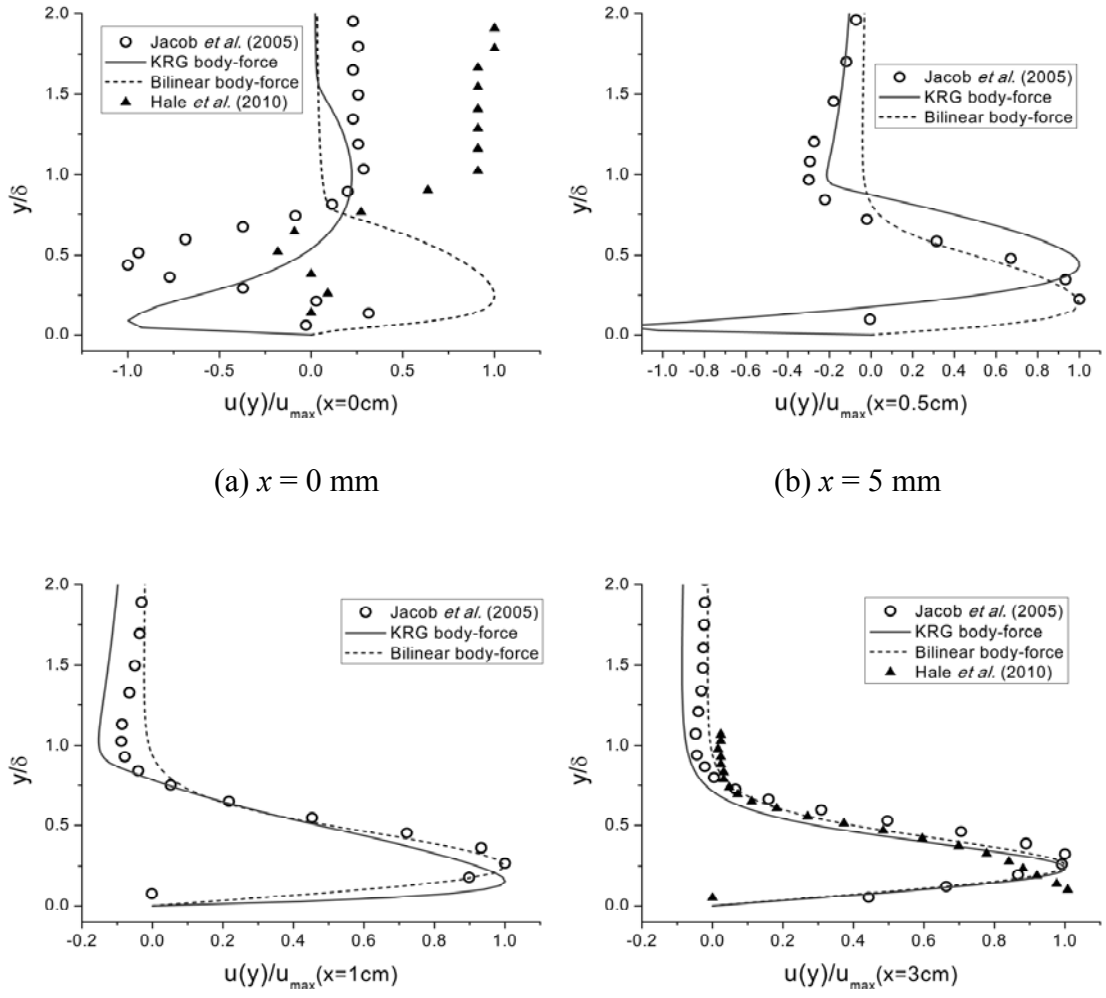

(a) x = 0 mm (b) x = 5 mm

(c) x = 10 mm (d) x = 30 mm

Figure 2.26 Sectional velocity profile comparison; *x* is the distance from the downstream exposed-electrode tip.

The bilinear model performs better in the positive velocity part. Whereas, the KRG model shows the negative velocity region in the vicinity of the exposed electrode, which is shown in Jacob *et al*. (2005) but absent in the bilinear model. Moreover, compared to the bilinear model, the KRG model shows profiles with a higher-shear layer near the wall due to the body-force concentrated near the dielectric surface.

2.7 Summary of the chapter

The parametric effects of the DBD actuator in helium are analyzed by simulating a 2-species fluid model with the help of surrogate modeling techniques. For different levels of refinement and different regions in design space, different surrogates offer the most accurate approximation, which justifies the application of multiple surrogate models. It is found that there are multiple branches of the Pareto front in low and high power regions where parametric impacts and performance variables differ significantly. The degree of correlation and global sensitivity of design variables are very different in the low and high power regions. Average force and power show distinct variation in magnitude and/or direction. Surrogate models combined with detailed solution analysis help us understand various parametric dependencies, as summarized below.

Dielectric constant

The dielectric constant affects the amount of charged particle clouds above the insulator wall during the second half cycle. With a smaller constant, particle clouds thicken, increasing the asymmetry between the two half cycles. As a result, the average force, F_x increases. On the other hand, the dielectric constant also affects the density of the charged particle layer on the insulator surface. With a larger constant, a higher electric field is produced, resulting in an increase of F_x magnitude, but in a negative direction. The amount of overall charged particle generation is also affected by the dielectric constant. With a larger dielectric constant, higher electric field and power consumption occur.

Frequency of applied voltage

The applied voltage frequency affects the amount of overall charged particle generation. With a higher frequency, the discharge duration decreases, and the asymmetry between the two half cycles decreases, resulting in larger F_x in a negative direction. A higher frequency accompanied by a higher dielectric constant induces larger power usage.

Positive-to-negative half cycle time ratio

This ratio also contributes to the overall charged particle generation. With a larger ratio, the first half cycle discharge becomes more prominent. As a result, F_x increases. On the

other hand, the amount of charged particle clouds above the insulator wall during the second half cycle is also influenced. The larger ratio induces a lower level of charged particle generation, which means an insufficient electric field for the plateau region in the second half cycle. As a result F_x decreases.

KRG and RBNN models can successfully provide approximate body-force fields for a single design point. Despite the limitations on geometry and operational voltage in the 2-species fluid plasma model, the surrogate-based body-force combined with airflow simulation results in a reasonable agreement in normalized velocity profile with experiments. The bilinear model performs slightly better in the region with the positive velocity. However, due to its simplicity, the model doesn't allow a reverse flow structure to develop, which is more comprehensive surrogate model can handle more satisfactorily. Overall, both approaches are fast and can be useful to facilitate the development of flow control algorithms.

CHAPTER 3
FEEDBACK FLOW CONTROL USING MARKOV PARAMETERS

In this chapter, the flow around the finite and infinite wings with the SD 7003 airfoil geometry and the DBD actuator installed on their upper surfaces are chosen as the flow-actuator system. Although application of the DBD actuator is suitable for higher Reynolds numbers, usually larger than 10^4, Reynolds numbers in the range of 300 ~ 1000 are chosen in this study to facilitate the development of an effective flow control framework. For Re = 1000, considering the body-force magnitude of a typical DBD actuation, the physical wing chord and free-stream speed correspond to $O(1)$ cm and $O(1)$ m/s, respectively. Under high-angle-of-attack flow fields accompanying massive flow separation, the aerodynamic lift and drag of the wing are chosen as performance measures of the flow-actuator system, and the control goal is to stabilize the performance under unsteady aerodynamics.

3.1 Open-loop control of low-Reynolds number flow

3.1.1 Flow dynamics model

The flow fields are analyzed by solving the incompressible Navier-Stokes equations using Loci-STREAM[107], a parallized pressure-based unstructured finite volume code. Since the ion and electron states in the actuation region are non-equilibrium, and the ion temperature is comparable to the neutral fluid, the neutral fluid is treated as being isothermal. Considering the time scale disparity between the low-Reynolds number flow physics and the gas discharge dynamics of radio frequency (RF), the force acting on the

neutral fluid is assumed to be a quasi-steady body force. The body force felt by the neutral fluid is equivalent to the Lorentz force or Coulomb force (since there is no magnetic field) acting on the net charge density. For the unsteady operation of the actuator, based on the time-scale-difference argument, only voltage variation with time scales much larger than the RF operation is considered.

In index notation, the relevant conservations are, for $i, j = 1, 2, 3$,

$$\frac{\partial u_j}{\partial x_j} = 0, \tag{3.1}$$

$$\frac{\partial u_i}{\partial t} + \frac{\partial \left(u_i u_j\right)}{\partial x_j} = \frac{F_{bi}}{\rho} - \frac{1}{\rho}\frac{\partial p}{\partial x_i} + \nu \frac{\partial}{\partial x_j}\left(\frac{\partial u_i}{\partial x_j}\right), \tag{3.2}$$

where F_{bi} is the DBD body-force vector defined in the next section. Here, x_i is Cartesian position in the global coordinate system, u_i is the flow velocity, ρ is the density, p is the pressure, and v is the kinematic viscosity of air.

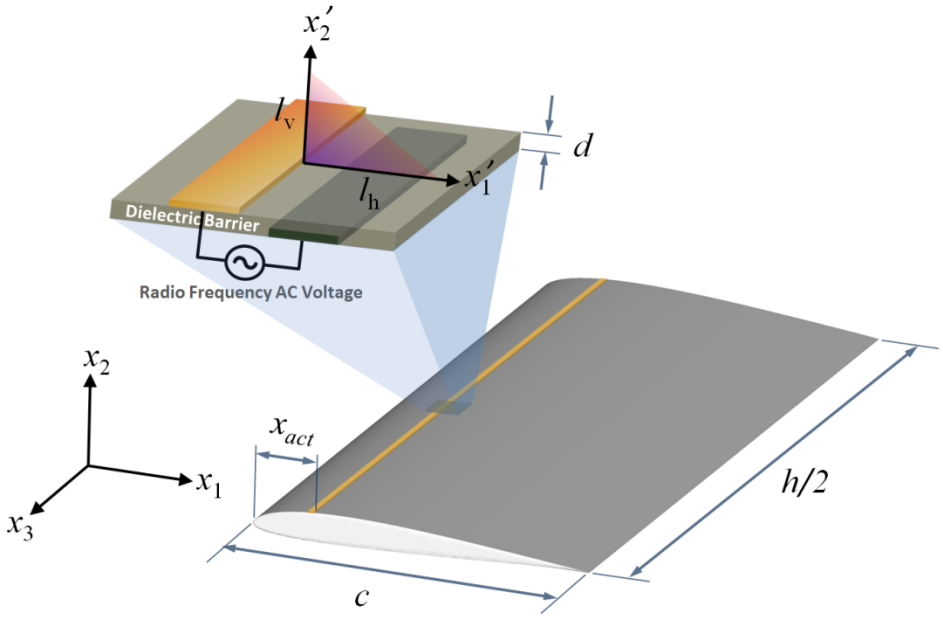

Figure 3.1 Schematics of DBD actuator model.

3.1.2 DBD actuator model

A simplified model representation with a bilinear electric field proposed by Shyy *et al*. (2002)[37] is used in this study to approximate the force field generated by discharge. This approach, which couples the neutral flow field with the reduced-order model via body force, shows good agreement with experimental results[108]. The reduced order model has been applied to studies of flow control in airfoils at low Reynolds numbers[28, 29], low-pressure turbines[109] and bluff-body flows[31], resulting in separation elimination or delay, or significant drag reduction.

The DBD actuator is modeled with the bilinear electric field and constant net charge density[37]. As shown in Figure 3.1, this model prescribes the localized body-force distribution confined in a triangular plasma region, which is bounded by the exposed electrode and dielectric surface. The electric field distribution inside the plasma region is approximated by the spatially bilinear relation

$$\mathbf{E}'\left(x_1',x_2',t\right)=\left(\frac{\left|\mathbf{E}'\left(x_1',x_2',t\right)\right|k_2}{\sqrt{k_1^2+k_2^2}},\frac{\left|\mathbf{E}'\left(x_1',x_2',t\right)\right|k_1}{\sqrt{k_1^2+k_2^2}},0\right), \tag{3.3}$$

$$\left|\mathbf{E}'\left(x_1',x_2',t\right)\right|=E_0\left(t\right)-k_1x_1'-k_2x_2',\quad E_0\left(t\right)=\frac{V_{app}\left(t\right)}{d}, \tag{3.4}$$

where (x_1',x_2') is the actuator local coordinate system, d is the insulator thickness, and k_1 and k_2 are the electric-field slopes in the x_1' and x_2' directions, respectively. This is a solution of Gauss' equation with the assumption that the charge density is constant in the plasma region. In Eq. (3.4), the maximum electric field intensity $E_0\left(t\right)$ is defined using the applied voltage V_{app} and insulator thickness d. The electric-field slopes, which are set to allow breakdown voltage at the plasma boundary with the minimum electric field strength, indicate electric field attenuation away from the exposed electrode and insulator surface. This analytical-empirical model results in the body force acting on the neutral fluid give by

$$\mathbf{F}_b\left(x_1, x_2, t\right) = \rho_c q_c \delta\left(x_1, x_2\right) f_v \Delta t_d \mathbf{E}\left(x_1, x_2, t\right), \tag{3.5}$$

where f_v is the frequency of the AC voltage applied to the DBD actuator, Δt_d is the discharge duty cycle, and $\mathbf{E}\left(x_1, x_2, t\right)$ is the electric field distribution in Eq. (3.3) transformed to the global coordinate system. Since the constant charge density ρ_c with unit charge q_c is present only inside the plasma region, $\delta\left(x_1, x_2\right)$ is set to 1 inside and 0 outside of the region. The actuation is assumed to be 2-dimensional within the wing span, and there is no variation in the actuator parameters along the x_3-axis on the wing. For this study, the horizontal electric field length l_h and vertical length l_v are $0.05c$ and $0.025c$, respectively. The discharge duty cycle is the portion of time during which effective force generation occurs per operation cycle. The applied voltage depends on the control signal, resulting in a time-varying body force. Since the reduced-order DBD model Eqs. (3.3)-(3.5) is based on the quasi-steady assumption, the control input is meaningful only when its timescale lies between those of low-Reynolds-number flow and plasma operation. The DBD model has been validated against experimental data of force generation[110] and maximum induced flow velocity[108].

3.1.3 Flow and actuation conditions

As shown in Figure 3.1, a single DBD actuator covering the wing span is located on the upper surface of the wing at x_{act} from the leading edge. The parametric study to assess the impact on control performance is done for the Reynolds number based on the chord length *Re*, wing aspect ratio *AR*, actuation position x_{act}/c and nominal actuation voltage $V_{app,0}$. When the Reynolds number is changed, the ratio of the free-stream inertial force and DBD body force is maintained constant.

The identification of system parameters for the nominal actuation voltage is done without any disturbance. For the feedback control cases, the disturbance is simplified as a harmonic fluctuation in the vertical free-stream speed as explained in the following section.

3.1.4 Impact of DBD actuation on flow field

a. DBD actuation and high angle of attack low-Reynolds number flow

In this study, an Angle of Attack (*AoA*) of 15˚ is used to explore the dynamics of unsteady flow separation without actuation. An example flow structure around an infinite wing with *Re* = 1000, based on the free-stream speed $U_\infty = \sqrt{U_1^2 + U_2^2 + U_3^2}$, where $\left(U_1, U_2, U_3\right)$ is free-stream velocity, is shown in Figure 3.2. Without any disturbance in the free-stream flow, the separated flow is unstable and induces unsteadiness in the flow field. Specifically, the vortex structure evolves with a non-dimensional period of 1.61; the compact vortex pair causing maximum lift evolves to a single weak vortex generating minimum lift.

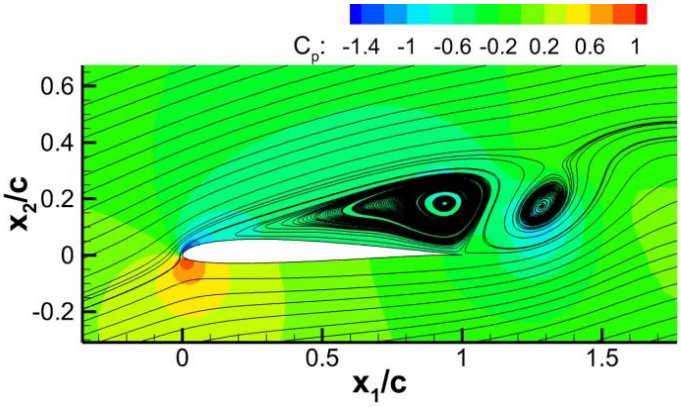

(a) instant of maximum lift

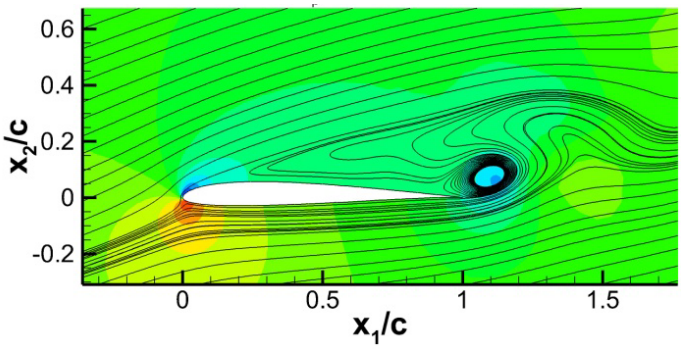

(b) instant of minimum lift

Figure 3.2 Streamlines and pressure contours without actuation (*Re* = 1000, *AoA* = 15°).

If there is a disturbance in the free-stream flow, for example in the vertical flow speed, the vortex instability in the separated flow region is coupled with the free-stream unsteadiness.

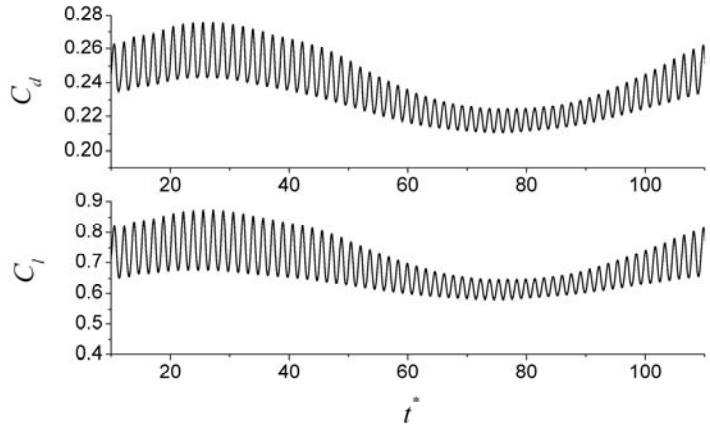

(a)T^* = 100, α_d = 0.1

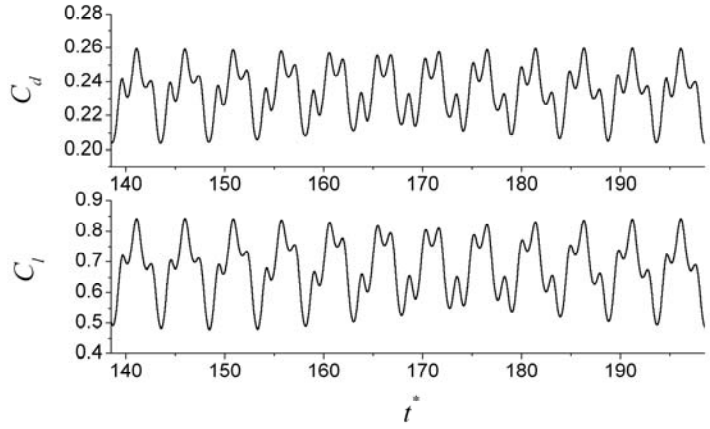

(b)T^* = 5, α_d = 0.06

Figure 3.3 Drag and lift time-histories with the sinusoidal disturbance in vertical free-stream speed (*Re* = 1000, *AoA* = 15°).

In this study, the free-stream velocity is $\mathbf{U}\left(t^*\right)=\left(U_1, U_2\left(1+\alpha_d \sin\left(2\pi t^*/T^*\right)\right), U_3\right)$, where $t^* = U_\infty t/c$ is the non-dimensional time, α_d is the disturbance amplitude, and T^* is the non-dimensional disturbance period. As shown in Figure 3.3(a), if the frequency difference between the instability of the separated flow and the free stream unsteadiness is large, the two time scales are separated. However, if the two time scales have the same

order of magnitude, as shown in Figure 3.3(b), two fluctuations are coupled, resulting in larger amplitude variations in drag and lift even with the lower disturbance amplitude.

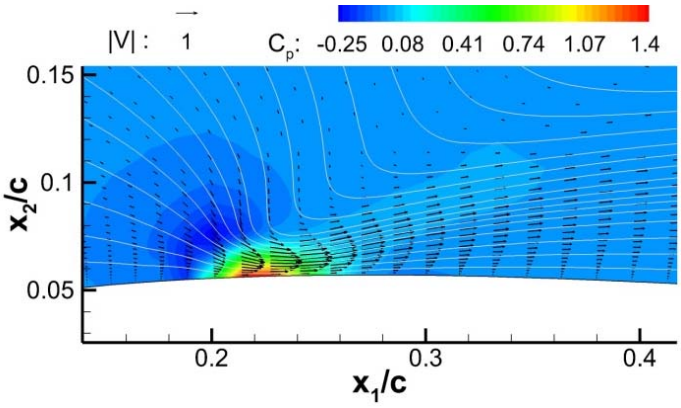

(a) velocity vectors, streamlines and pressure contours without free stream

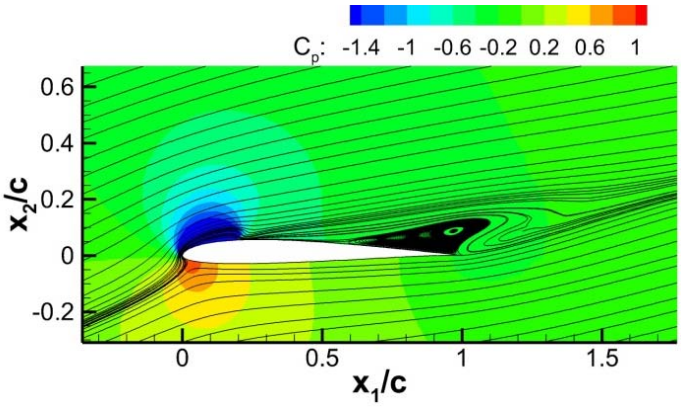

(b) streamlines and pressure contours with free stream

Figure 3.4 Flow field with the actuation of V_{app} = 1 kV (actuator length: l_h/c= 0.05, position: x_{act}/c = 0.2).

When the actuator is activated, the body-force field generates an induced flow near the airfoil surface as shown in Figure 3.4(a). The reduced-order DBD actuator model approximates the body-force field inside the ionized gas volume with quasi-steady linear distributions of positive x_1-directional and negative x_2-directional forces. The actuation V_{app} = 1 kV induces a maximum flow speed comparable to the free-stream speed U_∞. For V_{app} = 1 kV, the maximum non-dimensional body force, normalized by the inertial force of the free stream condition, is approximately 97.2. While inducing the flow entrained from the surrounding air and accelerated downstream, the actuator generates suction and

pressure regions upstream and downstream of the actuation position, respectively. As a result of the induced wall jet, the additional wall shear stress contributes to the drag increase. When this wall-jet is applied to the flow with $\alpha = 15^{\circ}$, the separated flow region decreases, and the unsteady separated region is stabilized with a reduced separated-flow region as shown in Figure 3.4(b).

b. Actuation voltage

In Figure 3.5, the flow structure, streamlines at the symmetry plane and pressure distribution of the flow fields with different actuation voltages between 1 ~ 6 kV are compared for Re = 300 and 1000. Although the angle of attack is high as 15°, the flow with the wing aspect ratio of 8 is mostly 2-dimensional except the wing tip. Without actuation, the flows over the airfoil are entirely separated at both Reynolds numbers with a recirculation region surrounded by shear layers. Compared to Re = 300, the separated flow region at Re = 1000 is larger with thinner shear layers, and suction peaks in the sectional pressure distribution are more localized near the leading edge.

For both Reynolds numbers, when the actuation of V_{app} = 1 kV is applied, the separated flow region is decreased. The sectional pressure coefficient distributions show that the actuation results in a 2-dimensional (little spanwise variation except the wing tip) intensified suction peak near the leading edge and a pressure peak near the actuator. Compared to Re = 300, the enhanced suction peak is more noticeable for Re = 1000, and the velocity deficit in the shear layers decreases more significantly than Re = 300. As V_{app} increases, flow separation is reduced accordingly. No recirculating flow is observed for $V_{app} > 4$ kV.

For Re = 300, though the flow separation can be suppressed, the velocity deficit downstream of the wing hardly decreases for $V_{app} > 1$ kV, and the negative pressure on the upper surface of the wing cannot be recovered near the trailing edge. As voltage increases, although the suction pressure near the leading edge increases and contributes to enhancing lift, the pressure peak near the actuator is intensified at a higher rate, contributing unfavorably to lift.

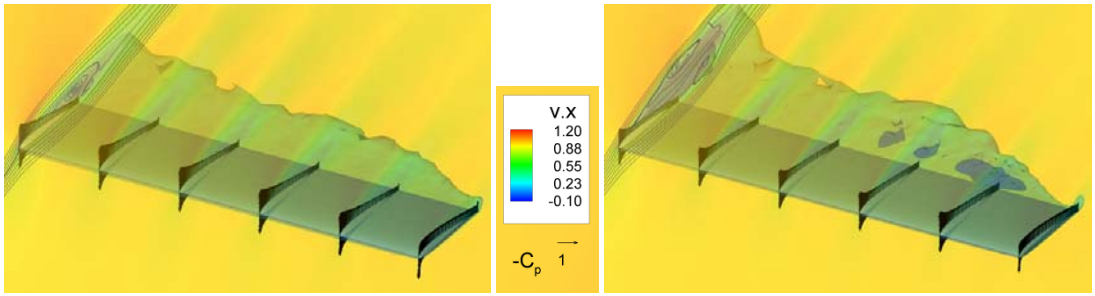

(a) no actuation

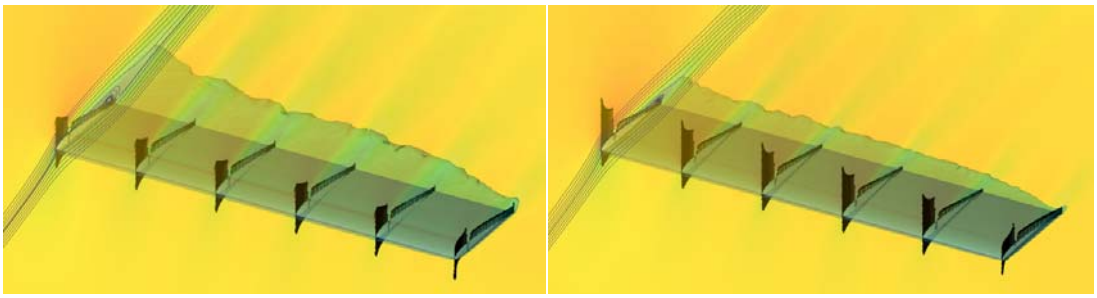

(b) V_{app} = 1 kV

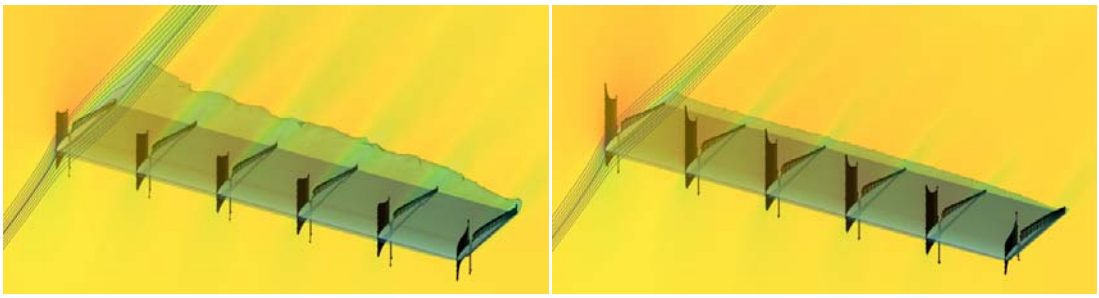

(c) V_{app} = 4 kV

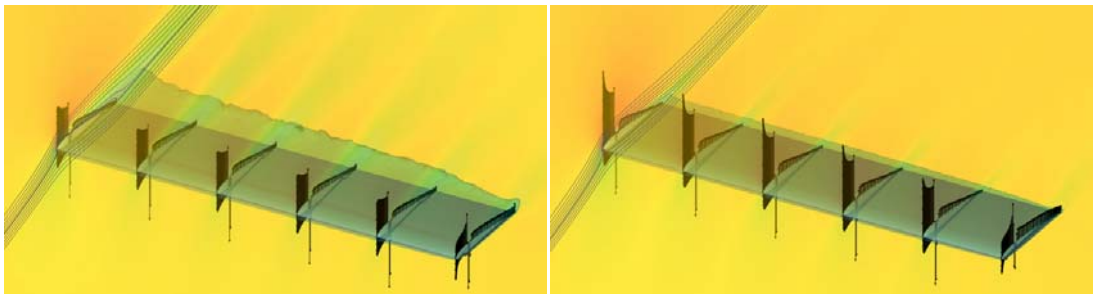

(d) V_{app} = 6 kV

Figure 3.5 Streamlines on the symmetry plane, V_x contours and pressure distribution at 6 wing sections, and iso-velocity-magnitude surface of $|V| = 0.3$; left column: $Re = 300$, right column: $Re = 1000$ ($AR = 8$, $AoA = 15°$, $x_{act} = 0.2c$).

On the other hand, for Re = 1000, the increase of the suction pressure, especially near the leading edge, is more prominent, which is an indication of lift enhancement and drag decrease. The velocity deficit in the shear layers is reduced continuously as the voltage increases up to 6 kV, and the pressure recovery at the trailing edge is facilitated, implying a reduction in pressure drag.

In Figure 3.6, the aerodynamic lift and drag as functions of the applied voltage are shown. The lift and drag coefficients, C_L and C_D, are based on the total surface forces acting on the wing, whereas the pressure lift and drag coefficients, $C_{L,p}$ and $C_{D,p}$, only reflect the pressure forces on the wing. In Figure 3.6(a) the total drag increases with the voltage increase, whereas the pressure drag decreases. The former can be explained by considering that the viscous forces due to the induced jet overcome the impact of pressure forces at low Reynolds numbers. The latter is because the suction region near the leading edge intensified by the actuation decreases the pressure drag. For lift, on the other hand, the difference between the total lift and pressure lift is much less than drag, as shown in Figure 3.6(b). Moreover, compared to the monotonic increase of lift with actuation at Re = 1000, the dependency of lift on actuation voltage is not monotonic at Re = 300. As discussed in previous studies, the voltage-lift relation is dependent on aspect ratio and actuation location, as well as Reynolds number.

The voltage range in Figure 3.6 can be divided in two according to the slope of the voltage-performance relation. For up to $V_{app} \approx 1$ kV, the actuation is more influential in aerodynamic forces than higher voltages. The higher sensitivity to voltage can be attributed to the existence of the separated flow region at lower voltages. At higher voltages, once the flow is almost attached, only the intensified suction region and pressure peak induced by the actuator dominate the resultant aerodynamic forces. The drag increase rate with voltage is sustained as the voltage increases, and the slope is insensitive to the Reynolds number. On the other hand, the lift increase rate is reduced, which is thought to be caused by the pressure peak that counteracts the favorable contribution of the upstream intensified suction region to lift.

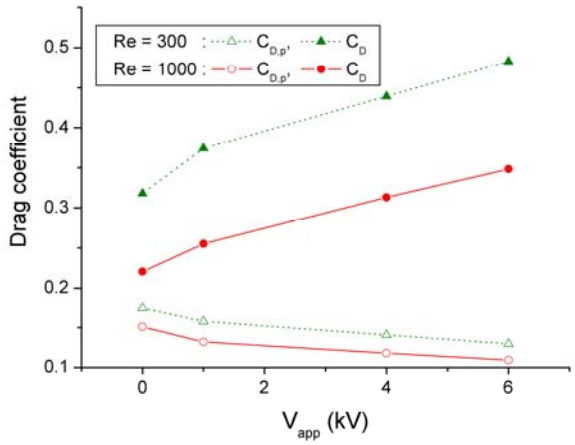

(a) pressure and total drag coefficients

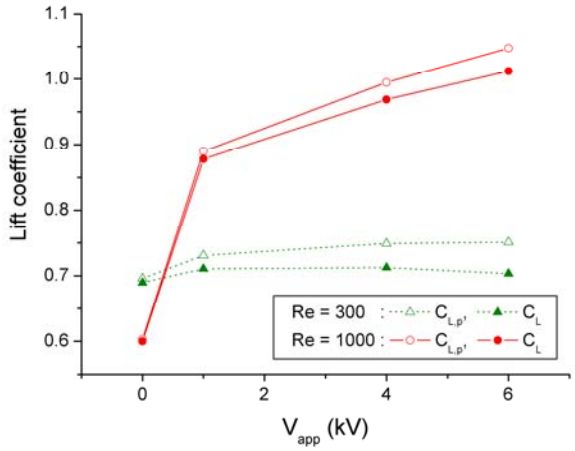

(b) pressure and total lift coefficients

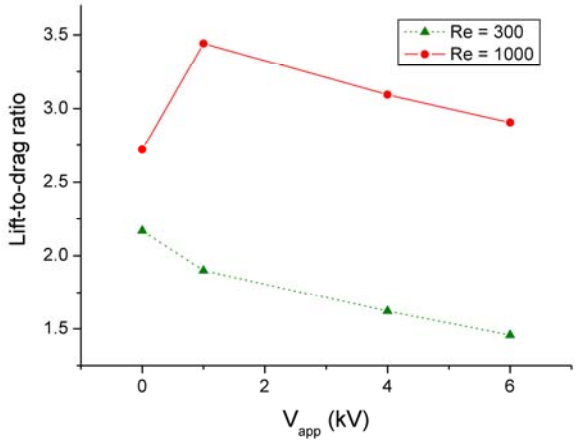

(c) lift-to-drag ratio (C_L/C_D)

Figure 3.6 Applied voltage and aerodynamic forces (AR = 8, x_{act}/c = 0.2).

The relation between the applied voltage and lift-to-drag ratio is shown in Figure 3.6(c). At Re = 300, since the actuation deteriorates both lift and drag, the lift-to-drag ratio becomes lower as the voltage increases. At Re = 1000, on the other hand, the lift-to-drag ratio increases with voltage for V_{app} < 1 kV. This non-monotonic relation is caused by the steep increase of lift at lower voltages. Due to the lift increase even for higher voltages, the lift-to-drag ratio can be enhanced by actuation compared to the case without actuation, although the lift-to-drag ratio starts to decrease for V_{app} > 1 kV.

c. Impact of wing aspect ratio

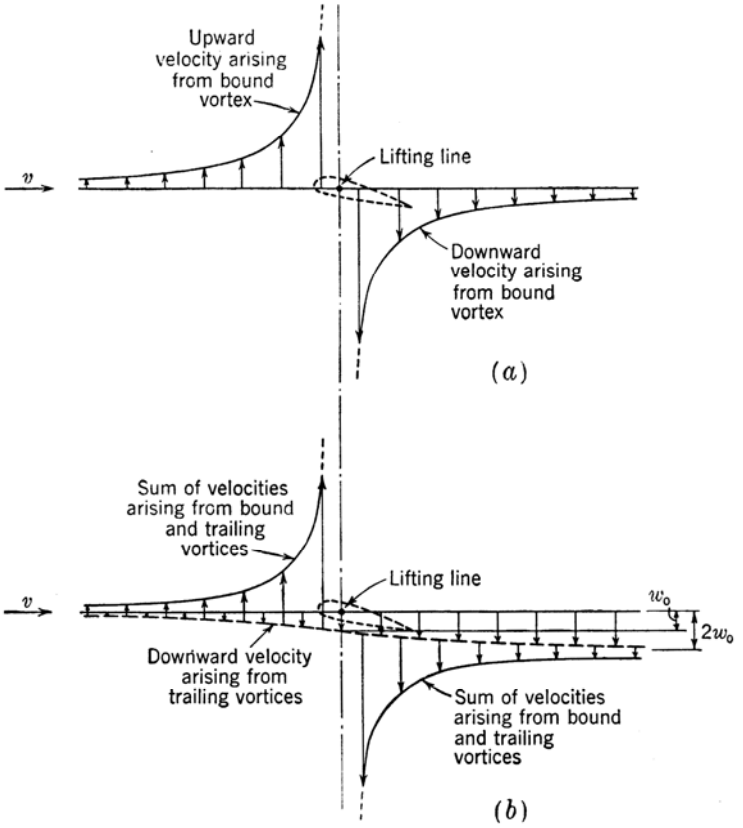

Figure 3.7 Streamwise vertical-velocity distributions for (a) infinite wing and (b) finite wing (reproduced from Pope, 1951[111]).

The major 3D flow effect on a finite wing is the impact of wing tip vortices, which are absent in 2D flows. The influence of 3-dimensionality increases as the angle-of-attack increases and wing aspect ratio decreases. As shown in Figure 3.7, where vortex theory illustrates the streamwise variation of the flow velocity normal to the free stream due to

the wing-bound vortex, the downwash flow of a finite wing decreases the upward upstream flow and increases the downward downstream flow. As a result, the downwash flow induced by wingtip vortices decreases the effective angle of attack, resulting in lower lift and higher drag compared to 2D cases. According to vortex theory, the vertical velocity increases to plus and minus infinities upstream and downstream of the lifting line, respectively, and the impact of downwash on the vertical flow velocity converges to its maximum as the flow goes downstream.

With the DBD actuation at the angle-of-attack of 15°, the vertical (x_2-directional) flow velocity variation along the streamwise direction is shown in Figure 3.8. All cases with different voltage and aspect ratios consistently show upward upstream and downward downstream flows similar to Figure 3.7, except near the leading and trailing edges of the wing where the actual flow speed should be zero and far downstream where the wing tip vortices dissipate. In addition, Figure 3.8(a) shows that the impact of wing tip vortices, similar to Figure 3.7, exists with the moderate actuation. With the higher actuation voltage of 33 kV as shown in Figure 3.8(b), the maximum upward upstream velocity increases by 80 % for the 2D case. For the 3D case, however, the change is lower, especially at the leading and trailing edges. The difference between the 2D and 3D cases implies that the DBD actuation amplifies the influence of 3-dimensionality, which is characterized by the downwash effect for finite wings.

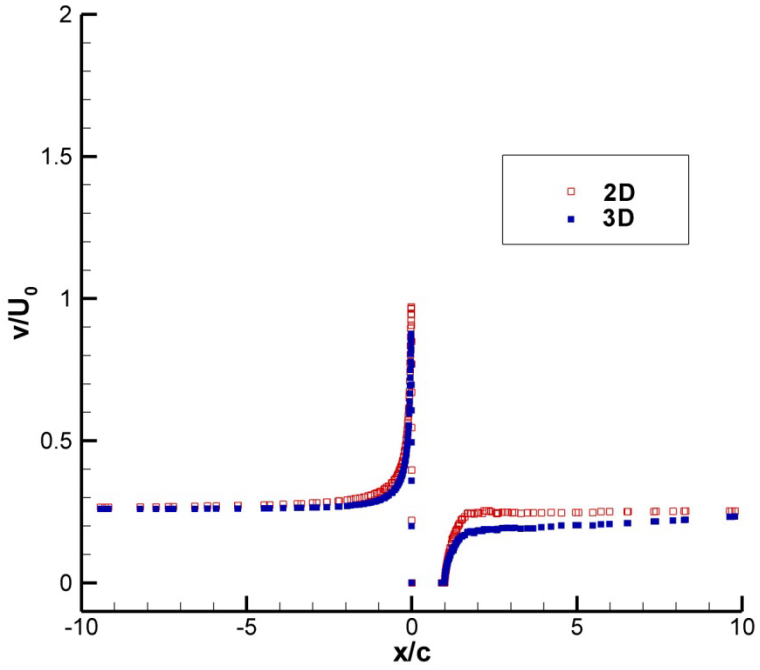

(a) V_{app} = 1 kV

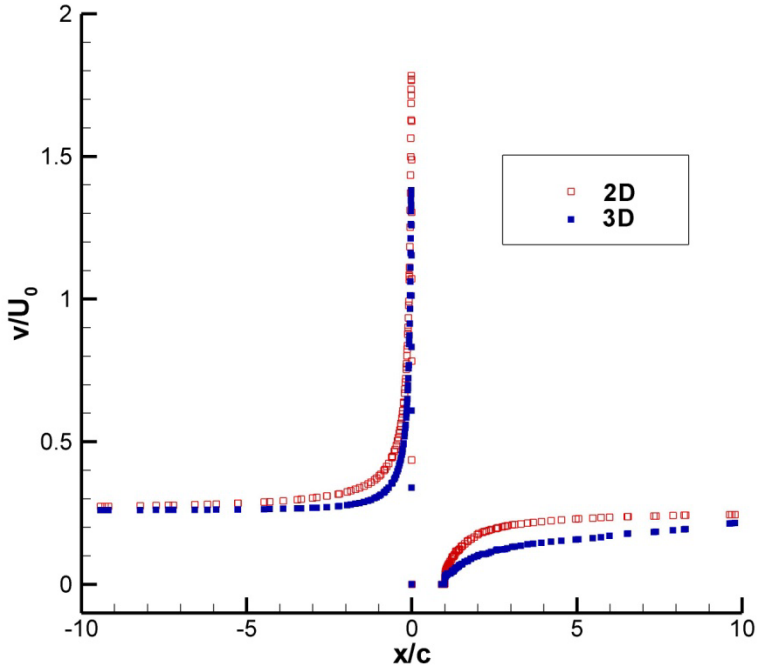

(b) V_{app} = 33 kV

Figure 3.8 *y*-directional velocity distributions along $y = 0$ on the symmetric plane ($AR = 4$, $AoA = 15°$, $Re = 300$, wing chord is located at $0 \leq x/c \leq 1$).

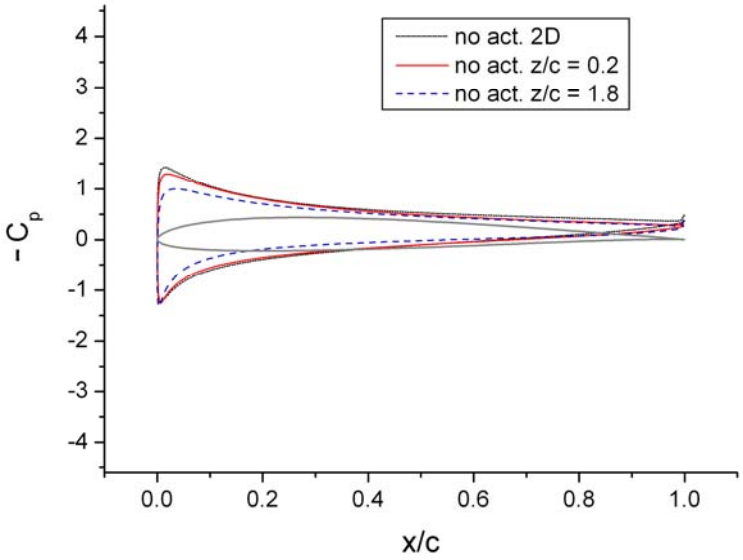

(a) no actuation

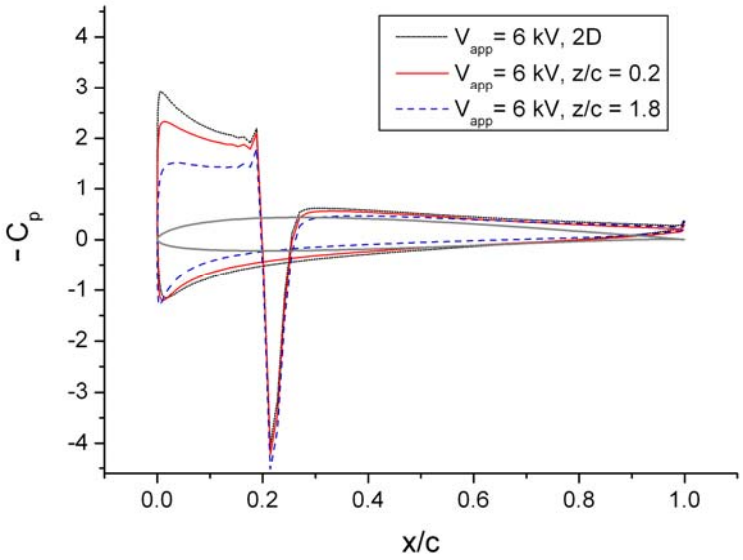

(b) V_{app} = 6 kV

Figure 3.9 Pressure coefficient distributions for 2D and 3D wings (AR = 4 for 3D, *AoA* = 15°, *Re* = 300).

For the same flow conditions, the distributions of pressure coefficients at different sections for 3D are compared with 2D in Figure 3.9. In Figure 3.9(a), since the flow is massively separated without actuation, no suction peak exists near the leading edge and the pressure distributions are flat across the upper surface. The actuation helps to recover the suction pressure as well as induces the pressure peak near the actuator as shown in

Figure 3.9(b). Though the suction pressure near the leading edge is enhanced with actuation for 2D and 3D sections at z/c = 0.2 and z/c = 1.8, the pressure recovery in the suction region diminishes as there exists more 3D flow effect (2D > 3D at z/c = 0.2 > 3D at z/c = 1.8), implying that the 3D effect is increased with actuation. As shown in the previous section, although the flow topology is changed by actuation from separated to attached flow, the pressure distribution downstream of the actuation position is barely changed, which is attributed to the dominant viscous effect at such a low Reynolds number. Since the actuation increases the 3D effect while keeping pressure distributions downstream of the actuator, including the pressure peak, the impact of actuation on aerodynamic forces is expected to be less favorable for finite wings at this Reynolds number.

The impact of wing aspect ratio on the relation between voltage and aerodynamic forces is shown in Figure 3.10, where the left column corresponds to Re = 300 and the right to Re = 1000. At both Reynolds numbers, as the wing aspect ratio increases, the higher lift can be achieved with the lower drag at a given voltage. Moreover, the higher aspect ratio results in the steeper slope of the voltage-lift relations. At Re = 300, while the lift of the infinite wing can be enhanced with the actuation, the actuation voltage higher than 1 kV decreases the lift of the wings with AR = 4 and 8. As a result, the lift-to-drag ratio cannot be enhanced by introducing the actuation at this lower Reynolds number. These unfavorable impacts with finite wings are consistent with the 3D effect with actuation explained above. At Re = 300, as a result, only decreasing pressure drag or increasing pressure lift for $AR \geq 8$ is feasible with the DBD actuation. On the other hand, for Re = 1000 in the right column, the impact of aspect ratio on the voltage-lift slope is more noticeable. Especially for the infinite wing, when the voltage is in the range of $0 < V_{app} \leq$ 1 kV, the impact is significant enough to decrease drag. Since the lift increase at Re = 1000 is more considerable compared to Re = 300, there is a voltage range (0 ~ 1 kV for AR = 4 and 8, and 0 ~ 4 kV for $AR = \infty$) where the life-to-drag ratio can be enhanced by actuation. An additional observation is that, for V_{app} > 1 kV, the slopes of the voltage-pressure drag relations are insensitive to Reynolds number and aspect ratio.

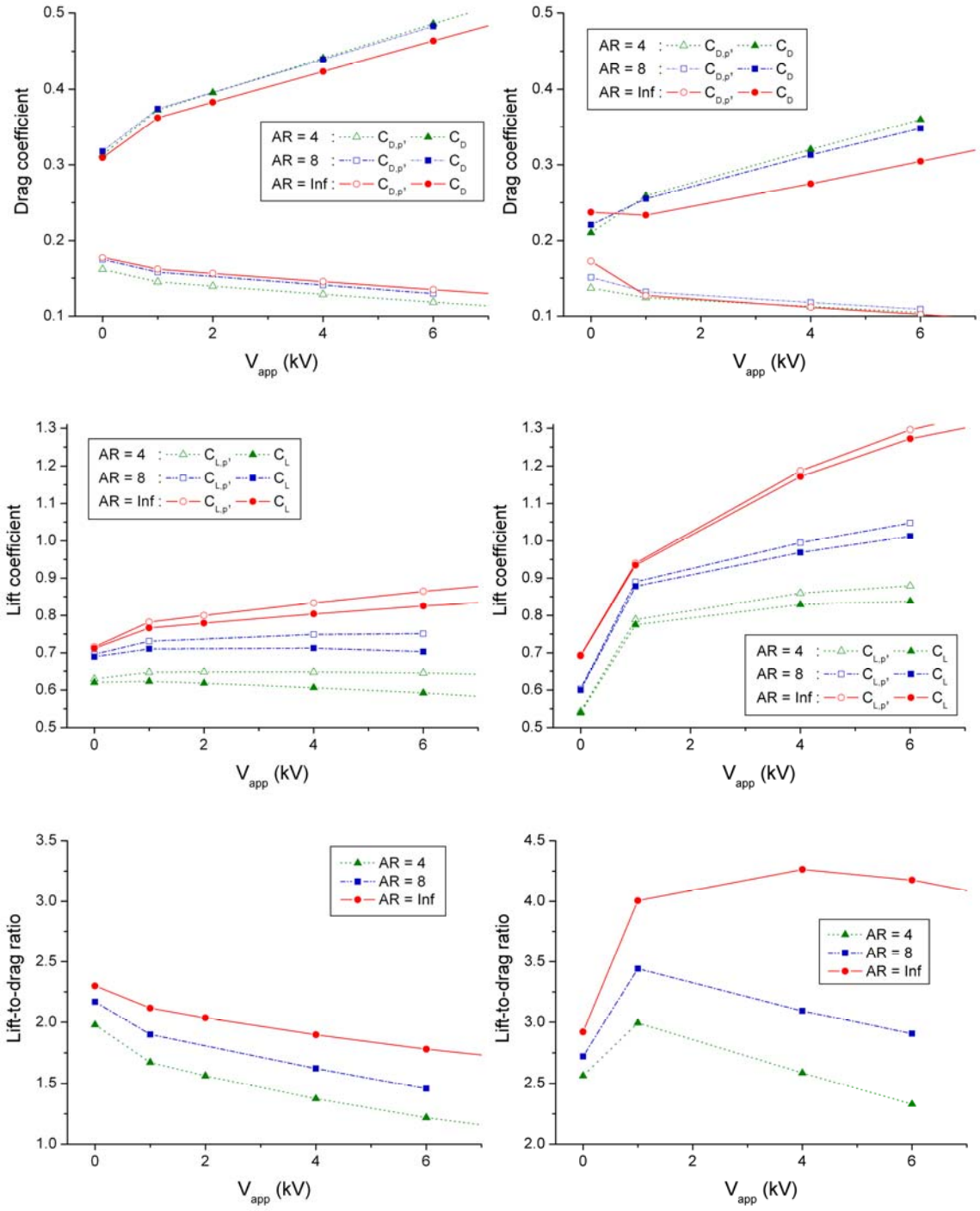

Figure 3.10 Applied voltage and aerodynamic forces with wing aspect ratio; left column: *Re* = 300, right column: *Re* = 1000.

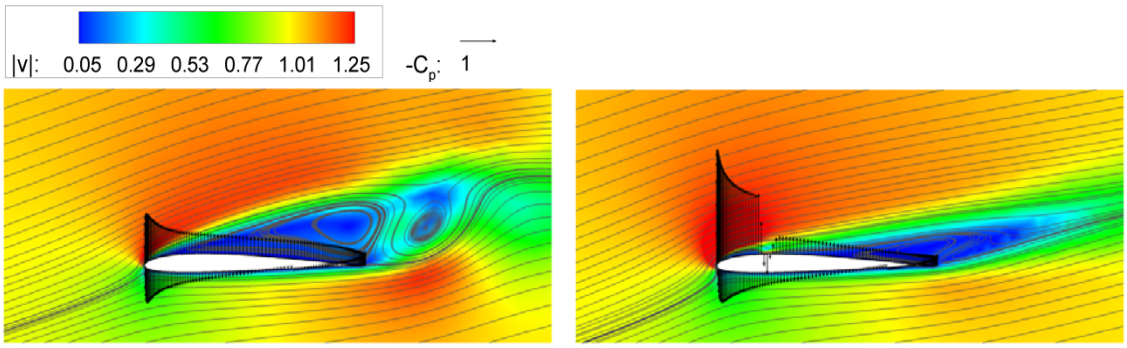

(a) 2D

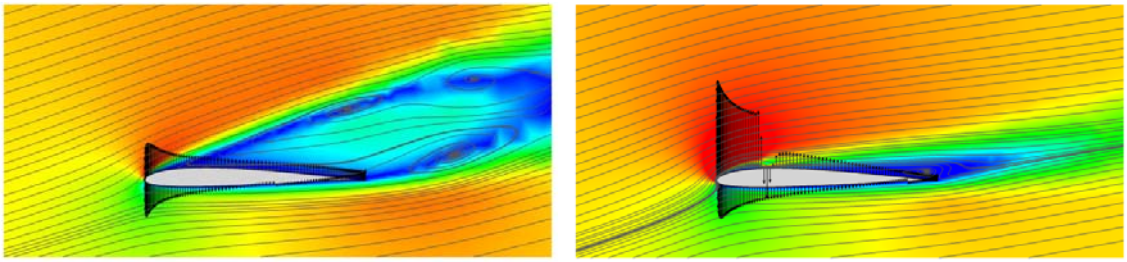

(b) $AR = 4$, $z/c = 0$

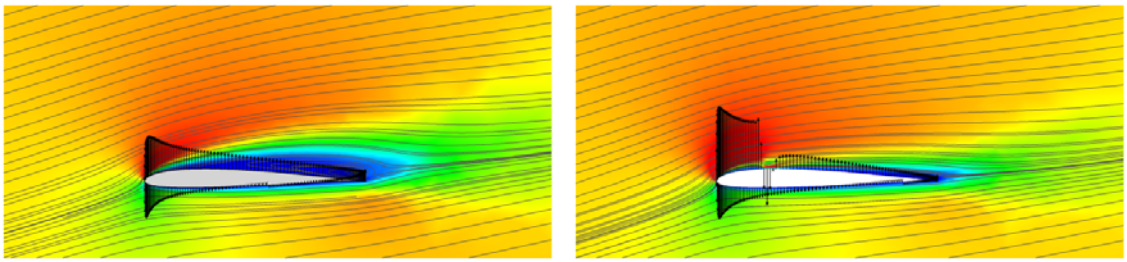

(c) $AR = 4$, $z/c = 1.6$

Figure 3.11 Velocity magnitude contours, streamlines and surface pressure distribution; left column: no actuation, right column: V_{app} = 1 kV (Re = 1000, AoA = 15°, $x_{act} = 0.2c$).

In Figure 3.11, flow fields of the infinite wing and $AR = 4$ are compared to explore the significant change in the voltage-drag relation for $0 < V_{app} \leq 1$ kV, depending on wing aspect ratio. Without actuation, the 2D flow shows a periodic evolution of flow structure, and an instantaneous flow field is shown in Figure 3.11(a). Compared to $AR = 4$ in Figure 3.11(b), which shows the flow at the symmetry plane, the lower pressure inside the separated region near the trailing edge for the 2D case contributes higher drag. For V_{app} = 1 kV, the fore part of the separated flow is attached; the suction peak is intensified, and the pressure peak downstream of the actuator appears. Compared to $AR = 4$ in Figure

3.11(b) and (c), the 2D flow in Figure 3.11(a) shows that the higher increase in the suction peak and lower increase in the pressure peak contribute favorably to drag reduction, though the size of the separated region is larger and the pressure recovery near the trailing edge is less than for $AR = 4$. As mentioned earlier, the impact of actuation on drag is notable for $0 < V_{app} \leq 1$ kV, where the resizing of the separated flow region performs an important role in the force changes. As the voltage increases to $V_{app} \geq 4$ kV, however, the induced wall jet further increases the friction drag whose impact overcomes the benefit of the decreased pressure drag, resulting in the increase of the total drag.

d. Impact of the actuation location

For $Re = 300$, the impact of the actuation location on the voltage-force relations is compared in Figure 3.12 for $x_{act}/c = 0.2$ and 0.7. As the actuation position moves to downstream, the slopes of the voltage-pressure forces – pressure drag $C_{D,p}$ and pressure lift $C_{L,p}$ – are affected significantly. For the airfoil geometry of SD 7003, the surface normal vector at $x_{act}/c = 0.2$ points slightly upstream, and inclines to downstream at $x_{act}/c = 0.7$. The increase of pressure drag with voltage increase for $x_{act}/c = 0.7$ can be explained by considering the direction of pressure forces heading downstream. As pointed out in the previous discussions, among the impacts of the DBD actuation on the aerodynamics forces, namely suppression of flow separation, intensified suction and pressure peaks, the latter two dominate the impact on aerodynamic forces at $Re = 300$. For $x_{act}/c = 0.7$, the enhanced suction pressure near the actuator acts on the surface facing downstream and increases pressure drag for the 2D case. As opposed to $x_{act}/c = 0.2$, it is interesting to observe that the voltage-pressure drag slope depends on aspect ratio at $x_{act}/c = 0.7$. As the wing aspect ratio decreases, the voltage-pressure drag slope becomes negative. The slope of the voltage-pressure lift relation, on the other hand, increases for $x_{act}/c = 0.7$ compared to $x_{act}/c = 0.2$, which means a favorable impact of actuation on lift. The impact is more noticeable for finite wings.

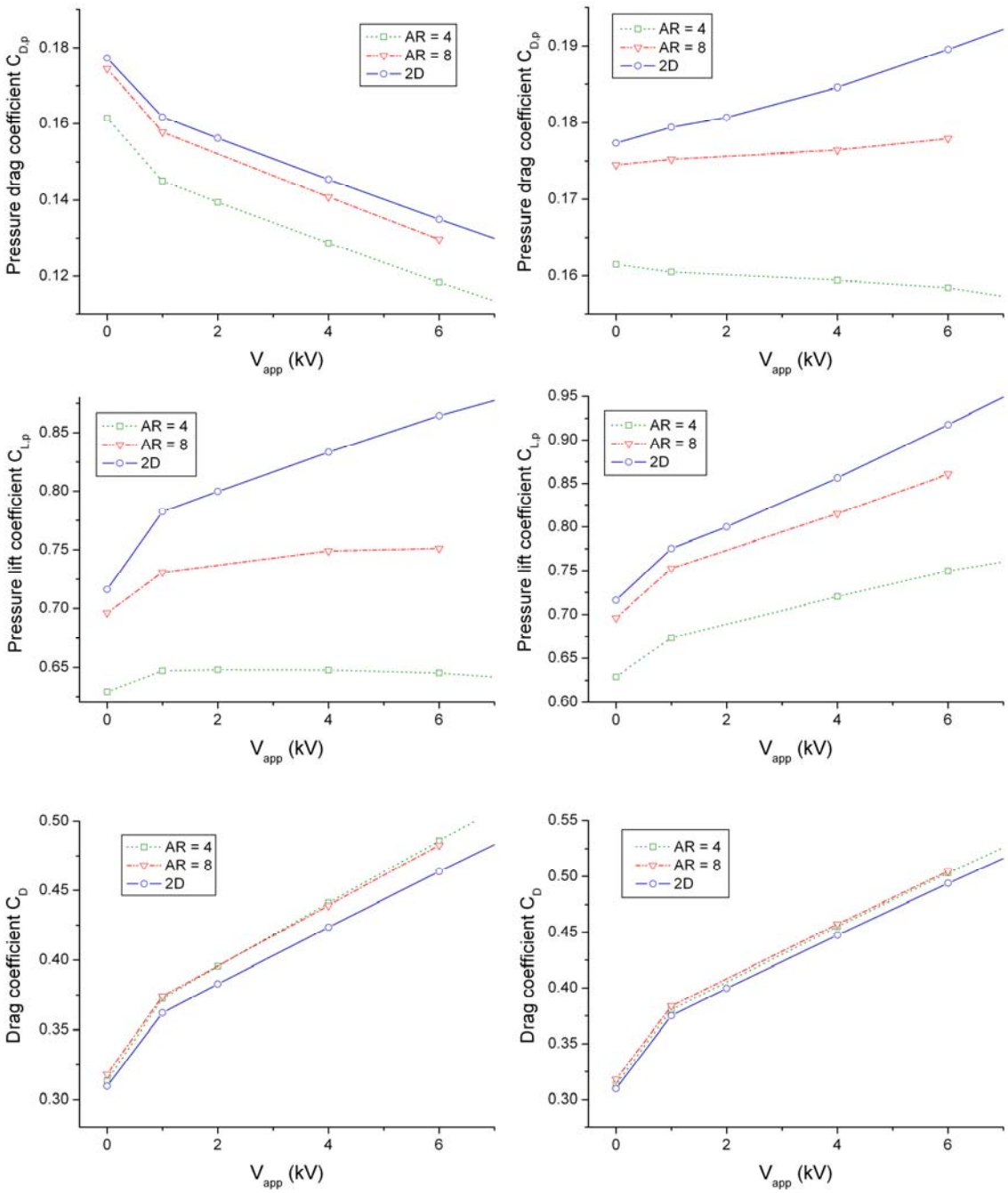

Figure 3.12 Applied voltage and aerodynamic forces with actuation position; left column: x_{act}/c = 0.2, right column: x_{act}/c = 0.7 (Re = 300, AoA = 15°).

To summarize, the actuation location significantly affects control authority regarding pressure drag. On the other hand, the voltage-drag relation, which includes viscous forces, remains without much change according to the actuation location as shown in Figure 3.12.

This insensitivity of drag to voltage, as explained in the previous section, can be attributed to the friction forces dominating drag at $Re = 300$.

3.2 Markov parameter-based system identification

3.2.1 Background

A dynamic system can be represented using a state space model. In discrete-time, a state space model or internal description of a model represents a system with a set of first-order difference equations in terms of the internal state, in addition to the input and output. A finite dimensional, discrete-time, time-invariant, linear system can be expressed as

$$x(k+1) = Ax(k) + Bu(k), \tag{3.6}$$

$$y(k) = Cx(k) + Du(k), \tag{3.7}$$

where $x(k) \in \mathbb{R}^n$ is the state, $u(k) \in \mathbb{R}^{l_u}$ is the control, $y(k) \in \mathbb{R}^{l_y}$ is the measurement for $k \geq 0$.

The matrices *A, B, C* and *D* are maps among control, measurement and state variables, and characterize the system dynamics. For example, the transfer function from *u* to *y* is

$$G(z) = C(zI - A)^{-1} B + D. \tag{3.8}$$

The controllability and observability matrices, V_r and W_s, respectively, can be defined as

$$V_r = \begin{bmatrix} C & CA & \cdots & CA^{r-1} \end{bmatrix}^T, \tag{3.9}$$

$$W_s = \begin{bmatrix} B & AB & \cdots & A^{s-1}B \end{bmatrix}, \tag{3.10}$$

On the other hand, a time-series model, also called an input-output model or external description of a model, relates the input (control) and the output (measurement) only. For

example, common time-series models include the ARMA (autoregressive moving average) model,

$$y(k) = \sum_{i=1}^{n} -M_i y(k-i) + \sum_{i=1}^{n} N_i u(k-i), \tag{3.11}$$

where $M_i \in \mathbb{R}^{l_y \times l_y}$ and $N_i \in \mathbb{R}^{l_y \times l_u}$ are system parameter matrices.

Since the input-output relation can be explicitly measured from experiments, the estimation of an input-output model is usually more convenient than that of a state space model, especially when the analytic description of system dynamics is not available. On the other hand, since the majority of system and control theories are based on the state-space representation, it provides more insight into the system dynamics. Moreover, for higher order systems, estimating the roots of the polynomials in the transfer function based on M_i and N_i in Eq. (3.11) is known to be more subject to numerical ill-conditioning than the calculation of eigenvalues of the system matrix A in Eq. (3.6)[112].

The conversion from the state space model to the input-output model can be done by calculating the output using Eqs. (3.6) and (3.7) with known initial state and control. On the other hand, the conversion from the input-output model to the state space model requires solving a realization problem which involves the construction of state as well as system matrices. Generally, a system has infinite realizations that have the same input-output relation. The dynamic system Eqs. (3.6) and (3.7) is realizable if the system is controllable and observable, i.e., the ranks of matrices V_r and W_s are equal to the order of the system n. Among various realization approaches, the eigensystem realization algorithm (ERA)[113, 114], which is introduced below, is widely used to get a minimum-order realization.

System identification is the process of obtaining the mathematical descriptions of a system from its inputs and outputs. Considering the infinite dimensionality and nonlinearity of real systems, system identification involves conducting model reduction and estimating relevant model parameters rather than obtaining an analytical model of the system. For the convenience of the identification process and further application to

adaptive control, time-series models are more useful for handling input-output data. Some examples are ARMA model in Eq. (3.11), ARMAX model, which includes the process of exogenous noise in ARMA, and nonlinear models such as the Hammerstein-Wiener model.

A linear, time-invariant system can be uniquely determined by introducing Markov parameters as the system parameters. Markov parameters are the impulse response of the system. By assuming the zero initial states, Markov parameters can be defined as

$$H_i = \begin{cases} D & , \ i = 0 \\ CA^{i-1}B & , \ i \geq 1 \end{cases} . \tag{3.12}$$

Since the impulse response of a system can be directly obtained through experimentation, Markov parameters are a powerful tool in system identification as well as a medium relating the input-output and state-space models.

For example, a rational transfer function of Eq. (3.8) can be related to Markov parameters by expanding the transfer function at $z = \infty$, resulting in the Laurent series expansion[115]

$$G(z) = \sum_{i=1}^{\infty} z^{-i} H_i . \tag{3.13}$$

As shown in Santillo and Bernstein (2010)[116], the truncated expansion of Eq. (3.13) includes the Markov-parameter polynomial

$$p_r(z) = H_1 z^{r-1} + \cdots + H_{r-1} z + H_r . \tag{3.14}$$

The Markov-parameter polynomial contains information about the relative degree, which is d when $H_1 = \cdots = H_{d-1} = 0$, and the sign of the high-frequency gain H_d. Moreover, as r increases, the roots of Eq. (3.14) approximates the nonminimum-phase zeros of the transfer function, i.e., the complex numbers with magnitude greater than one where the transfer function equals zero. As explained in 3.3, since this model information is required by the adaptive controller adopted for this study, the approaches estimating Markov parameters are discussed further in the following sections.

3.2.2 Impulse response test

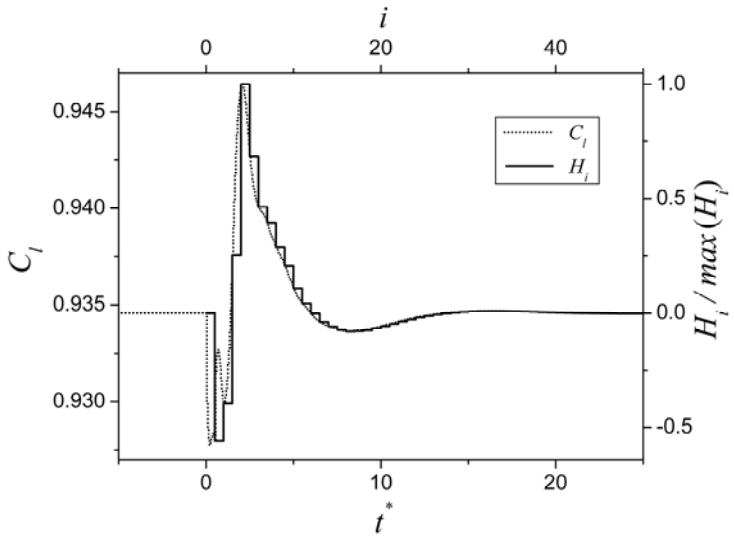

(a) impulse response and identified Markov parameters

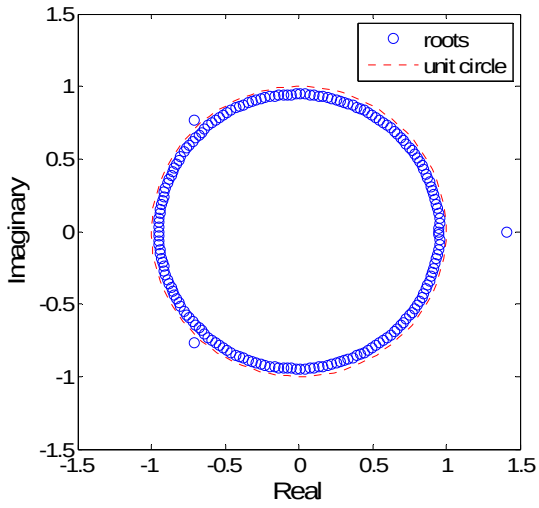

(c) 197 roots of Markov parameter polynomial

Figure 3.13 Impulse response and system identification for lift (Re = 1000, α = 15˚, $V_{app,0}$ = 1 kV, ΔV_{app} = 0.2 kV, H_i: i-th Markov parameter).

Since the output of a linear, time-invariant, causal system can be reproduced with its impulse response, the impulse response is a complete characterization of the system[117]. Moreover, it is straightforward, with a relatively simple setup to obtain the impulse response of a system whose steady state outputs are stable. Especially compared to other

iteration-based algorithms, the system parameters can be estimated with a much smaller number of sampling points.

Figure 3.13 shows an example of the impulse response of the aerodynamic lift and system parameter estimates for the flow-actuator system. For the impulse response test, the actuator operates with the nominal voltage 1 kV, and a finite-magnitude impulse with ΔV_{app} = 0.2 kV is applied at $t^* = 0$. The performance measurement and voltage update are done at every 10th flow time step, i.e., $\Delta t_c^* = 10\Delta t_f^*$, where Δt_c^* and Δt_f^* are the control time step and the flow simulation step, respectively. As shown in Figure 3.13(a), since the measurement and voltage update occur after the flow field is calculated, there is a system delay of at least 1 in the control time scale unit, regardless of the flow time resolution.

The estimated Markov parameters include information about system zeros. More specifically, some of the roots of the Markov parameter polynomial shown in Figure 3.13(b) approximate the zeros that lie outside of the unit circle in the complex domain, i.e., the nonminimum-phase (NMP) zeros or unstable zeros of the linearized transfer function. There are one real and two complex NMP zeros in this case. In most test cases of the current study, the real NMP zero is consistently captured by the impulse response test, whereas the complex ones are not.

For the same case, Figure 3.14(a) demonstrates the impulse response of the aerodynamic drag, which shows less sensitivity to the same impulse and the opposite direction of initial response. Moreover, as opposed to lift, the drag response only shows complex NMP zeros as shown in Figure 3.14(b). In many cases with larger different impulse magnitudes, the linearized transfer function from control to drag shows no NMP zero, i.e., the drag transfer function tends to be minimum-phase. This difference can be explained by considering the flow dynamics under the influence of the DBD actuation.

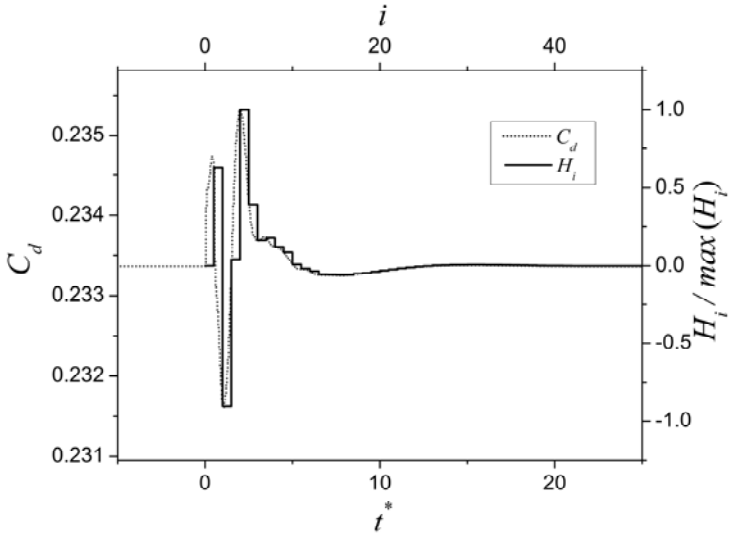

(a) impulse response and identified Markov parameters

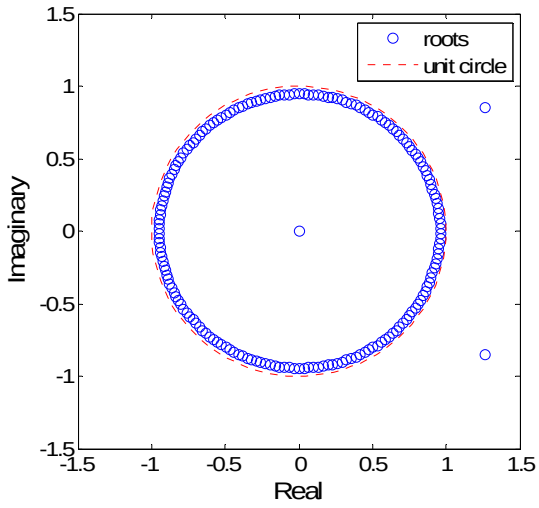

(c) 197 roots of Markov parameter polynomial

Figure 3.14 Impulse response and system identification for drag (Re = 1000, α = 15°, $V_{app,0}$ = 1 kV, ΔV_{app} = 0.2 kV, H_i: i-th Markov parameter).

The step response of a system with an odd number of NMP zeros has initial undershoot; that is, the step response initially moves in the direction opposite to its steady-state value[118]. For example, the step response of a system with one real NMP zero, having positive steady-state output, initially decreases, then increases to reach the steady-state value. A system with multiple NMP zeros repeats the step response with ripples which cross the undisturbed value as many times as the number of real NMP zeros before

reaching the steady-state output. Moreover, for a continuous-time system, the relative undershoot

$$r_y \triangleq \frac{y_{us}}{y_\infty} \geq \frac{0.98}{e^{\lambda t_s} - 1}, \tag{3.15}$$

where λ is the real NMP zero and t_s is the settling time, as shown in Figure 3.15 – i.e., the ratio of the undershoot amplitude and the steady-state value in a step response – is known to decrease as the NMP zero increases[119,120]. By relating the NMP zero and dynamic response of a system, the relative undershoot is informative for understanding the relative NMP zero positions of a system under different conditions. For example, the increased undershoot or decreased steady-state value means a smaller NMP zero as well as a larger relative undershoot. More details about the relation between the real NMP zero and relative undershoot for the flow-actuator system are discussed in 3.4.1.

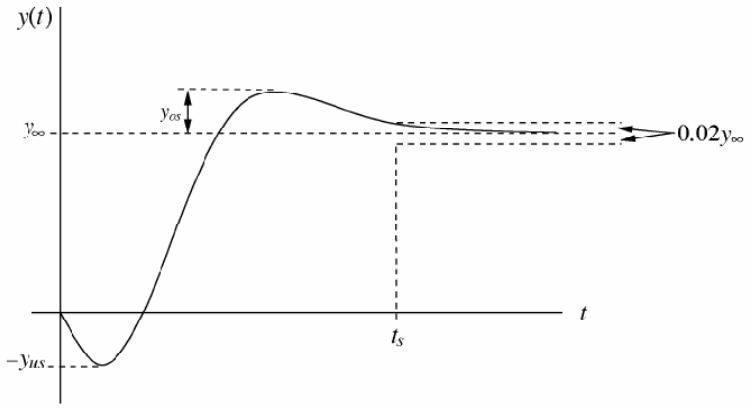

Figure 3.15 Representative impulse response of a system (Reproduced from Stewart and Davison, 2006[119]).

As noted earlier, the impact of the DBD actuation on the flow field under the flow and actuator conditions can be summarized as the intensified suction and pressure peaks around the actuation position, increased wall shear stress, and the reduction of flow separation. At these low-Reynolds numbers, the drag reduction due to the reduced separation region by the induced wall jet is less than the drag increase due to the viscous forces, resulting in the increase of the steady-state drag with actuation. Moreover, at the moment of actuation, the induced jet increases the local viscous drag before affecting the

separated flow region. As a result, the impulse actuation increases drag without undershoot, and the system for drag is either minimum-phase or NMP with an even number of complex NMP zeros. Lift, on the other hand, initially decreases due to the downward flow induced by the negative x_2-directional body force field, but then increases due to the intensified suction and the enhanced pressure recovery by the reduced flow separation, resulting in the step response with initial undershoot. It is consistent with this observation that the impulse response tests for lift show one real NMP zero. Since the initial impact of the actuation on aerodynamic forces determines whether the system has initial undershoot in the step response or not, the local variations of pressure and viscous force fields caused by the DBD actuation are major factors affecting the difference between systems with lift and drag as the performance.

3.2.3 Linearized system realization with ERA

As mentoned earlier, the eigensystem realization algorithm (ERA) utilizes Markov parameters to estimate system matrices. By defining the block-Hankel matrix[114] as

$$\mathcal{H}_{r,s}(j-1) \triangleq \begin{bmatrix} H_j & H_{j+1} & \cdots & H_{j+s-1} \\ H_{j+1} & \iddots & \iddots & \iddots \\ \vdots & \iddots & \iddots & \iddots \\ H_{j+r-1} & \iddots & \iddots & H_{j+r+s-2} \end{bmatrix}, \tag{3.16}$$

and using the factorization of its first set

$$\mathcal{H}_{r,s}(0) = P\Sigma Q, \tag{3.17}$$

the system matrices *A, B, C* and *D* in Eqs. (3.6)-(3.7) can be estimated by

$$A = \Sigma_0^{-1/2} P^T \mathcal{H}_{r,s}(1) Q^T \Sigma_0^{-1/2}, \tag{3.18}$$

$$B = \Sigma_0^{1/2} Q \begin{bmatrix} I_{l_u} \\ 0_{sl_u \times l_u} \end{bmatrix}, \tag{3.19}$$

$$C = \begin{bmatrix} I_{l_y} & 0_{l_y \times r l_y} \end{bmatrix} P \Sigma_0^{1/2}, \tag{3.20}$$

$$D = H_0, \tag{3.21}$$

where Σ_0 is the diagonal matrix reduced from Σ by truncating the negligible singular values. If there are *n* dominant singular values in Σ, in other words, $\mathcal{H}_{r,s}(0)$ is an *n*-rank matrix, the order of the model can be truncated to *n*, resulting in a minimal realization.

Once the impulse response is available, the block-Hankel matrix can be constructed. For example, for the same case as Figure 3.14, the singular values of the block-Hankel matrix shown in Figure 3.16(a) indicate that the order of the system for lift is approximately 6. Figure 3.16(b) shows the estimation of poles and zeros along with the roots of the Markov parameter polynomial. Both estimations show good agreement in the NMP zeros approximation. In addition, all the poles are located in the unit circle, implying that the system is stable. The realization of the linearized flow-actuator system for drag in Figure 3.17 shows similar trends in the dynamics estimation.

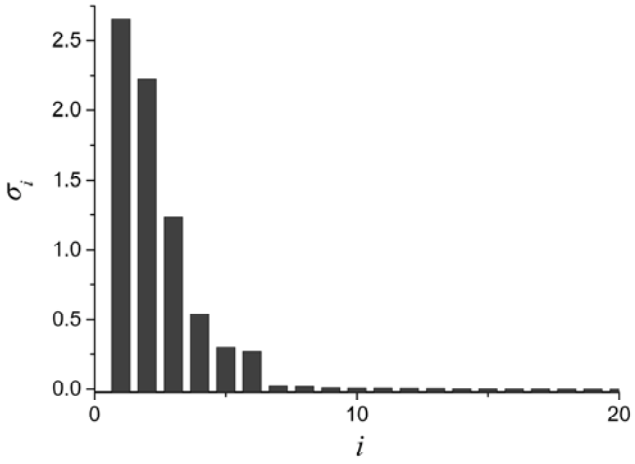

(a) singular values of the block-Hankel matrix

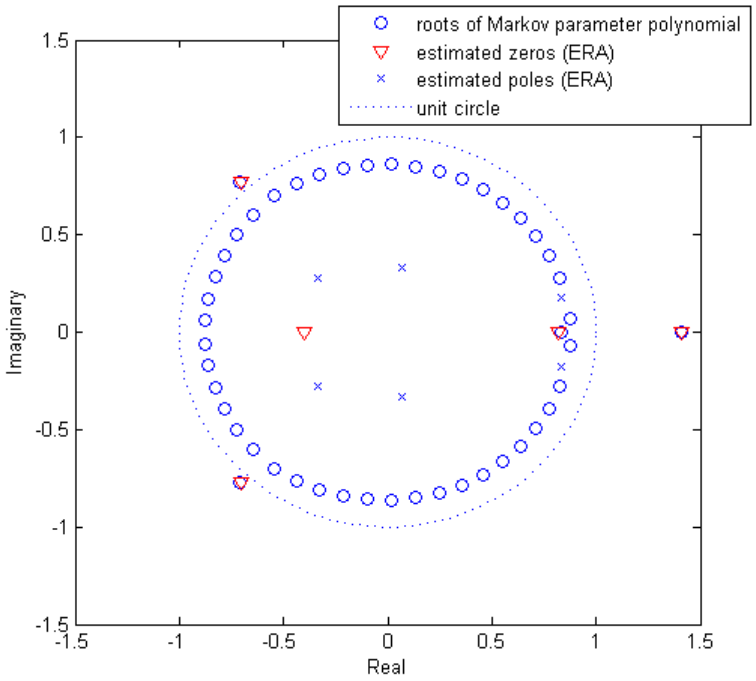

(b) estimated poles and zeros

Figure 3.16 Realization of the linearized flow-actuator system for lift ($AR = \infty$, $Re = 1000$, $\alpha = 15^\circ$, $V_{app,0} = 1$ kV, $\Delta V_{app} = 0.2$ kV, σ_i: i-th singular value).

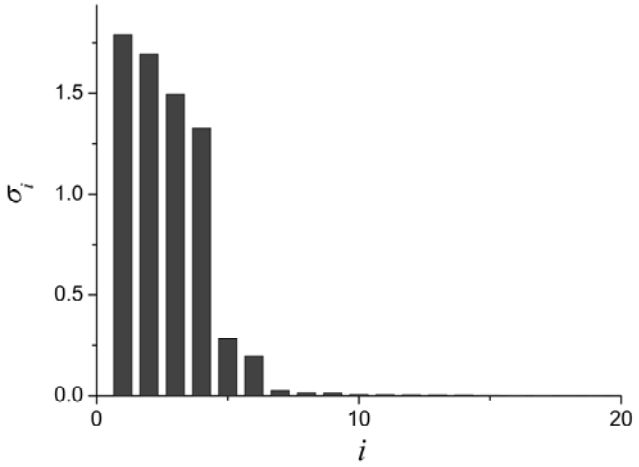

(a) singular values of the block-Hankel matrix

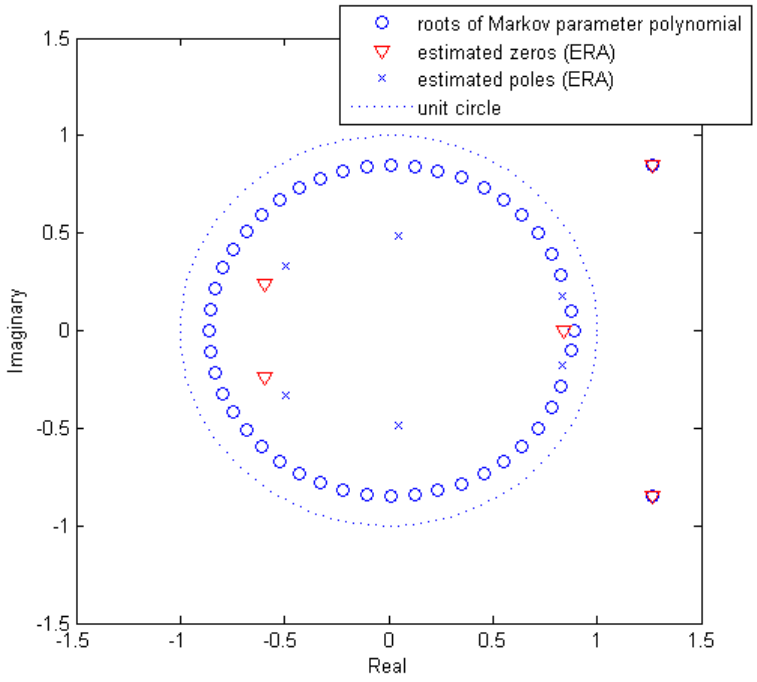

(b) estimated poles and zeros

Figure 3.17 Realization of the linearized flow-actuator system for drag ($AR = \infty$, $Re = 1000$, $\alpha = 15^{\circ}$, $V_{app,0} = 1$ kV, $\Delta V_{app} = 0.2$ kV, σ_i: i-th singular value).

3.2.4 Recursive least squares (RLS) algorithm

Although the impulse response test can provide Markov parameters directly, the test may not be available, especially when the system is unstable or online system identification is necessary. Instead of using the whole set of input and output data, a recursive system-identification algorithm seeks the system parameters by updating the estimates of the parameters using an input-output pair at each time step. Since a specific mode of a system can or cannot be excited depending on the input signal, the choice of an appropriate input signal is critical in any iterative identification algorithm. In order to provide a broad bandwidth input signal, the white noise signal, which is a random signal having constant probability density in frequency domain up to the Nyquist frequency, is widely accepted.

As described in Ljung and Soderstrom (1983)[83], a linear, time-invariant system can be expressed with the regression relation

$$y(t) = \theta^T \varphi(t) + v(t), \tag{3.22}$$

where $\varphi(t)$ is the regressor vector composed of input and output data, θ is the system parameter vector, and $v(t)$ is the prediction error or noise. Then, by minimizing the prediction error using a least squares function, the system parameter vector for $t = N$ can be estimated as

$$\hat{\theta}(N) = \left[\sum_{i=1}^{N} \varphi(t)\varphi^T(t)\right]^{-1} \sum_{i=1}^{N} \varphi(t) y(t). \tag{3.23}$$

By introducing a recursive formulation, the system parameter vector can be updated at each time step by

$$\hat{\theta}(t) = \hat{\theta}(t-1) + \frac{1}{t} R^{-1}(t)\varphi(t)\left[y(t) - \hat{\theta}^T(t-1)\varphi(t)\right], \tag{3.24}$$

$$R(t) = R(t-1) + \frac{1}{t}\left[\varphi(t)\varphi^T(t) - R(t-1)\right]. \tag{3.25}$$

Using the matrix inversion lemma

$$\left[A+BCD\right]^{-1}=A^{-1}-A^{-1}B\left[DA^{-1}B+C^{-1}\right]^{-1}DA^{-1}, \tag{3.26}$$

which is valid for arbitrary matrices *A, B, C* and *D* with compatible dimensions, the recursive formulation is equivalently

$$\hat{\theta}(t)=\hat{\theta}(t-1)+L(t)\left[y(t)-\hat{\theta}^{T}(t-1)\varphi(t)\right], \tag{3.27}$$

$$L(t)=\frac{P(t-1)\varphi(t)}{1+\varphi^{T}(t)P(t-1)\varphi(t)}, \tag{3.28}$$

$$P(t)=P(t-1)+\frac{P(t-1)\varphi(t)\varphi^{T}(t)P(t-1)}{1+\varphi^{T}(t)P(t-1)\varphi(t)}. \tag{3.29}$$

The initial values can be chosen as $P(0)=cI$ and $\hat{\theta}(0)=0$ with a large constant *c* for a faster decay of the effect of initial values.

Usually the RLS algorithm requires a much larger number of data points than the impulse response test to identify system parameters. Instead of the flow-actuator models Eqs. (3.1)-(3.5), the state-space model realized by ERA with the Markov parameters of the flow-actuator system is used to assess the RLS algorithm. Figure 3.18 shows the original impulse responses of lift and drag of the flow-actuator system compared with the reconstructed impulse response of the ARMA model that is estimated with the RLS algorithm. The estimation is done by applying the white noise input to the state-space model. The lift and drag responses estimated with 500 data points show good agreement with the original impulse responses.

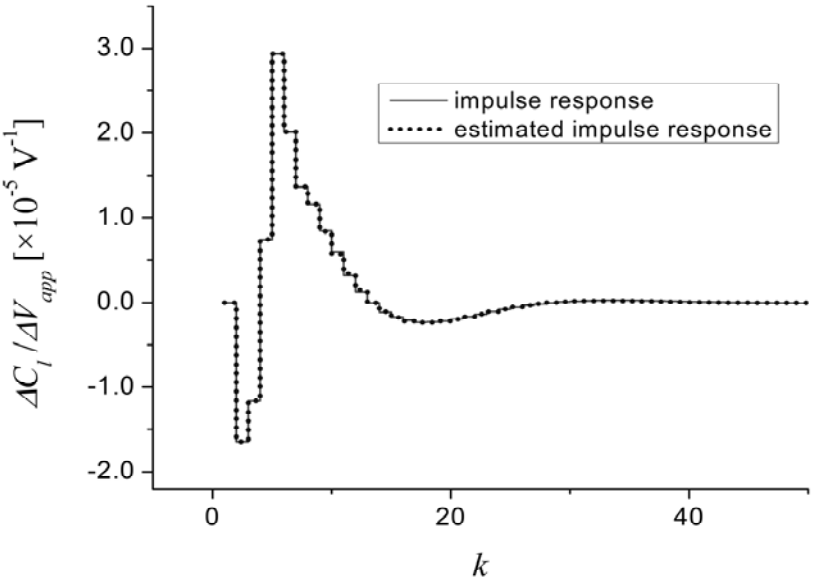

(a) lift

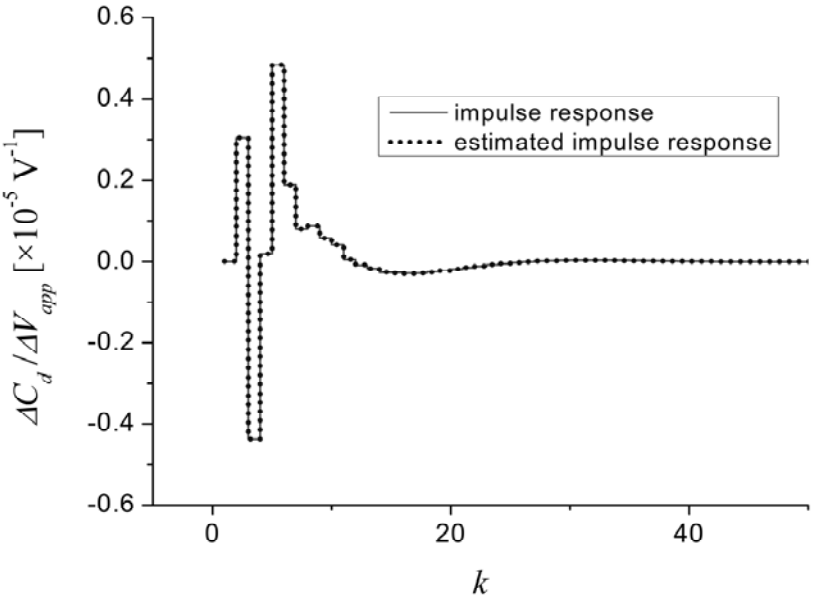

(b) drag

Figure 3.18 Impulse response estimation with ERA and RLS (50 samplings of the impulse response, 500 white-noise data points).

3.2.5 Identification of a real nonminimum-phase zero

When it is known that there is one nonminimum-phase (NMP) zero for a stable rational transfer function, an adaptive input along with the RLS algorithm can be used to estimate the zero as shown in Rojas et al. (2009)[84]. In their study, an arbitrary finite-dimensional, stable, linear time-invariant system with a NMP zero is modeled with a two-parameter FIR model

$$y(t) = \varphi^T(t)\theta, \tag{3.30}$$

where $\varphi(t) = \begin{bmatrix} u(t-1) & u(t-2) \end{bmatrix}^T$ and $\theta = \begin{bmatrix} \theta_1 & \theta_2 \end{bmatrix}^T$. Then, the regular recursive least squares algorithm in Eq. (3.24) and Eq. (3.25) can be combined with the adaptive input

$$u(t) = \rho(t-1)u(t-1) + r(t-1)\sqrt{1-\rho^2(t-1)} \tag{3.31}$$

where $r(t)$ is a sequence of zero-mean random variables independent of the exogenous noise, and $\rho(t)$ is a variable dependent on the estimate of the NMP zero $\hat{z}_{NMP}(t)$. By using $R(t) = \begin{bmatrix} 1 & \rho(t-1) \\ \rho(t-1) & 1 \end{bmatrix}$, it is shown that the NMP zero can be estimated as

$$\rho(t) = \frac{1}{\hat{z}_{NMP}(t)} = -\frac{\hat{\theta}_1(t)}{\hat{\theta}_2(t)}. \tag{3.32}$$

For example, the algorithm is applied to the estimation of the real NMP zero for the case of Re = 300 and x_{act} = 0.6c. As described in the previous section, ERA is used to approximate the flow-actuator system with the linearized transfer function. Figure 3.19(a) shows that the convergence of the estimate requires a large number of data points, compared to the impulse response and RLS algorithm. However, if some uncertainty is allowed, say 10 %, the data set can be much shorter, such as $O(100)$. As shown in Figure 3.19(b), although the estimation algorithm is based on the simplified model structure, the real NMP zero can be approximated with good accuracy.

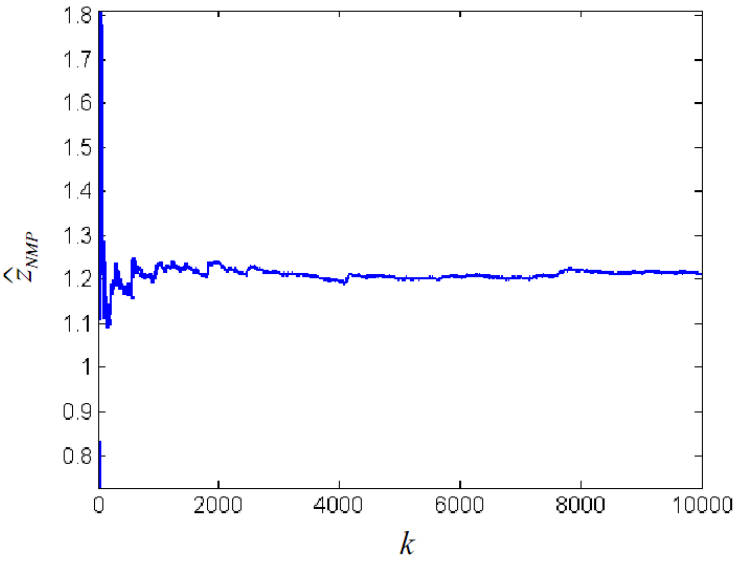

(a) time history of the estimated real NMP zero

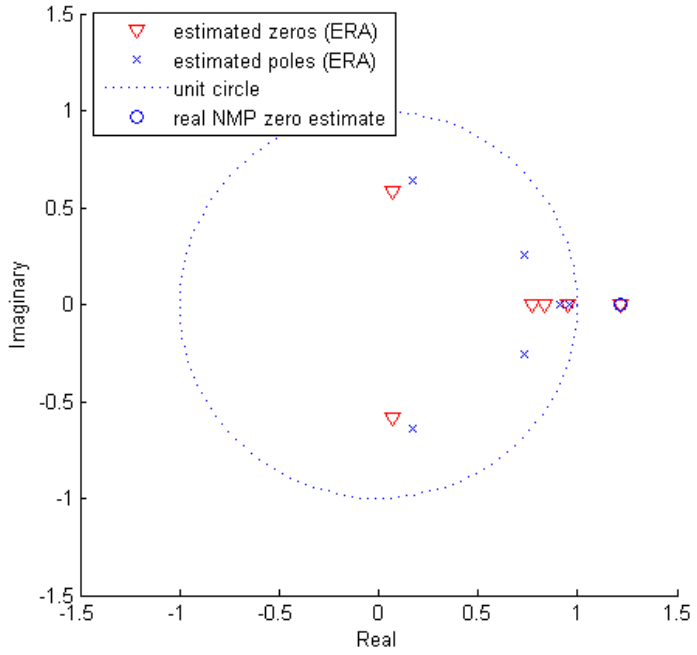

(b) zeros and poles estimated with ERA, and the real NMP zero estimate

Figure 3.19 Real NMP zero identification[84] (*Re* = 300, *AoA* = 15°, x_{act} = 0.6*c*).

3.3 Retrospective cost adaptive control algorithm

Adaptive control is a control scheme based on adjustable controller gains. In this approach, the controller gains are dynamically updated in response to changes in the plant and disturbance dynamics[121]. Compared to fixed gain control, which is designed for a known range of parameter uncertainties, adaptive control is capable of achieving target performance with larger parameter uncertainties[122]. Adaptive control especially aims at adjusting system and/or controller parameters under uncertainties from disturbances, and time-varying and unmodeled system dynamics. Although adaptive control is regarded as a less-model or model-free approach, it requires a certain amount of knowledge of the system to be controlled, which is one of the key issues in this technique[123].

In this section, the adaptive control algorithm shown in Santillo and Bernstein (2010)[116] is summarized for a single-input, single-output control system. Consider the single-input, single-output linear discrete-time system

$$x(k+1) = Ax(k) + Bu(k) + D_1 w(k), \tag{3.33}$$

$$z(k) = E_1 x(k) + E_0 w(k), \tag{3.34}$$

where $x(k) \in \mathbb{R}^n$, $z(k) \in \mathbb{R}$, $u(k) \in \mathbb{R}$, $w(k) \in \mathbb{R}^{l_w}$ are the state, performance, control and exogenous command and/or disturbance signal with $k \geq 0$. The adaptive controller minimizes the performance variable z in the presence of the exogenous signal w, which could be a disturbance, a command, or both. In this study, the performance variable is the variation of the aerodynamic lift acting on the airfoil under inlet flow conditions with a sinusoidal disturbance from its nominal (undisturbed) value.

For the general control problem given by Eqs. (3.33)-(3.34), a strictly proper time-series controller of order n_c, similar to Eq. (3.11), can be defined as

$$u(k) = \sum_{i=1}^{n_c} M_i(k) u(k-i) + \sum_{i=1}^{n_c} N_i(k) z(k-i), \tag{3.35}$$

where, for all $i=1,\cdots,n_c$, $M_i(k)$, $N_i(k)\in\mathbb{R}$ are given by the adaptive law given below. The control can be expressed as

$$u(k)=\theta^T(k)\phi(k), \tag{3.36}$$

where

$$\theta(k)\triangleq\begin{bmatrix}N_1(k) & \cdots & N_{n_c}(k) & M_1(k) & \cdots & M_{n_c}(k)\end{bmatrix}^T\in\mathbb{R}^{2n_c} \tag{3.37}$$

is the controller parameter matrix, and the regressor vector $\phi(k)$ is given by

$$\phi(k)\triangleq\begin{bmatrix}z(k-1)\\ \vdots \\ z(k-n_c)\\ u(k-1)\\ \vdots \\ u(k-n_c)\end{bmatrix}\in\mathbb{R}^{2n_c} \tag{3.38}$$

For positive integer μ, the extended control vector can be defined by

$$U(k)\triangleq\begin{bmatrix}u(k)\\ \vdots \\ u(k-p_c+1)\end{bmatrix}\in\mathbb{R}^{p_c} \tag{3.39}$$

where $p_c\triangleq\mu+1$. From Eq. (3.36), it follows that the extended control vector $U(k)$ can be written as

$$U(k)\triangleq\sum_{i=1}^{p_c}L_i\theta^T(k-i+1)\phi(k-i+1), \tag{3.40}$$

where

$$L_i \triangleq \begin{bmatrix} 0_{(i-1)\times 1} \\ 1 \\ 0_{(p_c-i)\times 1} \end{bmatrix} \in \mathbb{R}^{p_c} \tag{3.41}$$

Next, define the retrospective performance

$$\hat{z}\left(\hat{\theta},k\right) \triangleq z(k) - \bar{B}_{zu}\left(U(k) - \hat{U}\left(\hat{\theta},k\right)\right), \tag{3.42}$$

where $\hat{U}\left(\hat{\theta},k\right) \triangleq \sum_{i=1}^{p_c} L_i \hat{\theta}^T \phi(k-i+1)$, $\hat{\theta} \in \mathbb{R}^{2n_c}$ is an optimization variable, and the control matrix $\bar{B}_{zu}$ is given by Eq. (3.53) below. Note that $\hat{z}\left(\hat{\theta},k\right)$ is obtained by modifying the performance variable $z(k)$ based on the difference between the actual past control inputs $U(k)$ and the recomputed past control inputs $\hat{U}\left(\hat{\theta},k\right)$, assuming that $\hat{\theta}$ had been used in the past.

Now, consider the retrospective cost function

$$\hat{J}\left(\hat{\theta},k\right) \triangleq \hat{z}^2\left(\hat{\theta},k\right) + \alpha_l \left(\hat{\theta} - \theta(k)\right)^T \left(\hat{\theta} - \theta(k)\right), \tag{3.43}$$

where the learning rate α_l affects the transient performance and the convergence speed of the adaptive control algorithm. Substituting Eq. (3.42) into Eq. (3.43) yields

$$\hat{J}\left(\hat{\theta},k\right) \triangleq \hat{\theta}^T A(k)\hat{\theta} + b^T(k)\hat{\theta} + c(k), \tag{3.44}$$

where

$$A(k) \triangleq D^T(k)D(k) + \alpha_l I_{2n_c}, \tag{3.45}$$

$$b(k) \triangleq 2D^T(k)\left(z(k) - \bar{B}_{zu}U(k)\right) - 2\alpha_l \theta(k), \tag{3.46}$$

$$c(k) \triangleq \left(z(k) - \bar{B}_{zu} U(k)\right)^2 - \alpha_l \theta^T(k)\theta(k), \tag{3.47}$$

and $D(k) \triangleq \bar{B}_{zu} \sum_{i=1}^{p_c} \left(L_i \phi^T(k-i+1)\right)$. Since $A(k)$ is positive definite, $\hat{J}\left(\hat{\theta}, k\right)$ has the unique global minimizer $-\frac{1}{2} A^{-1}(k) b(k)$. Thus, the update law is given by

$$\theta(k+1) = -\frac{1}{2} A^{-1}(k) b(k). \tag{3.48}$$

The adaptive controller in Eq. (3.36) and Eqs. (3.45)-(3.48) requires limited model information of the system in Eqs. (3.33)-(3.34), i.e., knowledge of $\bar{B}_{zu}$. In this study, $\bar{B}_{zu}$ is constructed using estimates of the system's relative degree, first nonzero Markov parameter and the nonminimum-phase zeros of the transfer function from *u* to *z*. Consider the transfer function from *u* to *z* given by

$$G_{zu}(z) \triangleq E_1 \left(zI - A\right)^{-1} B, \tag{3.49}$$

which can be written as

$$G_{zu}(z) \triangleq H_d \frac{\beta(z)}{\alpha(z)}, \tag{3.50}$$

where the relative degree $d \geq 1$ is the smallest positive integer *i* such that *i*-th Markov parameter H_i is nonzero, and $\alpha(z)$ and $\beta(z)$ are monic coprime polynomials. If $\beta(z)$ has the factorization

$$\beta(z) = \beta_u(z)\beta_s(z), \tag{3.51}$$

where $\beta_s(z)$ is a monic polynomial of degree n_s whose roots lie inside the unit circle, and $\beta_u(z)$ is a monic polynomial of degree n_u whose roots lie on or outside the unit circle. Then, $\beta_u(z)$ can be written as

$$\beta_u(z) = z^{n_u} + \beta_{u,1} z^{n_u-1} + \cdots + \beta_{u,n_u-1} z + \beta_{u,n_u}. \tag{3.52}$$

By letting $\mu = n_u + d$, the resulting system parameter matrix $\bar{B}_{zu}$ is given by

$$\bar{B}_{zu} \triangleq H_d \begin{bmatrix} 0_{1\times d} & 1 & \beta_{u,1} & \cdots & \beta_{u,n_u} \end{bmatrix} \in \mathbb{R}^{1\times p_c}. \tag{3.53}$$

Note that $\bar{B}_{zu}$ is constructed using the relative degree *d*, the first nonzero Markov parameter H_d, and the NMP zeros the transfer function from *u* to *z*. Other constructions of $\bar{B}_{zu}$ are shown in Santillo and Bernstein (2010)[116].

3.4 Identification of flow-actuator system

3.4.1 Step response test

As mentioned in 3.2.2, the step response of a system can help to characterize system parameters. Typical step responses of the flow-actuator system for drag and lift are shown in Figure 3.20. The step response of drag shows no undershoot. The maximum as well as steady-state values are lower when the Reynolds number is higher. Lift, on the other hand, decreases first under the step actuation and reaches a positive steady-state value. It is interesting to notice that the undershoot magnitude does not change much with the Reynolds number, whereas the steady-state value is very sensitive to the Reynolds number.

The observations can be related to the influence of the DBD actuation on the flow field. The induced flow due to the actuation accompanies the high shear layer near the actuation location, resulting in a monotonic drag increase, along with the secondary effect of the changes in wake and separated-flow regions. The lift evolution, on the other hand, is more affected by the pressure and suction peaks, as well as the changes in wake and separated-flow regions. Due to the difference in the response time between these impacts, the reverse-direction lift variation (or undershoot) precedes the lift increase, which is prominent with the higher Reynolds number.

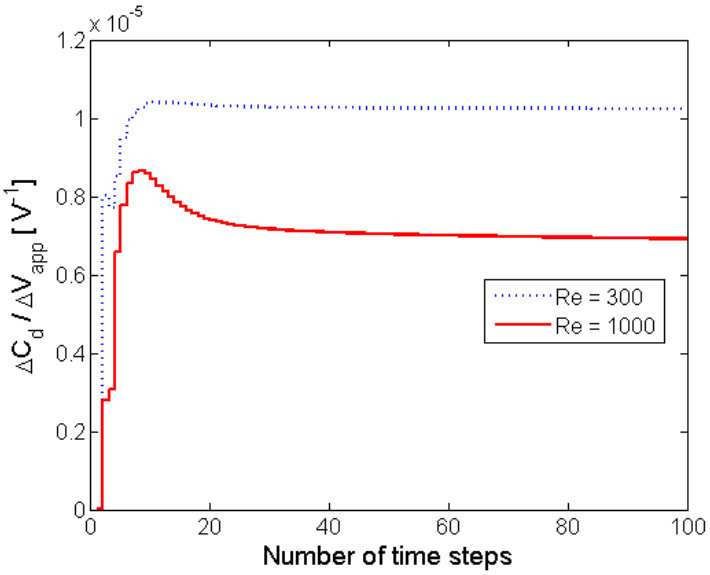

(a) drag

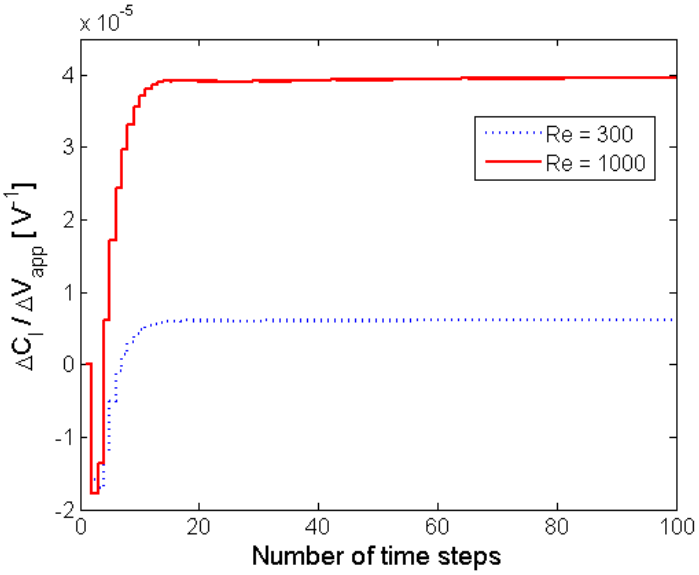

(b) lift

Figure 3.20 Step response of the flow-actuator system.

3.4.2 Real NMP zero with flow and actuator conditions

For the test cases, the identified system parameters, or more specifically the first nonzero Markov parameter and real NMP zero, are dependent on the flow and actuator conditions. The relevant questions can be summarized as the following. How much do the system

parameters change according to the flow and actuation conditions, and actuation itself? How accurately should the system parameters be estimated or how much tolerance to their changes does the control system have? Is it possible to minimize or incorporate the parametric changes with the control algorithm to achieve control goals? The nonlinearity caused by the parametric change can invalidate the linear model assumption on which the control algorithm based. Thus, assessing the parametric change helps to address the limitation of the current framework and to suggest directions to improve control performance.

For a continuous-time system, since the real NMP zero value is inversely proportional to the relative undershoot, as mentioned in the previous section, the change in either the undershoot magnitude or the steady-state value in the lift step response indicates the variation of the real NMP zero; the NMP zero increases if either the undershoot amplitude decreases or if the steady-state lift increases. The same trend is observed for the discrete-time flow-actuator system in this study. As an example, the relation between the relative undershoot and the real NMP zero in lift for Re = 300 is shown in Figure 3.21(a) for different actuation locations. For both pressure lift and total lift, the real NMP zero increases, as the actuation position moves downstream. Since the increase of the steady-state lift caused by the increase of x_{act}/c results in the decrease of the relative undershoot, the relation between the relative undershoot and real NMP zero is consistent with the one in continuous-time systems.

For different flow conditions, the impact of the wing aspect ratio on the real NMP zero is shown in Figure 3.21(b), and the trend of the NMP zero variation is consistent with the impact of the actuation location, i.e., the enhanced steady-state lift with a higher aspect ratio wing decreases the relative undershoot.

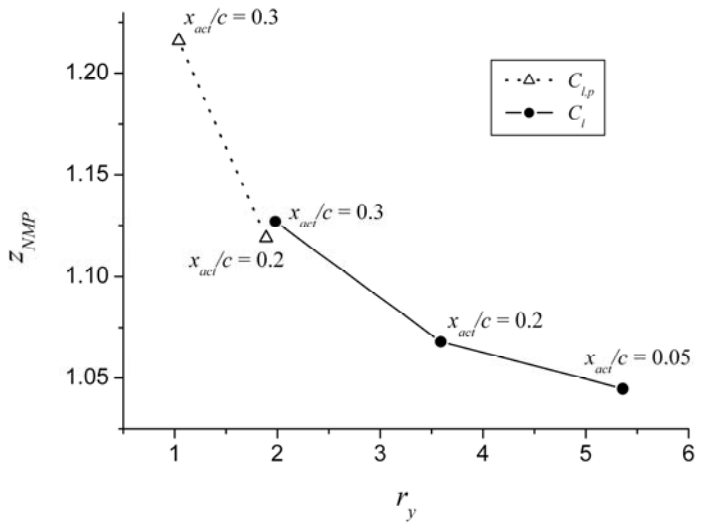

(a) relative undershoot with actuation location (Re = 300, $V_{app,0}$ = 1 kV, ΔV_{app} = 3 kV, $C_{l,p}$: pressure lift coefficient)

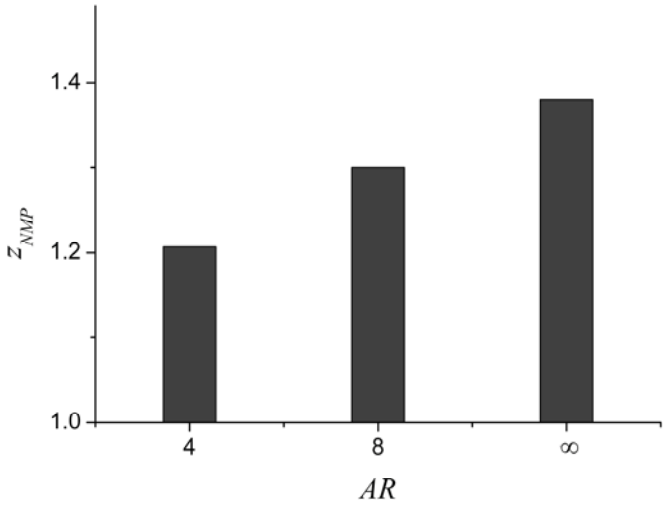

(b) wing aspect ratio (Re = 1000, x_{act}/c = 0.2, $V_{app,0}$ = 2 kV, ΔV_{app} = 1 kV)

Figure 3.21 Geometric conditions and NMP zero.

As discussed in 3.5, in this study it is observed that the feedback performance is significantly affected by the disturbance period in the range of T^* = 5 ~ 100 and magnitude of the disturbance in vertical free-stream speed. A higher disturbance magnitude changes system dynamics by changing both the instantaneous angle of attack and flow speed. Furthermore, the control voltage variation at each time step should be

increased as the disturbance amplitude increases. As mentioned in 3.3, the system parameters required by the adaptive controller include the NMP zero and the first nonzero Markov parameter. Figure 3.22 shows that both parameter estimates are dependent on the impulse magnitude. The real NMP zero of lift is asymmetric with respect to the sign of the impulse voltage and decreases as the impulse magnitude approaches zero. On the other hand, the first nonzero Markov parameter increases as the impulse magnitude approaches zero. These parametric drifts indicate the sensitivity of system parameters on voltage increment or disturbance magnitude. In Figure 3.22, it is also shown that the change in vertical free-stream speed also induces the parametric drifts.

In Figure 3.23, the variations of the real NMP zero and first nonzero Markov parameter according to the Reynolds number, as well as the voltage increment, are shown. As the Reynolds number increases between *Re* = 300 and 1000, the real NMP zero becomes larger, which is analogous to the trend with the relative undershoot, considering the increase of the steady-state lift at higher Reynolds numbers. Although the undershoot magnitude is observed to increase as the Reynolds number increases, the impact of the steady-state-lift increase at a higher Reynolds number dominates the relative undershoot. On the other hand, the impact of Reynolds number on the first nonzero Markov parameter is the opposite, as shown in Figure 3.23(b); the parameter decreases as Reynolds number increases. Considering the absolute value of the parameter, however, the trend represents the increased high-frequency gain for a higher Reynolds number.

As mentioned earlier, there exist flow and control time scales in the current flow control simulations. The non-dimensional time resolution of flow simulations in this study is fixed to $\Delta t_f^* = U_\infty \Delta t_f / c = 0.05$. Since the discontinuous voltage update at each control time step induces high-frequency input to the flow-actuator system, the flow time resolution should be sufficient to resolve flow dynamics critical in system parameters. In Figure 3.24(a), for example, the impulse responses with $\Delta t_f^* = 0.05$ (case A) and with $\Delta t_f^* = 0.01$ (case B) are compared, while keeping the control time resolution the same. The transient oscillation between t^* = 5 and 12 is not captured with the coarser time resolution. However, the overall responses (or system parameters) are consistent with

each other, and the estimated real NMP zero remains virtually same, implying the current flow time resolution is sufficient to capture key flow dynamics of the system.

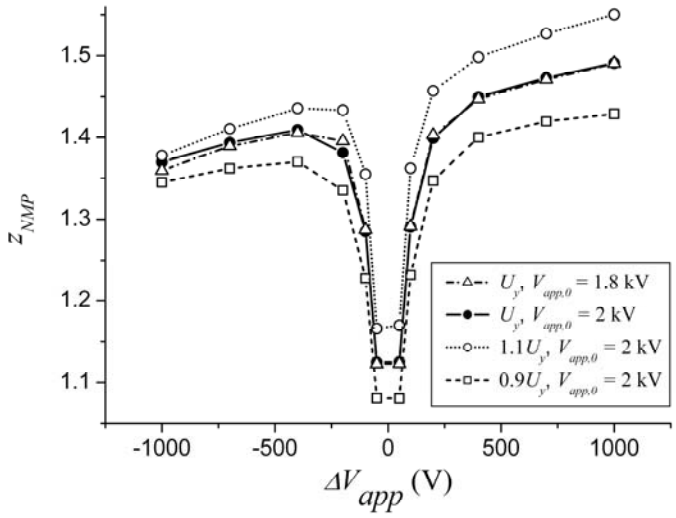

(a) NMP zero

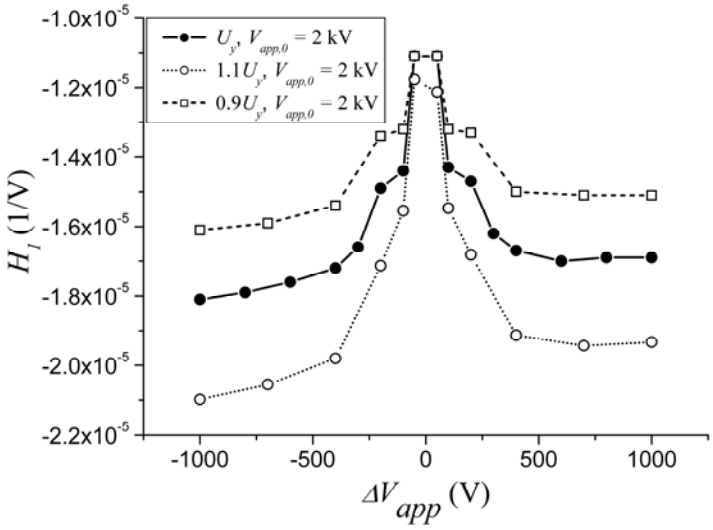

(b) first nonzero Markov parameter

Figure 3.22 Impulse magnitude and system parameters (*Re* = 1000, x_{act}/c = 0.2).

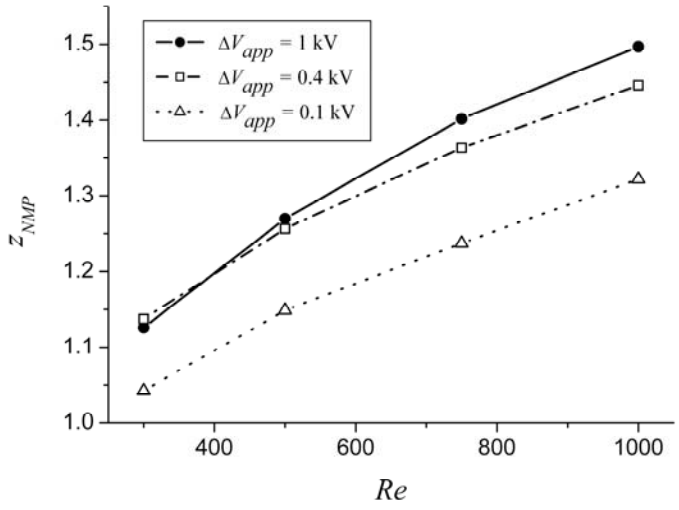

(a) NMP zero

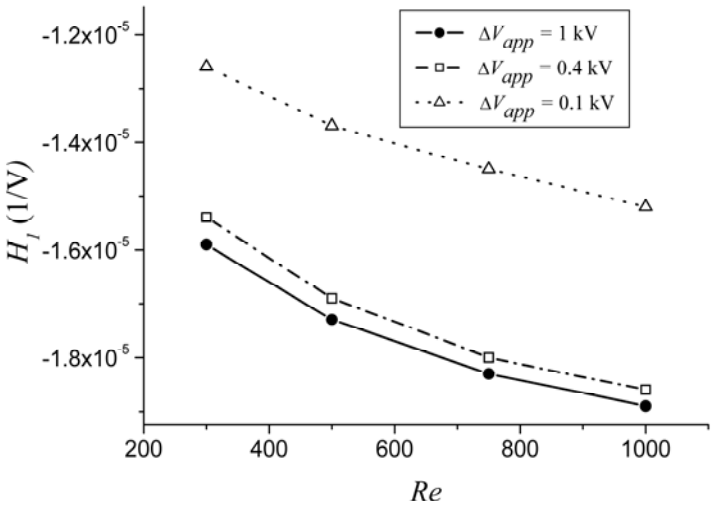

(b) first nonzero Markov parameter

Figure 3.23 Reynolds number and system parameters (x_{act}/c = 0.2, $V_{app,0}$ = 1 kV).

The control time resolution, on the other hand, significantly affects the system parameters. For example, the comparison between $\Delta t_c^* = 0.5$ (case B) and $\Delta t_c^* = 0.1$ (case C) in Figure 3.24(b) indicates that the smaller control time step not only causes reduced impact of the impulse and resolves higher frequencies, but also results in the noticeably different flow response. Moreover, the estimated linearized transfer function of the actuator-flow system with $\Delta t_c^* = 0.1$ (case C) shows three NMP zeros located close to the unit circle, as opposed to the one real NMP zero with the larger control time step. As a result, it is observed in this study that the increase of control time resolution can limit performance of feedback control. Although the higher sampling and updating rate is known to be beneficial in control performance, the result implies that there can be some optimal control time step, which achieves sufficient bandwidth of the control system and favorable locations of NMP zeros at the same time.

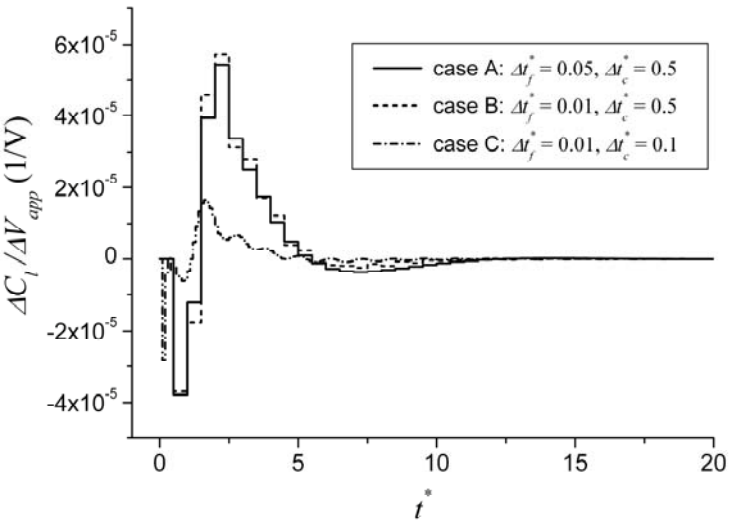

(a) time resolutions and impulse response

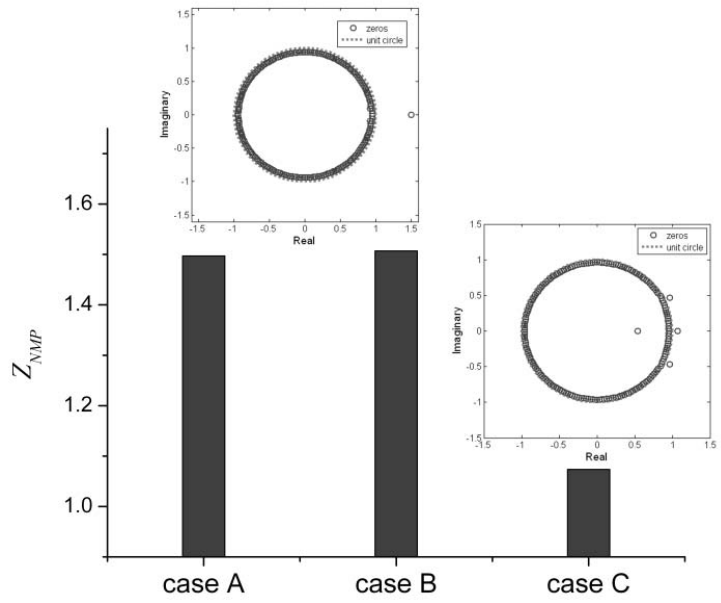

(b) estimated NMP zeros and their locations in the complex domain

Figure 3.24 Flow and control time resolutions and system parameters for lift (Re = 1000, α = 15°, $V_{app,0}$ = 1 kV, ΔV_{app} = 1 kV).

3.5 Closed-loop control of unsteady aerodynamics

3.5.1 Closed-loop control setup

Assuming that no information about the flow unsteadiness is known *a priori*, the retrospective adaptive controller is applied to the feedback loop to eliminate the impact of the flow unsteadiness. The ratio of control and flow time resolutions is set to 10 to limit the bandwidth of the control system. For sampling data, the zero-order-data hold[124], which keeps the control constant between control time steps, is used.

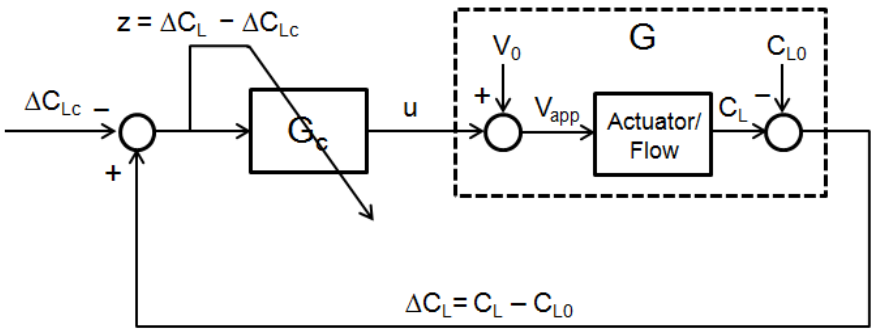

Figure 3.25 Block diagram for feedback control.

In Figure 3.25, the feedback control setup is shown with block diagrams. The input to the flow-actuator system is the actuation voltage V_{app}, which is the summation of the control input u and the nominal voltage V_0. The measurement is aerodynamic lift of the wing, which comprises the performance z. In order to regulate the orders of variables, the performance and control input are scaled accordingly inside the controller.

The performance is defined as the difference between the current lift deviation from the nominal value and the target lift increment. When the control objective is command following, i.e., adjusting the lift coefficient according to a command signal, the target lift increment can be set as the difference between the target lift coefficient and the lift coefficient under actuation with the nominal voltage. The disturbance-rejection control, on the other hand, can be realized by setting ΔC_{Lc} to be zero.

If the objective is command-following control while there exist disturbances to be cancelled, ΔC_{Lc} can simply be set to the command instead of zero. In the current study, only the disturbance-rejection cases are considered.

3.5.2 Disturbance rejection flow control

In this section, the retrospective adaptive controller is applied to mitigating the influence of sinusoidal disturbances in the vertical free-stream speed. The objective is to minimize the difference between the undisturbed lift with the nominal actuation and the measured lift under the influence of the disturbance. Two cases with different disturbance frequency and amplitude are shown in Figure 3.26(a) and (b). In both cases, the impact of sinusoidal disturbances on the airfoil lift is suppressed by the DBD actuator, with the time-varying voltage signal determined by the controller. The fluctuation of drag, on the other hand, is amplified for $T^* = 100$, while suppressed for $T^* = 10$, which implies that the actuation can be beneficial in both lift and drag, depending on the disturbance frequency.

The variation in vertical flow speed induces changes in both flow speed and angle of attack, and aerodynamic forces are also subject to the response of the separated flow to the changes. As shown in Figure 3.26(a), for a disturbance with a lower frequency and a higher amplitude, the phase difference between open-loop drag and lift fluctuations is larger than the one with a higher frequency and a lower amplitude, as in Figure 3.26(b). In addition, the closed-loop control voltage is close to the reverse of the lift variation for both cases, resulting in the suppression of the lift fluctuation. As a result, the control voltage signal of $T^* = 100$ is in phase with the drag fluctuation, amplifying the drag fluctuation. On the other hand, drag and lift are in phase with each other for $T^* = 10$, and the control voltage suppresses both drag and lift fluctuations.

For the case of Figure 3.26(a), streamlines and pressure contours under the open-loop (i.e., constant voltage) actuation are shown in Figure 3.27(a) and (b), where the lift is minimum and maximum, respectively. Since the amplitude of the closed-loop voltage variation is too small to cause a noticeable difference in the flow structure, the two instants in Figure 3.27 also correspond the phases when the closed-loop control voltage is maximum and minimum, respectively. The distribution shown with the dotted line is the

local pressure difference between the closed-loop and open-loop actuations at each phase. The sections with dotted lines inside and outside the airfoil geometry denote the regions where the voltage change causes pressure increase and pressure decrease, respectively.

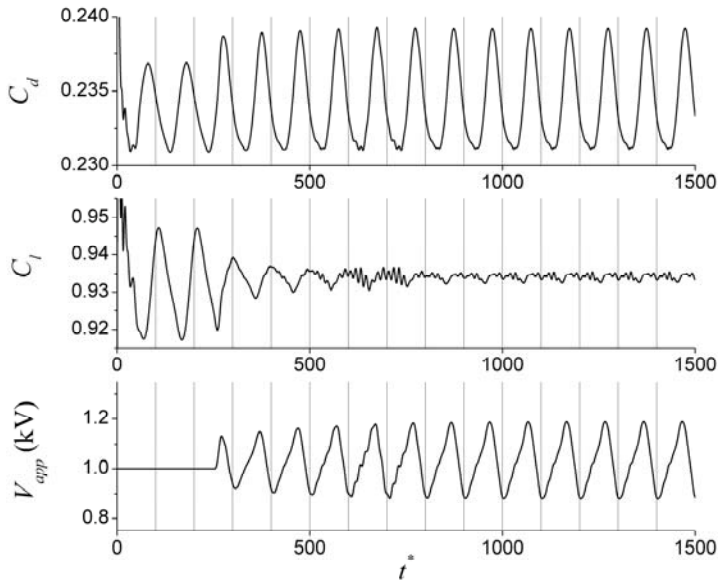

(a)$T^* = 100$, $\alpha_d = 0.06$

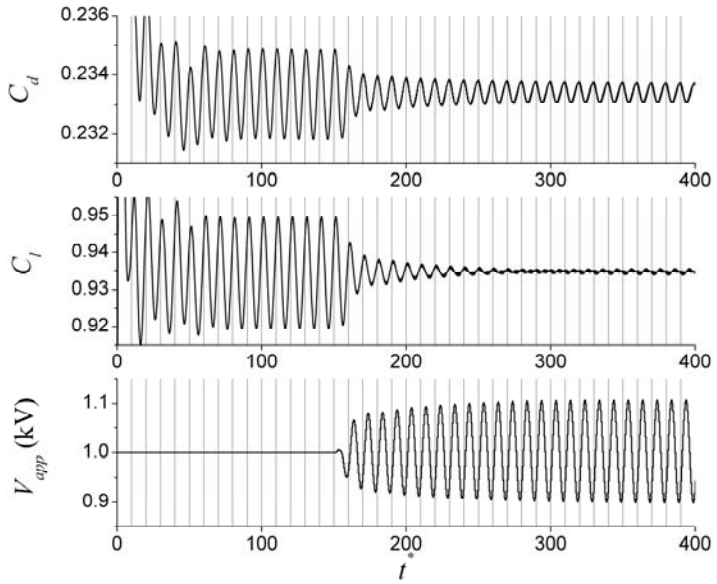

(b)$T^* = 10$, $\alpha_d = 0.01$

Figure 3.26 Disturbance rejection of lift; drag coefficient, lift coefficient and applied voltage (Re = 1000, $AR = \infty$, $\alpha = 15^\circ$, $V_{app,0}$ = 1 kV, learning rate = 200, n_c = 50, 3 system parameters capturing 1 NMP zero and delay).

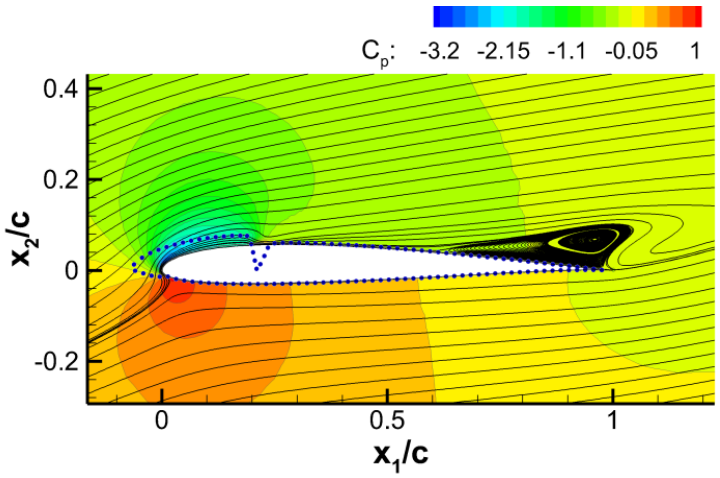

(a) minimum lift (maximum voltage)

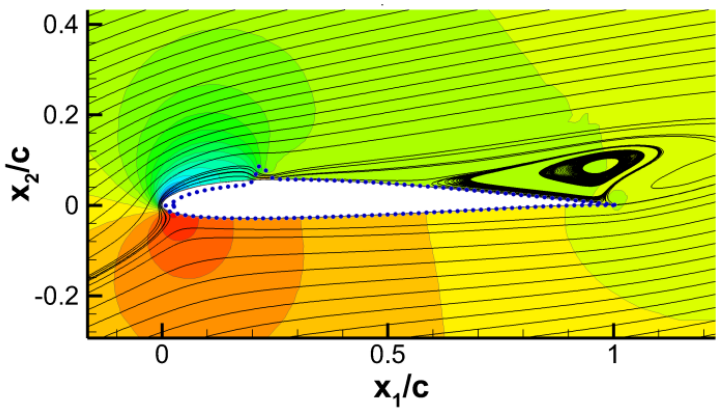

(b) maximum lift (minimum voltage)

Figure 3.27 Streamlines and pressure contours with 1 kV actuation, and compensated pressure distribution under feedback control (Re = 1000, AR = ∞, α = 15°, T^* = 100, α_d = 0.06, $V_{app,0}$ = 1 kV, x_{act}/c = 0.2).

Since the jet induced by the actuator is almost horizontal and the viscous force augmented by the actuation hardly contributes to lift as a result, the variation in pressure distribution mostly contributes to the lift variation. Although the closed-loop voltage variation is not large enough to resize the separated flow structure, the relative pressure distributions suggest the lift stabilization mechanism. At the instant of minimum lift, the controller increases the actuation voltage, intensifying the suction pressure near the leading edge as shown in Figure 3.27(a). Though the pressure distributions downstream of the actuator and downside of the wing are hardly changed, the net pressure change

near the leading edge and the actuator contributes to enhancing lift. When the disturbance causes maximum lift, on the other hand, the controller decreases the voltage, reducing suction and pressure peaks as shown in Figure 3.27(b) to mitigate the lift increase.

The control performances for different wing aspect ratios are compared in Figure 3.28. Compared to the infinite wing, higher voltage variation is required for the finite wing, implying that the control authority on lift is decreased. Even with the same disturbance, there are phase differences in force responses between infinite and finite wings, and drag fluctuation is increased by stabilizing lift for the finite wing, as opposed to the reduced drag fluctuation for the infinite wing. It is observed that the control authority on lift decreases and penalty for drag increases, as the wing aspect ratio decreases.

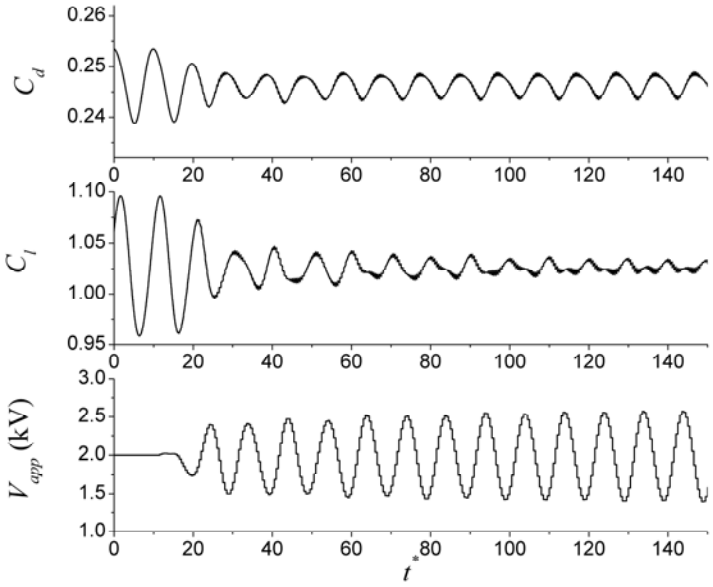

(a) $AR = \infty$

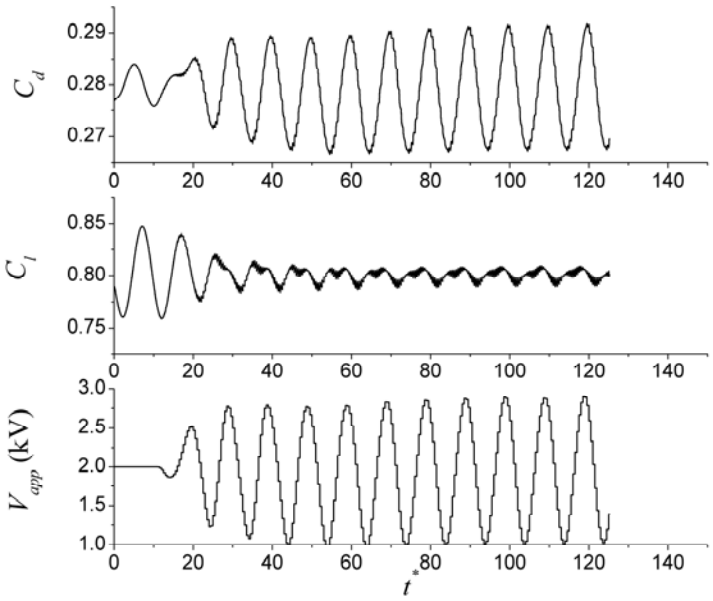

(b) $AR = 4$

Figure 3.28 Disturbance rejection of lift; drag coefficient, lift coefficient and applied voltage (Re = 1000, α = 15°, T^* = 10, α_d = 0.05, $V_{app,0}$ = 2 kV, learning rate = 300, n_c = 50, 3 system parameters capturing 1 NMP zero and delay).

3.5.3 Simultaneous stabilization of lift and drag

The observations in Figure 3.28 indicate that controlling lift can be either beneficial or detrimental to drag depending on wing aspect ratio. Although the drag fluctuation is not included in the performance, it would be advantageous in practice to be able to stabilize both lift and drag. In order to understand the impact of wing aspect ratio on the drag fluctuation, the time evolutions of pressure and viscous drags for the case of Figure 3.28(b) are shown in Figure 3.29, along with pressure and wall-shear stress distributions on the upper surface of the wing. For the two time instants with lower and higher voltage levels, denoted by A and B, respectively, both pressure and friction drags alternate their maximum and minimum values. With the lower voltage, the viscous drag decreases, while the pressure drag increases. With the higher voltage, on the other hand, the opposite occurs. Since the variation amplitudes of viscous and pressure drag evolutions are different, the total drag accompanies the steady-state fluctuation, as mentioned in the previous section.

The impact of wing aspect ratio can be addressed based on the pressure and friction force distributions on the wing. Due to the dominant 3-dimensional effect near the wing tip, the pressure distribution near the wing tip exhibits the loss of the enhanced suction peak, which is more noticeable for B. On the other hand, the friction force peaks distributing along the span are more influential near the wing tip. Moreover, higher voltage in B increases this effect. As a result, the finite wing with $AR = 4$, compared to the infinite wing, has reduced impact of the DBD actuation on the pressure force and increased impact of the actuation on the friction force, resulting in amplified drag fluctuation with feedback control.

Since various factors can affect the unsteady force evolutions the trend is subject to other flow conditions, such as Reynolds number, actuation location and disturbance frequency.

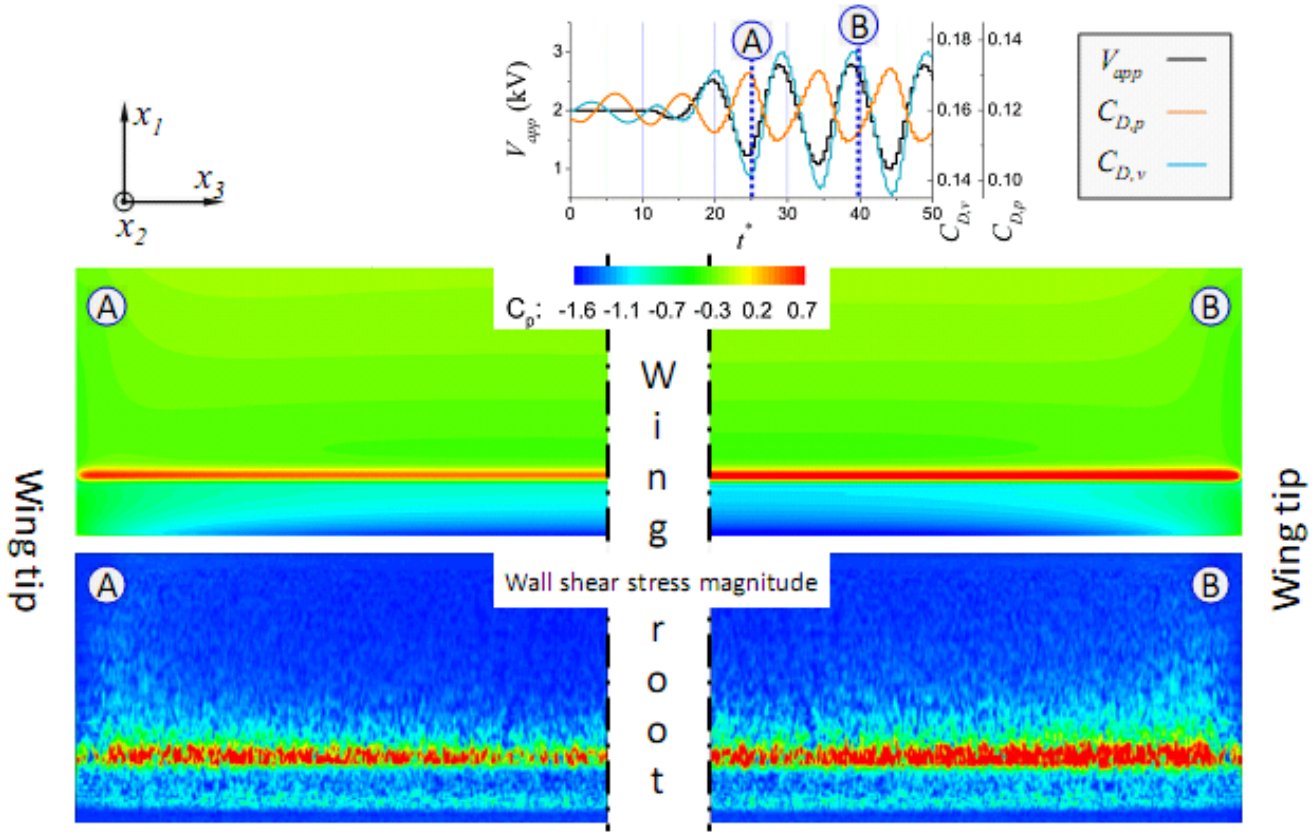

Figure 3.29 Pressure and viscous drag evolutions during feedback control: same case as Figure 3.28(b).

3.6 Summary of the chapter

For Reynolds numbers between 300 and 1000, the flow over the wing with the SD7003 airfoil geometry at the angle of attack of 15 degrees is controlled using the DBD actuator. The impacts of the open-loop DBD actuation on aerodynamic forces originate from: 1) pressure and suction peaks near the actuator; 2) pressure recovery in the wake due to reduced flow-separation; and 3) the additional friction force caused by the induced flow. Moreover, the impacts of the selected parameters on actuation performance are summarized in the following.

Actuation voltage

Higher voltage results in higher lift increase and more decrease of pressure drag, whereas total drag increases with voltage. The sensitivity of voltage on aerodynamic forces is noticeable for the lower voltage region especially $V_{app} \leq 1$ kV where the separated-flow region exists, and the impact declines as the flow attaches. The trend is also sensitive to Reynolds number and wing aspect ratio, i.e., higher *Re* and larger *AR* result in the favorable impacts of the DBD actuation on the aerodynamic forces.

Wing aspect ratio

Although the actuator is invariant along the spanwise direction, the DBD actuation intensifies the 3D effect of the flow field. For the infinite wing at *Re* = 1000, the DBD actuation can enhance lift and reduce drag simultaneously.

Reynolds number

For *Re* = 300, the DBD actuation can eliminate the flow separation but cannot decrease the velocity deficit in the wake region. For *Re* = 1000, on the other hand, the actuation shrinks the wake region, resulting in more favorable impacts on aerodynamic forces.

Actuation location

More downstream actuation benefits the lift enhancement, but at the cost of drag increase.

For the feedback control of the lift fluctuation under the influence of the free-stream unsteadiness, the retrospective cost adaptive control algorithm is adopted. The control law updates controller gains by minimizing the retrospective cost function with the information of system parameters, namely the first nonzero Markov parameter and NMP zeros of the linearized transfer function of the flow-actuator system. In order to estimate those parameters, the Markov parameter polynomial, whose coefficients consist of Markov parameters, is used.

Multiple identification techniques are applied to estimate the system parameters. For a stable nominal state, the impulse response of the flow-actuator system provides Markov parameters directly. The RLS algorithm can be applied to estimate the parameters recursively, implying its potential as an online identification tool. In addition, the recursive input signal can be used to estimate the real NMP zero more efficiently.

The identified system parameters indicate that the linearized transfer function of the flow-actuator system has one real NMP zero from voltage to lift, whereas it has no real NMP zero (or no NMP zero in many cases) from voltage to drag. The existence of the real NMP zero for lift is consistent with the fact that the step response of lift has initial undershoot, which is the property of a nonminimum-phase system with a real NMP zero.

Among the three impacts of the DBD actuation on aerodynamic forces, the pressure and suction peaks around the actuator mainly contribute to the disturbance rejection in lift. The performance of feedback lift control is explored further for different wing aspect ratios, and for disturbance amplitude and frequency. Lift fluctuations with free-stream unsteadiness under 10 % can be stabilized by the control system. On the other hand, the drag fluctuations, while not intended, can be suppressed at the same time when the disturbance amplitude and period are small, especially for the infinite wing. Moreover, the difference in response time between the pressure variations and augmented friction forces due to the actuation determines the feasibility of simultaneous stabilization of lift and drag. As a result, the feasibility of reducing lift and drag fluctuations simultaneously is also dependent on the disturbance conditions.

The real NMP zero and first nonzero Markov parameter are subject to geometric, flow and actuation conditions, as well as the control time resolution: The more upstream actuation, lower wing aspect ratio and lower Reynolds number, the smaller the NMP zero. The lower vertical free-stream speed and smaller voltage variation induces the smaller NMP zero. The higher vertical free-stream speed, Reynolds number and voltage increment results in the larger absolute value of the first nonzero Markov parameter. The higher sampling rate decreases the magnitude of NMP zeros.

The drift of system parameters depending on the flow and actuation conditions indicates the degree of nonlinearities of the system. As a result, control performance, such as attainable bounds of controlled variables and controllable disturbance level, is limited. For the infinite wing, disturbance magnitudes up to 15 % can be suppressed, but with unfavorable transient responses. For finite wings, disturbances less than 8 % are manageable.

The selected parameters, their conditions and key observations are summarized in Table 3.1 and Table 3.2.

Table 3.1 Summary of the impact of flow and actuator conditions.

Conditions	Reynolds number: $Re = 300 \sim 1000$	Aspect ratio: $AR = 4, 8, \infty$	Actuation location: $x_{act}/c = 0.05 \sim 0.7$
Order or the linearized transfer function	3~6 (delay is 1).		
First nonzero Markov parameter(H_1) and real NMP zero(z_{NMP}) for lift	$\|H_1\|$ and z_{NMP} increase as Re increases.	z_{NMP} increases as AR increases.	z_{NMP} increases as actuation location moves downstream.
Steady-state aerodynamic forces	Control authority on lift grows as Re increases. Penalty on drag decays as Re increases.	Control authority on lift grows as AR increases. Penalty on drag decays as AR increases.	Control authority on lift grows as actuation moves to downstream. Drag increase: no clear trend for $Re = 300$.
Dynamic aerodynamic force: lift	For higher Re, undershoot is larger but the steady-state lift increase is more substantial, resulting in decrease of the relative undershoot.	The relative undershoot decreases as the actuator moves downstream and AR increases.	
Feedback performance	At a higher Reynolds number both lift and drag fluctuations can be suppressed at certain disturbance frequencies.	Controllable disturbance magnitudes are limited by the reduced control authority for a lower AR.	Only for 0.2.

Table 3.2 Summary of the impact of operation conditions.

Conditions	Nominal voltage: $V_{app,0}$ = 1 and 2 kV	Impulse or step amplitude: ΔV_{app} = 0.1 ~ 5 kV	Control time resolution: Δt_c^* = 0.1 and 0.5
Order or the linearized transfer function	3~6 (delay is 1).		For Δt_c^* = 0.1, system order is 10 (delay is 1).
First nonzero Markov parameter(H_1) and real NMP zero(z_{NMP}) for lift	Not sensitive.	$\lvert H_1 \rvert$ and z_{NMP} increase as step amplitude increases. Asymmetry in amplitude sign.	z_{NMP} decreases as time resolution increases.
Steady-state aerodynamic forces	Lift mostly increases with the actuation. For $AR = \infty$ at Re = 1000, drag decreases with V_{app} = 1 kV; For others, the actuation results in the increase of drag.	Not relevant	
Dynamic aerodynamic force: lift	Not sensitive.	Steady-state lift increases faster than undershoot as step amplitude increases, resulting in smaller relative undershoot.	For higher time resolution, undershoot is larger, NMP zero is smaller.
Feedback performance	Not sensitive but the lower voltage bound is limited by the breakdown voltage.	The NMP zero drift can limit the disturbance magnitude that can be suppressed.	Higher time resolution incorporates NMP zeros close to the unit circle. Lower time resolution causes higher steady-state error due to unresolved fluctuations.

CHAPTER 4
SUMMARY AND CONCLUSION

4.1 Outcome and findings

4.1.1 Surrogate modeling and DBD actuator

The performance of the DBD actuator, namely force generation and power consumption, is sensitive to the operational, geometry and material parameters of the actuator. Specifically, these parameters can, in certain combinations, facilitate the asymmetry between two half-cycles by affecting the discharge-limiting process, thereby enhancing the time-averaged force generation.

In order to aid systematic parametric-study and design guidelines, surrogate-based modeling is introduced. Multiple surrogate models are trained to approximate the first-principle-based simulations of the DBD actuator. Two operation parameters – the discharge frequency and the polarity time ratio of the applied voltage – and one material parameter – dielectric constant – are chosen as design variables. In order to achieve reasonable accuracy while reducing the computation cost, multiple levels of design space refinement are devised. Surrogate models at each level differ in fitting the original data and the weighted average surrogate provides good accuracy for this application. Although the surrogate models at the initial level are not accurate enough, they consistently supply beneficial information for the further refinement of the design space. The non-polyhedral design-space-constraints generated by the initial level surrogate models provide efficient design of experiments for the refined regions, resulting in higher accuracy in the regions of interest.

The surrogates at different levels consistently show that two branches of the Pareto front exist with different orientations of the average force. As sets of possible optimal operation, the parametric combinations along the Pareto front elucidate the mechanism of enhancing force generation, which is to increase the asymmetry between the first- and second-half cycles. Moreover, each front branch is found to be in one of two regions far apart from the others in the original design space. For the two regions, namely high- and low-power regions, parametric sensitivities differ significantly. Specifically, the dielectric constant is always influential, but the importance of the frequency and polarity time ratio alternates depending on the power capability.

Surrogate modeling can also provide reduced-order DBD actuator models, which link first-principle-based DBD simulations and induced flow simulations with a complex geometry and different time-scale. In the process of flow-control-system design, it is critical to assess the parametric impacts of actuator operation on control authority and to apply the understanding to the optimization of the control system.

4.1.2 Adaptive control of the flow-actuator system

In this flow-control study, unsteady aerodynamic forces on the finite or infinite wing with the SD7003 airfoil geometry under the influence of time-varying free-stream velocity are controlled with the DBD actuator. At Reynolds numbers between 300 and 1000 and at an angle-of-attack of 15 degrees, the wake instability can be prevented by open-loop actuation. On the other hand, the force fluctuations induced by the moderate free-stream unsteadiness can be stabilized by feedback control. The retrospective cost adaptive control algorithm based on the parameter estimates of the flow-actuator system provides the control voltage that minimizes lift deviation from the undisturbed lift.

For the system information required by the controller, the first nonzero Markov parameter and NMP zero of the flow-actuator system's linearized transfer function are estimated using the Markov parameter polynomial whose coefficients are the impulse response of the system. In most cases, the linearized system model is nonminimum-phase for lift with a real NMP zero and shows undershoot in response to voltage increase. On the other hand, no real NMP zero exists for drag.

The open-loop actuation increases the steady-state lift by intensifying the suction peak and by recovering the pressure loss in the separated-flow region with the penalty of the increased friction drag. However, depending on the disturbance condition, the closed-loop actuation can be favorable to both lift and drag by suppressing the fluctuations of lift and drag simultaneously. The regulated time-varying pressure field, especially intensified pressure and suction peaks around the DBD actuator, is shown as the main disturbance rejection mechanism. Since the impact of the actuation on lift can be attributed to different sources with different time evolutions, the simultaneous attenuations of lift and drag fluctuations are dependent on the flow and actuation conditions, especially time scale of the disturbance.

For modest free-stream fluctuations, constant estimates of the first nonzero Markov parameter and real NMP zero are sufficient for the adaptive controller to stabilize the lift fluctuation. Those system parameters, however, are functions of flow and actuation conditions due to the nonlinearities of the system. The variable system parameters can limit the control performance especially under severe disturbance conditions, implying that the trends can be used to optimize geometric and operational conditions of the DBD actuator to enhance control performance.

4.2 Contributions

One of the key challenges in the application of the DBD actuator is to enhance its control authority with less power. The application of surrogate modeling techniques establishes an efficient design process in the flow control exercise, whose performance requirements span multiple operation points. In this study, various parametric influences on the actuation performance are explored to aid in the design process. The computational cost of simulating multi-scale plasma dynamics in the DBD actuation prohibits in-depth survey of the design space. The multiple surrogate models employed in this study not only provide reliable performance estimates with a significant design-cost reduction, but also portray the design space, clarifying the region of interest for further design-space refinement. The high- and low-power regions separated by the design space accompany disparities in modeling parameters such as force orientations, parametric sensitivities and

achievable optimal conditions. Multiple branches of the Pareto front suggest the possibility of flexible applicability to meet various performance requirements.

On the other hand, surrogate models can bridge the detailed discharge simulation and airflow simulation with complex geometries, providing modeling guidelines. The surrogate-based body-force model offers potential for capturing more realistic flow physics under the influence of actuator parameters than the bilinear body-force model.

The open-loop control results provide insight into the impacts of DBD actuation on the low-Reynolds-number aerodynamics around a rectangular wing for various flow and actuator conditions. In order to design the flow-actuator system with sufficient control authority, it is important to understand the trend of actuation-performance relations.

This feedback control study, which is based on the adaptive control law using the flow-actuator system's Markov parameters, provides a prospective flow control framework. The information required by the controller is incorporated into compact system parameters, which are easy to identify, suggesting further extension to online identification in order to accommodate various flow regimes and inherent nonlinearities of the system. The applied identification methods and closed-loop flow control based on the retrospective cost adaptive algorithm prove the capability and validity of the current approach. Moreover, combined with the DBD actuator, the control system successfully alleviates the moderate flow unsteadiness, proposing an effective control scheme for low-Reynolds number aerodynamics.

Another goal of this study is to understand the interaction between unsteady actuation and aerodynamic performances – i.e., lift and drag of a wing – and the underlying physics. Since the controller outputs the actuation voltage appropriate for achieving the objective, namely minimizing the influence of free-stream disturbances, the resultant actuation and flow information can aid in understanding the control mechanisms suppressing lift fluctuation, which are valuable in designing a low-Reynolds number flyer. In this study, the mechanism of lift stabilization, impacts on the uncontrolled drag and feasibility of simultaneous suppression of lift and drag fluctuations are explicitly addressed for different flow and actuation conditions. In addition, the identified system parameters –

first nonzero Markov parameter and NMP zero – are related to the flow response to DBD actuation, and the impacts of flow and actuation conditions on these parameters are assessed. Furthermore, it is shown that different flow and actuation conditions cause the variations of parameter estimate, namely, parametric drift, which influences control performance and can restrict achievable performances. As a result, the parametric combinations – wing aspect ratio, actuation location, control time resolution – that are favorable to achieving control objective can be deduced for the purpose of enhancing control authority of the DBD actuator and improving control performance.

On the other hand, the limitations of the linearized-modeling approach are also highlighted by the parametric drifts, which indicate the nonlinearities of the flow-actuator system with respect to the conditional parameters as well as the actuation itself. The controller with constant system parameters identified at one operation point shows restrictions in the controllable disturbance magnitude and achievable steady-state performance variation. As a result, substantial free stream fluctuations cannot be controlled properly, and the manageable disturbance magnitude remains less than 10 % of the vertical free stream speed.

4.3 Future work

In order to explore the plasma physics in the DBD actuation, 2-species helium chemistry is adopted with the fluid modeling approach. Although the fundamental mechanisms of actuator operation can be captured with the relatively simple model, the application of air chemistry with more ionized-species, especially negative ions, can improve the fidelity of the analysis. The limitations in the actuator geometry and computational domain size due to computational cost can be alleviated by introducing the capability of parallel computation to the DBD simulation.

The surrogate-based modeling approach offers the parametric investigation for three operation and material variables – applied voltage frequency, insulator dielectric constant and polarity time ratio of the voltage waveform. However, the force generation and power consumption are also affected by other parameters such as electrode size, insulator thickness, and amplitude of operation-voltage waveform, which are invariant in this study.

More design variables mean an increase in dimensionality, resulting in an exponential increase in sampling points. In such a case, additional surrogate techniques such as design space splitting and dimensionality reduction based on the global sensitivity indices can accelerate the design process.

Although some surrogates offer good approximations of force fields, the actuator conditions, such as material and operational parameters, should be incorporated with the spatial design variables in order to utilize these surrogates as a powerful design tool. More considerations are necessary to efficiently combine into a single data set the actuator parameters and spatial coordinates, which have very different sampling densities. Furthermore, in order to extend the simulation capability based on first-principle-models for more consistent geometry and operation conditions, further improvement of the 2-species fluid plasma model is required, especially in the number of species in the chemistry and computational efficiency.

In the feedback flow control, a single-input and single-output model is used for the flow-actuator system. Instead, more general multiple-input and multiple-output models can be adopted for the controller and the flow-actuator system. Although the extended model implementations are not extraordinarily laborious, the choice of measurements and actuators may require an extensive investigation. In addition, more realistic exercises can be simulated by adding noise models to the control system.

The Reynolds numbers between 300 and 1000 adopted in this study are sufficiently low to incorporate laminar flow throughout the entire domain. For higher Reynolds numbers of $O(10^4 \sim 10^5)$, turbulence effects as well as transition-to-turbulence need to be considered. Moreover, since the increased Reynolds number accompanies higher nonlinearity and decreased control authority, the problem becomes more complicated.

Finally, as shown in the feedback control examples, higher disturbance magnitude deteriorates control performance. The information about parametric drifts associated with flow and actuation conditions can provide a mapping from these conditions to the system parameters, resulting in variable parameter estimates. Some preliminary studies incorporating parametric mapping based on flow-velocity measurement with the adaptive

controller show an improvement in reducing lift fluctuation under high disturbance conditions.

REFERENCES

[1]Shyy, W., Lian, Y., Tang, J., Viieru, D., and Liu, H., *Aerodynamics of Low Reynolds Number Flyers*, New York, Cambridge Univ. Press, 2008.

[2]Mueller, T. J., and DeLaurier, J. D., "Aerodynamics of small vehicles," *Ann. Rev. Fluid Mech.*, Vol. 35, 2003, pp. 89-111.

[3]Lissaman, P. B. S., "Low-Reynolds-number airfoils," *Ann. Rev. Fluid Mech.*, Vol. 15, 1983, pp. 223-239.

[4]Shyy, W., Berg, M., and Ljungqvist, D., "Flapping and flexible wings for biological and micro air vehicles," *Prog. Aero. Sci.*, Vol. 35, 1999, pp. 455-505.

[5]Choi, H., Jeon, W.-P., and Kim, J., "Control of flow over a bluff body," *Annu. Rev. Fluid Mech.*, Vol. 40, 2008, pp. 113-139.

[6]Becker, R., King, R., Petz, R., and Nitsche, W., "Adaptive closed-loop separation control on a high-lift configuration using extremum seeking," *AIAA Journal*, Vol. 45, No. 6, 2007, pp. 1382-1392.

[7]Gad-el-Hak, M., *Flow Control: Passive, Active and Reactive Flow Management*, New York, Cambridge University Press, 2000.

[8]Chang, P. K., *Control of Flow Separation: Energy Conservation, Operational Efficiency, and Safety*, New York, Hemisphere Publishing Corp., 1976.

[9]Joslin, R. D., and Miller, D. N., *Fundamentals and Applications of Modern Flow Control*, Reston, Progress in Astronautics and aeronautics, 2009.

[10]Lachmann, G. V., *Boundary Layer and Flow Control*, New York, Pergamon Press, 1961.

[11]Greenblatt, D., Goksel, B., Rechenberg, I., Schule, C. Y., Romann, D., and Paschereit, C. O., "Dielectric barrier discharge flow control at very low flight Reynolds numbers," *AIAA Journal*, Vol. 46, No. 6, 2008, pp. 1528-1540.

[12]Moreau, E., "Airflow control by non-thermal plasma actuators," *J. Phys. D: Appl. Phys.*, Vol. 40, 2007, pp. 605-636.

[13]Braun, E. M., Lu, F. K., and Wilson, D. R., "A critical review of electric and electromagnetic flow control research applied to aerodynamics," *39th Plasmadynamics and Lasers Conference*, Seattle, Washington, 23-26 June, 2008, AIAA 2008-3788.

[14]Enloe, C. L., McLaughlin, T. E., VanDyken, R. D., Kachner, K. D., Jumper, E. J., Corke, T. C., Post, M., and Haddad, O., "Mechanisms and responses of a single dielectric barrier plasma actuator: geometric effects," *AIAA Journal*, Vol. 42, No. 3, 2004, pp. 595-604.

[15]Jukes, T. N., Choi, K.-S., Johnson, G. A., and Scott, S. J., "Characterization of Surface Plasma-Induced Wall Flows Through Velocity and Temperature Measurements," *AIAA Journal*, Vol. 44, No. 4, 2006, pp. 764-771.

[16]Wang, Q.-M., Du, X.-H., Xu, B., and Cross, L. E., "Electromechanical coupling and output efficiency of piezoelectric bending actuators," *IEEE Transactions on Ultrasonics, Ferroelectrics, and Frequency Control*, Vol. 46, No. 3, 1999, pp. 638-646.

[17]Kogelschatz, U., Eliasson, B., and Egli, W., "Dielectric-barrier discharges: principle and applications," *Journal De Physique IV*, Vol. 7, C4, 1997, pp. 47-66.

[18]Caraballo, E., Kasnakoglu, C., Serrani, A., and Samimy, M., "Control input separation methods for reduced-order model-based feedback flow control," *AIAA Journal*, Vol. 46, No. 9, 2008, pp. 2306-2322.

[19]Chan, S., Zhang, X., and Gabriel, S., "Attenuation of low-speed flow-induced cavity tones using plasma actuators," *AIAA Journal*, Vol. 45, No. 7, 2007, pp. 1525-1538.

[20]Huang, X., Chan, S., Zhang, X., and Gabriel, S., "Variable structure model for flow-induced tonal noise control with plasma actuators," *AIAA Journal*, Vol. 46, No. 1, 2008, pp. 241-250.

[21]Asghar, A., and Jumper, E. J., "Phase synchronization of vortex shedding from two circular cylinders using plasma actuators," *AIAA Journal*, Vol. 47, No. 7, 2009, pp. 1608-1616.

[22]Benard, N., Braud, P., Jolibois, J., and Moreau, E., "Airflow reattachment along a NACA 0015 airfoil by surface dielectric barrier discharge actuator - time resolved particle image velocimetry investigation," *4th Flow Control Conference*, Seattle, Washington, 23-26 June, 2008, AIAA 2008-4202.

[23]Benard, N., Bonner, J. P., Touchard, G., and Moreau, E., "Flow control by dielectric barrier discharge actuators - jet mixing enhancement," *4th Flow Control Conference*, Seattle, Washington, 23-26 June, 2008, AIAA 2008-3878.

[24]Patel, M. P., Sowle, Z. H., Corke, T. C., and He, C., "Autonomous sensing and control of wing stall using a smart plasma slat," *44th AIAA Aerospace Sciences Meeting and Exhibit*, Reno, Nevada, 9-12 January, 2006, AIAA 2006-1207.

[25]Lopera, J., Ng, T. T., Patel, M. P., and Vasudevan, S., "Aerodynamic control of 1303 UAV using windward surface plasma actuators on a separation ramp," *45th AIAA Aerospace Sciences Meeting and Exhibit*, Reno, Nevada, 8-11 Janusary, 2007, AIAA 2007-636.

[26]Grundmann, S., and Tropea, C., "Experimental damping of boundary-layer oscillations using DBD plasma actuators," *International Journal of Heat and Fluid Flow*, Vol. 30, 2009, pp. 394-402.

[27]Kim, J.-H., Nishihara, M., Keshav, S., Adamovich, I. V., Samimy, M., Gorbatov, S. V., and Pliavaka, F. V., "On the development of localized arc filament plasma actuators for high-speed flow control," *40th Plasmadynamics and Lasers Conference*, San Antonio, Texas, 2009, AIAA 2009-4071.

[28]Visbal, M. R., Gaitonde, D. V., and Roy, S., "Control of transitional and turbulent flows using plasma-based actuators," *36th AIAA Fluid Dynamics Conference and Exhibit*, San Francisco, CA, 5-8 June, 2006, AIAA 2006-3230.

[29]Jayaraman, B., Lian, Y., and Shyy, W., "Low-Reynolds number flow control using dielectric barrier discharge actuators," *37th AIAA Fluid Dynamics Conference and Exhibit*, Miami, FL, 25-28 June, 2007, AIAA 2007-3974.

[30]Poggie, J., "Plasma-based control of shock-wave/boundary-layer interaction," *44th AIAA Aerospace Sciences Meeting and Exhibit*, Reno, Nevada, 9-12 January, 2006, AIAA 2006-1007.

[31]Rizzetta, D. P., and Visbal, M. R., "Large-eddy simulation of plasma-based control strategies for bluff body flow," *4th Flow Control Conference*, Seattle, Washington, 23-26 June, 2008, AIAA 2008-4197.

[32]He, C., Corke, T. C., and Patel, M. P., "Numerical and experimental analysis of plasma flow control over a hump model," *45th AIAA Aerospace Sciences Meeting and Exhibit*, Reno, Nevada, 8-11 January, 2007, AIAA 2007-935.

[33]McDaniel, E. W., *Collision Phenomena in Ionized Gases*, New York, John Wiley & Sons, Inc., 1964.

[34]Mitchner, M., and Charles H Kruger, J., *Partially Ionized Gases*, New York, John Wiley & Sons, Inc., 1973.

[35]Unfer, T., Boeuf, J. P., Rogier, F., and Thivet, F., "Modeling of dielectric barrier discharge and coupling with computational fluid dynamics," *46th AIAA Aerospace Sciences Meeting and Exhibit*, Reno, NV, 7-10 January, 2008, AIAA 2008-1375.

[36]Roth, J. R., Sherman, D. M., and Wilkinson, S. P., "Boundary Layer Flow Control with a One Atmosphere Uniform Glow Discharge Surface Plasma," *AIAA Journal*, Vol. AIAA 98-0328, 1998.

[37]Shyy, W., Jayaraman, B., and Andersson, A., "Modeling of glow discharge-induced fluid dynamics," *J. Appl. Phys.*, Vol. 92, No. 11, 2002, pp. 6434-6443.

[38]Jayaraman, B., and Shyy, W., "Modeling of dielectric barrier discharge-induced fluid dynamics and heat transfer," *Prog. Aero. Sci.*, 2007.

[39]Enloe, C. L., McLaughlin, T. E., VanDyken, R. D., Kachner, K. D., Jumper, E. J., and Corke, T. C., "Mechanisms and Responses of a Single Dielectric Barrier Plasma Actuator: Plasma Morphology," *AIAA Journal*, Vol. 42, No. 3, 2004, pp. 589-594.

[40]Gherardi, N., and Massines, F., "Mechanisms controlling the transition from glow silent dischrage to streamer discharge in nitrogen," *IEEE Transactions on Plasma Science*, Vol. 29, No. 3, 2001, pp. 536-544.

[41]Roth, J. R., *Industrial Plasma Engineering Volume 2: applications to nonthermal plasma processing*, London, IOP Publishing, 2001.

[42]Yuan, X., Shin, J., and Raja, L. L., "One-dimensional simulation of multi pulse phenomena in dielectric-barrier atmospheric-pressure glow discharges," *Vacuum*, Vol. 80, 2006, pp. 1199-1205.

[43]Font, G. I., Enloe, C. L., McLaughlin, T. E., and Orlov, D., "Plasma discharge characteristics and experimentally determined boundary conditions for a plasma actuator," *45th AIAA Aerospace Sciences Meeting and Exhibit*, Reno, Nevada, 8-11 January, 2007, AIAA 2007-188.

[44]Likhanskii, A. V., Shneider, M. N., Macheret, S. O., and Miles, R. B., "Optimization of dielectric barrier discharge plasma actuators driven by repetitive nanosecond pulses," *45th AIAA Aerospace Sciences Meeting and Exhibit*, Reno, Nevada, 8-11 January 2007, 2007.

[45]Roy, S., Singh, K. P., and Gaitonde, D. V., "Air plasma actuators for effective flow control," *45th AIAA Aerospace Sciences Meeting and Exhibit*, Reno, Nevada, 8-11 January 2007, 2007.

[46]Porter, C. O., McLaughlin, T. E., Enloe, C. L., Font, G. I., Roney, J., and Baughn, J. W., "Boundary Layer Control Using a DBD Plasma Actuator," *45th AIAA Aerospace Sciences Meeting and Exhibit*, Reno, NV, Jan 8-11, 2007.

[47]Forte, M., Jolibois, J., Moreau, E., Touchard, G., and Cazalens, M., "Optimization of a dielectric barrier discharge actuator by stationary and non-stationary measurements of the induced flow velocity - application to airflow control," *3rd AIAA Flow Control Conference*, San Francisco, CA, 5-8 June, 2006, AIAA 2006-2863.

[48]Abe, T., Takizawa, Y., Sato, S., and Kimura, N., "A parametric experimental study for momentum transfer by plasma actuator," *45th AIAA Aerospace Sciences Meeting and Exhibit*, Reno, NV, 8-11 January, 2007, AIAA 2007-187.

[49]Roth, J. R., and Dai, X., "Optimization of the aerodynamic plasma actuator as an electrohydrodynamic (EHD) electrical device," *44th AIAA Aerospace Sciences Meeting and Exhibit*, Reno, NV, 9-12 January, 2006, AIAA 2006-1203.

[50]Gregory, J. W., Enloe, C. L., Font, G. I., and McLaughlin, T. E., "Force Production Mechanisms of a Dielectric-Barrier Discharge Plasma Actuator," *45th AIAA Aerospace Sciences Meeting and Exhibit*, Reno, NV, Jan 8-11, 2007.

[51]Hall, K. D., Jumper, E. J., Corke, T. C., and McLaughlin, T. E., "Potential flow model of a plasma actuator as a lift enhancement device," *43rd AIAA Aerospace Sciences Meeting and Exhibit*, Reno, Nevada, 10-13 January, 2005, AIAA 2005-783.

[52]Suzen, Y. B., Huang, P. G., Jacob, J. D., and Ashpis, D. E., "Numerical simulations of plasma based flow control applications," *35th AIAA Fluid Dynamics Conference and Exhibit*, Toronto, Canada, 6-9 June, 2005, AIAA 2005-4633.

[53]Orlov, D. M., Corke, T. C., and Patel, M. P., "Electric circuit model for aerodynamic plasma," *44th AIAA Aerospace Sciences Meeting and Exhibit*, Reno, Nevada, 9-12 January, 2006, AIAA 2006-1206.

[54]Queipo, N. V., Haftka, R. T., Shyy, W., Goel, T., Vaidyanathan, R., and Tucker, P. K., "Surrogate-based analysis and optimization," *Progress in Aerospace Sciences*, Vol. 41, 2005, pp. 1-28.

[55]Mack, Y., Goel, T., Shyy, W., Haftka, R. T., and Queipo, N., "Multiple surrogate for the shape optimization of bluff body-facilitated mixing," *43rd AIAA Aerospace Sciences Meeting and Exhibit*, Reno, Nevada, 10-13 January, 2005, AIAA 2005-333.

[56]Goel, T., Zhao, J., Tharkur, S., Haftka, R. T., and Shyy, W., "Surrogate model-based strategy for cryogenic cavitation model valication and sensitivity evaluation," *AUAA/ASME/SAE/ASEE Joint Propulsion Conference & Exhibit*, Sacramento, CA, 9-12 July, 2006, AIAA 2006-5047.

[57]Box, G. E. P., Hunter, J. S., and Hunter, W. G., *Statistics for Experimenters*, 2nd ed., New York, John Wiley & Sons, Inc., 2005.

[58]Myers, R. H., and Montgomery, D. C., *Response Surface Methodology: Progress and Product Optimization Using Designed Experiments*, 2nd ed., New York, John Wiley & Sons, Inc., 2002.

[59]Sacks, J., Welch, W. J., Mitchell, T. J., and Wynn, H. P., "Design and analysis of computer experiments," *Statistical Science*, Vol. 4, No. 4, 1989, pp. 409-435.

[60]Lophaven, S. N., Nielsen, H. B., and Sondergaard, J., "DACE - A Matlab Kriging Toolbox," *Technical Report IMM-TR-2002-12*, Informatics and Mathematical Modelling, Technical University of Denmark, 2002.

[61]Cheng, B., and Titterington, D. M., "Neural networks: a review from a statistical perspective," *Statistical Science*, Vol. 9, No. 1, 1994, pp. 2-54.

[62]Goel, T., Haftka, R. T., Queipo, N., and Shyy, W., "Performance estimate and simultaneous application of multiple surrogates," *11th AIAA/ISSMO Multidisciplinary Analysis and Optimization Conference*, Portsmouth, VA, 6-8 September, 2006, AIAA 2006-7047.

[63]Viana, F. A. C., Haftka, R. T., and Steffen, V. J., "Multiple surrogates: how cross-validation errors can help us to obtain the best predictor," *Structural and multidisciplinary Optimization*, Vol. 39, No. 4, 2009, pp. 439-457.

[64]Viana, F. A. C., and Haftka, R. T., "Using multiple surrogates for metamodeling," *7th ASMO-UK/ISSMO International Conference on Engineering Design Optimization*, Bath, UK, 7-8 July, 2008.

[65]Sobol, I., "Sensitivity analysis for nonlinear mathematical models," *Mathematical Modeling & Computational Experiment*, Vol. 1, No. 4, 1993, pp. 407-414.

[66]Miettinen, K. M., *Nonlinear Multiobjective Optimization*, Boston, Kluwer Academic Publishers, 1999.

[67]Moin, P., and Bewley, T., "Feedback control of turbulence," *Appl. Mech. Rev.*, Vol. 47, No. 6, 1994, pp. S3-S13.

[68]Baker, J., Armaou, A., and Christofides, P. D., "Nonlinear control of incompressible fluid flow: application to Burgers' equation and 2D channel flow," *J. Math. Anal. Appl.*, Vol. 252, 2000, pp. 230-255.

[69]Fagley, C. P., Balas, M. J., Siegel, S., Seidel, J., and McLaughlin, T., "Reduced order mkodel of cylinder wake with direct adaptive feedback control," *AIAA Guidance, Navigation, and Control Conference*, Chicago, Illinois, 10-13 August, 2009, AIAA 2009-5856.

[70]Holmes, P., Lumley, J. L., and Berkooz, G., *Turbulence, Coherent Structures, Dynamical Systems and Symmetry*, New York, Cambridge University Press, 1996.

[71]Ahuja, S., and Rowley, C. W., "Low-dimensional models for feedback stabilization of unstable steady states," *46th AIAA Aerospace Sciences Meeting and Exhibit*, Reno, NV, 7-10 January, 2008, AIAA 2008-553.

[72]Gunzburger, M., "Adjoint equation-based methods for control problems in incompressible, viscous flows," *Flow, Turbulence and Combustion*, Vol. 65, 2000, pp. 249-272.

[73]Kutay, A. T., Culp, J. R., Muse, J. A., Brzozowski, D. P., Glezer, A., and Calise, A. J., "A closed-loop flight control experiment using active flow control actuators," *45th AIAA Aerospace Sciences Meeting and Exhibit*, Reno, Nevada, 8-11 January, 2007, AIAA 2007-114.

[74]Muse, J. A., Tchieu, A. A., Kutay, A. T., Chandramohan, R., Calise, A. J., and Leonard, A., "Vortex model based adaptive flight control using synthetic jets," *AIAA Guidance, Navigation, and Control Conference*, Chicago, IL, 10-13 August, 2009, AIAA 2009-5761.

[75]Pindera, M. Z., "Adaptive flow control using simple artificial neural networks," *40th AIAA Aerospace Sciences Meeting & Exhibit*, Reno, Nevada, 14-17 January, 2002, AIAA 2002-0990.

[76]Deb, D., Tao, G., Burkholder, J. O., and Smith, D. R., "Adaptive compensation control of symthetic jet actuator arrays for airfoil virtual shaping," *Journal of Aircraft*, Vol. 44, No. 2, 2007, pp. 616-626.

[77]Venugopal, R., and Bernstein, D. S., "Adaptive disturbance rejection using ARMARKOV/Toeplitz models," *IEEE Transactions on Automatic Control*, Vol. 8, No. 2, 2000, pp. 257-269.

[78]Tian, Y., Song, Q., and Cattafesta, L., "Adaptive feedback control of flow sepration," *3rd AIAA Flow Control Conference*, San Francisco, CA, 5-8 June, 2006, AIAA 2006-3016.

[79]Santillo, M. A., Hoagg, J. B., Bernstein, D. S., and Powell, K., "Adaptive disturbance rejection for flow in a duct with time-varying upstream velocity," *Preceedings of the 2007 American Control Conference*, New York, NY, 11-13 July, 2007.

[80]Cortelezzi, L., Chen, Y.-C., and Chang, H.-L., "Nonlinear feedback control of the wake past a plate: from a low-order model to a higher-order model," *Physics of Fluids*, Vol. 9, No. 7, 1997, pp. 2009-2022.

[81]Ito, K., and Ravindran, S. S., "A reduced order method for control of fluid flows," *Proceedings of the 35th Conferences on Decision and Control*, Kobe, Japan, December, 1996.

[82]Tadmor, G., Noack, B. R., Morzynski, M., and Siegel, S., "Low-dimensional mokdels for feedback flow control. part II: control design and dynamic estimation," *2nd AIAA Flow Control Conference*, Portland, Oregon, 28 June - 1 July, 2004, AIAA 2004-2409.

[83]Ljung, L., and Soderstrom, T., *Theory and Practice of Recursive Identification*, Cambridge, The MIT Press, 1983.

[84]Rojas, C. R., Hjalmarsson, H., Gerencser, L., and Martensson, J., "Consistent estimation of real NMP zeros in stable LTI systems of arbitrary complexity," *15th IFAC Symposium on System Identification*, Saint-Malo, France, July 6-8, 2009.

[85]Baughn, J. W., Porter, C. O., Peterson, B. L., McLaughlin, T. E., Enloe, C. L., Font, G. I., and Baird, C., "Momentum Transfer for an Aerodynamic Plasma Actuator with an Imposed Boundary Layer," *44th AIAA Aerospace Sciences Meeting and Exhibit*, Reno, NV, Jan 9-12, 2006.

[86]Abdoli, A., Mirzaee, I., Anvari, A., and Purmahmod, N., "Simulation of body force field effects on airfoil separation control and optimization of plasma actuator," *J. Phys. D: Appl. Phys.*, Vol. 41, 2008.

[87]Madsen, J. I., Shyy, W., and Haftka, R. T., "Response surface techniques for diffuser shape optimization," *AIAA Journal*, Vol. 38, No. 9, 2000, pp. 1512-1518.

[88]Mckay, M. D., Beckman, R. J., and Conover, W. J., "A comparison of three methods for selecting values of input variables from a computer code," *Technometrics*, Vol. 21, 1979, pp. 239-245.

[89]Broomhead, D. S., and Lowe, D., "Multivariable functional interpolation and adaptive networks," *Complex Systems*, Vol. 2, 1988, pp. 321-355.

[90]MATLAB® contributors, *MATLAB The Language of Technical Computing, Version 7.0 Release 14*, Natick, MA, The MathWorks, Inc., 2004.

[91]Viana, F. A. C., and Goel, T., *SURROGATES Toolbox*, http://fchgury.110mb.com, 2007.

[92]Jayaraman, B., Tharkur, S., and Shyy, W., "Modeling of fluid dynamics and heat transfer induced by dielectric barrier plasma actuator," *J. Heat Trans.*, Vol. 129, 2007, pp. 517-525.

[93]Shyy, W., and Sun, C.-S., "Development of a pressure-correction/staggered-grid based multigrid solver for incompressible recirculating flows," *Computers and Fluids*, Vol. 22, No. 1, 1993, pp. 51-76.

[94]Shyy, W., *Computational Modeling for Fluid Flow and Interfacial Transport*, Amsterdam, Netherlands, Elsevier, 1994.

[95]Ward, A. L., "Calculations of cathode-fall characteristics," *J. Appl. Phys.*, Vol. 33, No. 9, 1962, pp. 2789-2974.

[96]Jayaraman, B., Cho, Y.-C., and Shyy, W., "Modeling of dielectric barrier discharge plasma actuator," *J. Appl. Phys.*, Vol. 103, 2008, p. 053304.

[97]Van Dyken, R., McLaughlin, T. E., and Enloe, C. L., "Parametric investigations of a single dielectric barrier plasma actuator," *42nd AIAA Aerospace Sciences Meeting and Exhibit*, Reno, NV, 5-8 January, 2004, AIAA 2004-846.

[98]Enloe, C. L., McLaughlin, T. E., Gregory, J. W., Medina, R. A., and Miller, W. S., "Surface potential and electric field structure in the aerodynamic plasma actuator," *46th AIAA Aerospace Sciences Meeting and Exhibit*, Reno, NV, 7-10 January, 2008, AIAA 2008-1103.

[99]Hippel, A. R. V., *Dielectric Materials and Applications*, The Technology Press of MIT and John Wiley & Sons, Inc, 1954.

[100]Morrow, R., and Sato, N., "The discharge current induced by the motion of charged particles in time-dependent electric fields; Sato's equation extended," *J. Phys. D: Appl. Phys.*, Vol. 32, 1999, pp. L20-L22.

[101]Singh, K. P., and Roy, S., "Modeling plasma actuators with air chemistry for effective flow control," *J. Appl. Phys.*, Vol. 101, 2007.

[102]Porter, C. O., Baughn, J. W., McLaughlin, T. E., Enloe, C. L., and Font, G. I., "Plasma actuator force measurements," *AIAA Journal*, Vol. 45, No. 7, 2007, pp. 1562-1570.

[103]Opaits, D. F., Edwards, M. R., Zaidi, S. H., Shneider, M. N., Miles, R. B., Likhanskii, A. V., and Macheret, S. O., "Surface plasma induced wall jets," *38th AIAA Aerospace Sciences Meeting including the New Horizons Forum and Aerospace Exposition*, Orlando, Florida, 4-7 January, 2010, AIAA 2010-469.

[104]Hoskinson, A. R., Hershkowitz, N., and Ashpis, D. E., "Force measurements of single and double barrier DBD plasma actuators in quiescent air," *J. Phys. D: Appl. Phys.*, Vol. 41, 2008, 245209.

[105]Jacob, J. D., Ramakumar, K., Anthony, R., and Rivir, R. B., "Control of laminar and turbulent shear flows using plasma actuators," *4th International Symposium on Turbulence and Shear Flow Phenomena*, Williamsburg, VA, 27-29 June, 2005.

[106]Hale, C., Erfani, R., and Kontis, K., "Multiple encapsulated electrode plasma actuators to influence the induced velocity: further configurations," *40th Fluid Dynamics Conference and Exhibit*, Chicago, Illinois, 28 June - 1 July, 2010, AIAA 2010-5106.

[107]Kamakoti, R., Thakur, S., Wright, J., and Shyy, W., "Validation of a new parallel all-speed CFD code in a rule-based framework for multidisciplinary applications," *36th AIAA Fluid Dynamics Conference and Exhibit*, San Francisco, CA, 5-8 June, 2006, AIAA 2006-3063.

[108]Grundmann, S., Klumpp, S., and Tropea, C. "Experimental and numerical investigations of boundary-layer influence using plasma-actuators," *Active Flow Control, NNFM 95*. Springer, New York, 2007, pp. 56-68.

[109]Rizzetta, D. P., and Visbal, M. R., "Numerical investigation of plasma-based flow control for transitional highly loaded low-pressure turbine," *AIAA Journal*, Vol. 45, No. 10, 2007, pp. 2554-2564.

[110]Jayaraman, B., Cho, Y.-C., and Shyy, W., "Modeling of dielectric barrier discharge plasma actuator," *J. Appl. Phys.*, Vol. 103, 053304, 2008.

[111]Pope, A., *Basic Wing and Airfoil Theory*, McGraw-Hill Book Company Inc., 1951.

[112]Gilbert, P. D., "A note on the computation of time series model roots," *Applied Economics Letters*, Vol. 7, 2000, pp. 423-424.

[113]Ho, B. L., and Kalman, R. E., "Effective construction of linear state-variable models from input/output data," *3rd Annual Allerton Conference on Circuit and System Theory*, Monticello, Illinois, 1965.

[114]Juang, J.-N., and Pappa, R. S., "An eigensystem realization algorithm for modal parameter identification and model reduction," *Journal of Guidance, Control, and Dynamics*, Vol. 8, No. 5, 1984, pp. 620-627.

[115]Jonckheere, E., and Ma, C., "Recursive partial realization from the combined sequence of Markov parameters and Moments," *Linear Algebra And Its Applications*, Vol. 124, 1989, pp. 565-590.

[116]Santillo, M. A., and Bernstein, D. S., "Adaptive control based on retrospective cost optimization," *Journal of Guidance, Control, and Dynamics*, Vol. 33, No. 2, 2010, pp. 289-304.

[117]Ljung, L., *System Identification: Theory for the User*, New Jersey, P T R Prentice Hall, Inc., 1987.

[118]Rosenbrock, H. H., *State-space and Multivariable Theory*, London, Nelson, 1970.

[119]Stewart, J., and Davison, D. E., "On overshoot and nonminimum phase zeros," *IEEE Transactions on Automatic Control*, Vol. 51, No. 8, 2006, pp. 1378-1382.

[120]Lau, K., Middleton, R. H., and Braslavsky, J. H., "Undershoot and settling time tradeoffs for nonminimum phase systems," *IEEE Transactions on Automatic Control*, Vol. 48, No. 8, 2003, pp. 1389-1393.

[121]Ioannou, P. A., and Sun, J., *Robust Adaptive Control*, Prentice-Hall Inc., 1996.

[122]Tao, G., *Adaptive Control Design and Analysis*, Hoboken, New Jersey, John Wiley & Sons, Inc., 2003.

[123]Anderson, B. D. O., "Topical problems of adaptive control," *Proceedings of the European Control Conference*, Kos, Greece, 2-5 July, 2007.

[124]Ragazzini, J. R., and Franklin, G. F., *Sampled-data Control Systems*, New York, McGraw-Hill, Inc., 1958.